THE MILLING OF TIN BRONZE WITH A Cu-24.6wt%Sn COMPOSITION

by Garth Williams

A dissertation submitted to the Faculty of Engineering, University of Cape Town
in part fulfilment of the requirements for the degree of
Masters of Science in Materials Engineering

Department of Materials Engineering
University of Cape Town
February 1997

Abstract

The effects of high energy milling on tin bronze with the composition Cu-24.6wt%Sn have been examined using hardness testing, optical microscopy, scanning electron microscopy, transmission electron microscopy and x-ray diffraction. High energy milling has caused mechanical alloying of an elemental copper and tin powder blend, and mechanical milling of a cast powder and a melt quenched powder.

Nanocrystalline grains with a size between 5 nm and 50 nm have been directly observed in the final milled powder. The powder consist of the α phase and δ phase and is partially amorphous. An extension of the solid solution solubility has also been detected due to milling. The formation of the metastable tin-rich η phase has been observed in the intermediate stage of mechanical alloying of the elemental powder blend due to the higher diffusivity of tin in copper over copper in tin. The formation of the η phase during mechanical alloying of tin bronze with the composition Cu-24.6wt%Sn has not been reported before.

The morphological development of the three initial powders has proceeded by different mechanisms during milling due to the different hardness and toughness of the starting powders. Milling of the elemental powder blend and the cast powder proceeds via classic mechanisms for milling of ductile powders and brittle powders respectively, while milling of the tougher melt quenched powder proceeds via a combination of the two mechanisms.

An attempt to process the milled powder into a bulk state using various thermo-mechanical techniques while still retaining a nanocrystalline grain size has not succeeded. The high diffusivity of the material at elevated temperatures has led to grain growth into the micrometer range even at relatively low thermo-mechanical processing temperatures. The milled powders have poor compaction properties due to the highly deformed structure and therefore the processed material has poor properties compared to a cast material.

Acknowledgements

I would like to thank the following people who have assisted and/or advised me during the course of my studies (all affiliated to the Department of Materials Engineering at the University of Cape Town unless otherwise stated):

Jacky Sharland (formerly employed at the Department of Materials Engineering of UCT) and Anne Ball for helping to cut through the all the administrative red tape. Reggie Hendricks, Nick Dreze and Glen Newins for their assistance in the workshop.

Alan Duckham for hot pressing my powder samples. Bernard Greeves and James Peterson for printing of micrographs.

Terry Heaney of the Geology Department of UCT for assistance with the x-ray diffractometer. Mohammed Jaffer and William Williams of the Electron Microscope Unit of UCT for helping with transmission electron microscopy.

Mike Cortie of the Department of Physical Metallurgy, Mintek for suggesting and assisting me with the project.

David Knight and Fiona Levy of the Department of Physical Metallurgy, Mintek and Sharhad Nana, formerly employed at the Department of Physical Metallurgy, Mintek, for their assistance during my visits there.

Jimmy MacDonald of the Ultra High Pressure Unit (formerly Debex) for hot isostatic pressing of my powder samples.

And lastly my supervisor Candy Lang for her guidance with my project and her patience.

The financial support of Mintek is gratefully acknowledged.

This thesis is dedicated to my parents, Robert and Naira Williams for the opportunities, support and love they have given me through the years.

TABLE OF CONTENTS

1. INTRODUCTION

The aim of this project was to investigate the effects of high energy milling on tin bronze with the composition Cu-24.6wt%Sn. High energy milling is a non-equilibrium powder metallurgy technique which has been used to produce powders with metastable crystalline phase, powders with an extended solid solubility and metallic glass powders [1, 2]. High energy milling can also lead to the refinement of the crystal size into the nanometer range [1, 2]. The resulting material is called a nanocrystalline material. The Cu-Sn system was selected as it has been well characterised and because the component elemental materials are cheap and abundant.

Nanocrystalline materials have displayed improved properties over conventional materials with a microcrystalline structure as a result of their fine grain size. Ductility and toughness enhancement of brittle materials, improved sinterability, and increased strength and hardness have been reported as a result of the refinement of the grain size of various materials into the nanometer range [3].

It is possible to make use of the properties of nanostructured materials to enhance the fabricability of complex materials and components, even if the nanostructure is not retained in the final product [3]. Intermetallics are notorious for their limited ductility and formability at low temperatures. A fine grain size is thought to be beneficial in this regard. By reducing the grain size into the nanoscale region, superplastic deformation processes can be accomplished at temperatures lower than those conventionally employed in manufacturing components with an intermetallic structure. After the article has been processed into the desired shape, heat treatment at elevated temperatures will produce grain growth, resulting in a material with a good creep resistance for high temperature applications.

Lightweight nanocrystalline materials find application in the aerospace and automotive industries due to their enhanced strength compared with conventionally processed microcrystalline materials, as these industries continually strive to increase the efficiency of their driving engines by improving the strength to weight ratio of the

individual components [4]. Recently, high energy milling in the Cu-Sn system has been performed in order to improve the room temperature reaction rate of the resulting powder with the liquid Ga-In-Sn eutectic [5]. Improving the reaction rate of the milled material with the liquid alloy at room temperature may lead to usage as a low temperature solder or as dental filling materials.

In the present study, high energy milling of Cu-Sn powders in three different initial states was performed, and it was found that the morphological development during milling of the powder was different for each initial state. Milling of this material has led to the development of a metastable crystalline phase in the intermediate stage of milling, and has produced a powder with an extended solid solubility. Nanocrystallinity was observed during transmission electron microscopy examination of the powders. The milled powders which were processed using various thermo-mechanical techniques exhibited poor properties compared with the bulk microcrystalline material. As the nanocrystalline structure and corresponding enhanced properties produced by high energy milling are lost at high temperatures, this powder material is not suitable for conventional thermo-mechanical processing.

2. LITERATURE REVIEW

2.1 Introduction

Conventional coarse grained polycrystalline materials have a grain size in the micrometer range. Nanocrystalline (NC) or nanophase materials, as their name implies, have grain sizes typically in the range of 1 nm to 100 nm in at least one dimension [4, 6, 7]. Materials with ultrafine microstructures contain such a high density of defects (grain boundaries, interphase boundaries, dislocations, etc.) that the distances between these defects approach interatomic distances [7]. Figure 2.1 shows a schematic diagram of a pure metal with a NC grain size.

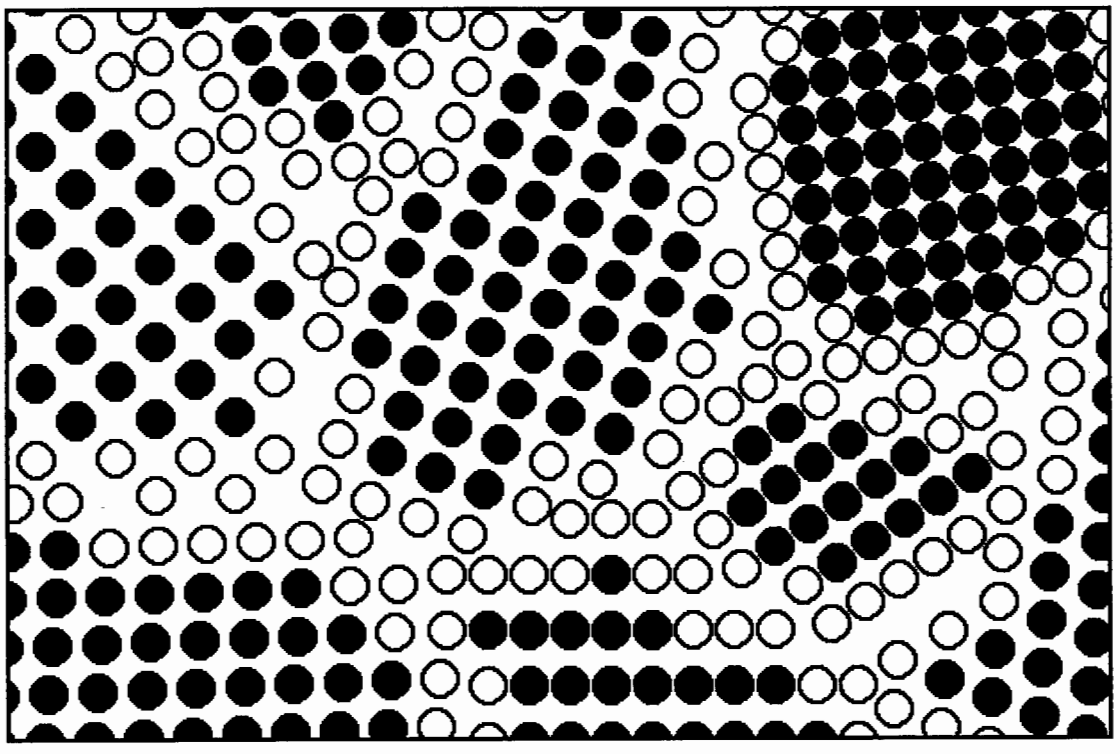

Figure 2.1: Schematic representation of an equiaxed NC metal showing atoms associated with the crystalline grains (filled circles) and those constituting the boundary network (open circles). (Redrawn from [6].)

It is immediately apparent that a characteristic attribute of these materials is the high density of interfaces as well as the reduced density in these regions [6, 7]. The number of atoms at the interfaces, or grain boundaries, is comparable to the number of

atoms within the grains [8]. It can be said that the material has a high ratio of interface atoms to crystallite atoms or R_{ic}.

Assuming the grains to have the shape of spheres or cubes, R_{ic} can range from 0.27 to 0.49 for nanophase materials with an average grain size of 5 nm, assuming a simple grain boundary arrangement and a grain boundary thickness of approximately 0.5 nm to 1.0 nm [8]. R_{ic} falls to between 0.14 to 0.27 for a 10 nm grain size, and to as low as 0.01 to 0.03 for a 100 nm grain size. Materials with a conventional grain size (> 1 μm) have a negligible R_{ic} [8]. This variation is shown graphically in Figure 2.2.

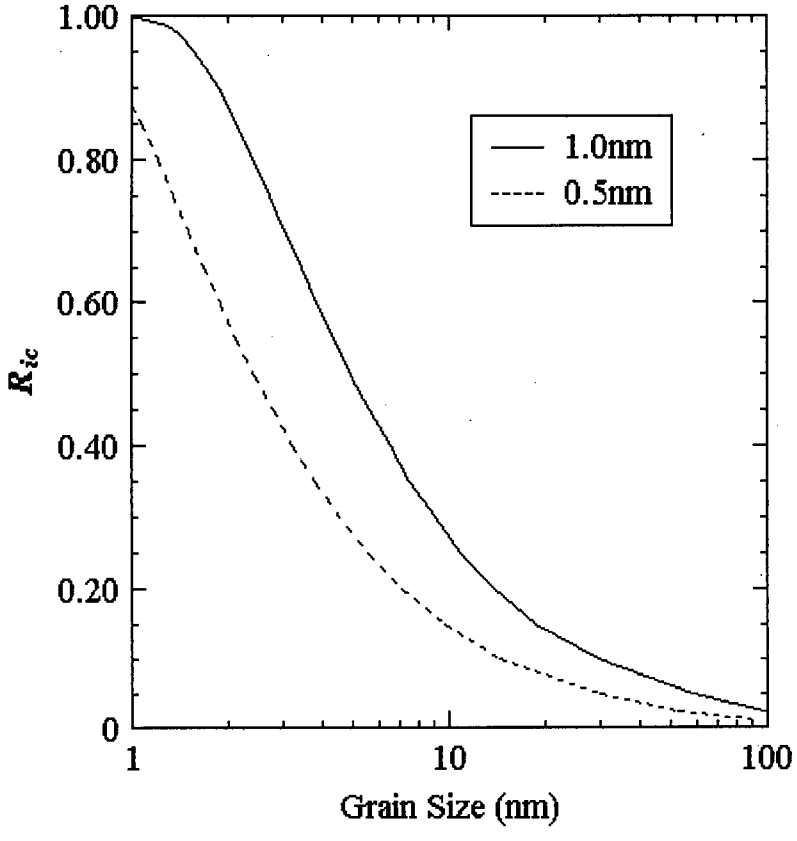

Figure 2.2: Range of fraction of atoms in grain boundaries or R_{ic} of a NC material as a function of grain size, assuming an average grain boundary thickness of 1.0 nm and 0.5 nm. (Redrawn from [8].)

Grain boundaries are characterised by a reduced atomic density, typically 10 % to 30 % of the density of crystalline regions, and a broad spectrum of interatomic spacings ranging from closely packed to widely spaced atoms in comparison to the

perfect lattice [6, 7, 9]. The effects of this modified structure are negligible in coarse grained polycrystals because the volume fraction of the boundary cores is negligible.

If the volume fraction of the grain boundary core is increased to appreciable levels by decreasing the grain size to the nanometer range, the effects of the modified structure of the grain boundaries are no longer negligible. The properties of NC materials can therefore expected to be strongly influenced by the nature of their internal boundaries simply because of the high number of these boundaries and the significant fraction of atoms associated with them [8].

It has been said that the structure in the boundary exhibits neither long nor short range order, a structure which is in contrast to that obtained in both crystalline and amorphous alloys [6, 7, 9]. The grain boundaries in NC metals are in a relatively unrelaxed state in that the system has a local but not a global energy minimum, i.e. the material is in a metastable condition [6]. This structure together with a high R_{ic} number is expected to produce many novel, and often improved, properties relative to those of conventional polycrystalline materials. Among these are a decreased density; a supermodulus effect; increased reactivity, strength, hardness, thermal expansion, specific heat, diffusion rate and ductility (even in ceramics and intermetallic compounds) [2, 3, 6, 7]. A summary of selected property changes which occur in a NC material is shown in Figure 2.3.

Because materials with an ultrafine microstructure have a high diffusion rate, a resulting problem is their thermal stability. The large amounts of energy stored in these materials provide driving forces for recovery and recrystallisation processes. Metals with a grain size of approximately 10 nm and an equilibrium melting temperature below 600 °C (e.g. tin, lead, aluminuim) have shown significant grain growth (doubling of the crystal size in 24 hours) at room temperature or below [10].

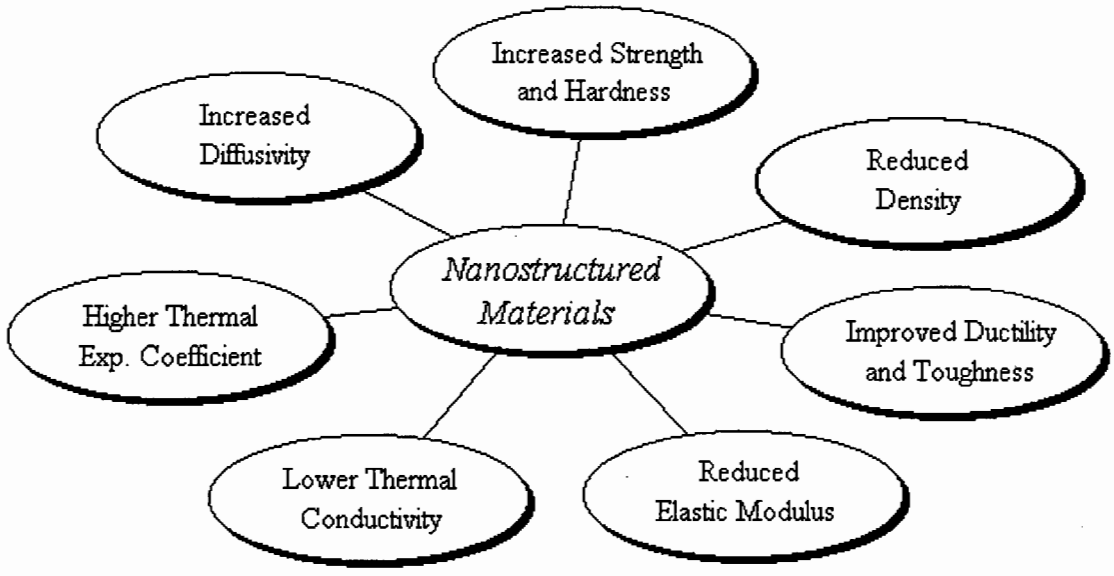

Figure 2.3: Summary of selected property changes associated with nanostructured materials. (Redrawn from [3].)

Intermetallic compounds have a highly ordered structure. The structure of the material can be thought of as two (or more) interpenetrating sub-lattices, with each sub-lattice containing a different arrangement of atoms. The resulting structure is referred to as a superlattice. The necessary condition for the formation of a superlattice, i.e. an ordered solid solution, is that dissimilar atoms must attract each other more than similar atoms. In addition, the alloy must exist at or near a composition which can be expressed as a simple formula, e.g. A_3B [11]. The high degree of ordering in intermetallics imparts to the material a high tensile strength, but causes the material to be brittle and/or have a low toughness due to the difficulty of dislocation motion through the lattice, especially at room temperature where failure occurs by intergranular fracture [12, 13, 14, 15]. This property has limited the widespread usage of intermetallic compounds in industry, especially as these materials possess many enhanced properties (high specific strength, high specific stiffness, retention of strength at high temperatures) which make them attractive to the aerospace industry [7, 15].

Refinement of the microstructural scale leads to improvements in the resistance to brittle failure. This may be understood on the basis of the work of Petch which considers the stress required to nucleate and grow microcracks and the stresses for

plastic flow [2]. Ductile flow should be allowed before a flaw propagates as a brittle crack. If the microstructure is refined so that the grain size is smaller than the critical flaw size, yield of an intermetallic material is possible, and failure will take place in a ductile manner [16]. It has been suggested that below a critical grain size, significant room temperature ductility might be possible in intermetallic materials [17, 18] and that through nanophase processing, the ductility of these materials may be improved [1, 7, 18].

For example, mechanically alloyed Fe-Al intermetallics have been shown to be ductile at room temperature [13, 19]. The NiAl system has been made ductile at 400 °C by refining the grain size to below 20 μm [17]. The critical grain size for harder and more brittle intermetallics is much smaller than this, and therefore in order to make the material ductile, the grain size needs to be reduced to far smaller values.

Nanostructured crystallites have been prepared by mechanical milling, rapid solidification from the liquid state, molecular beam epitaxy, reactive sputtering, sol-gel techniques, mechanical alloying, electrodeposition, chemical vapour deposition processes and modified gas condensation methods, of which the latter four techniques are the most widespread [6, 9]. The resulting microstructure can be tailored by varying the process variables in each of these methods. Controlled crystallisation of an amorphous phase produced by any of the methods listed above can also produce NC materials [6, 20].

2.2 The Cu-Sn System

The phases found in the Cu-Sn system are described in this section. Particular emphasis is placed on the phases surrounding the composition of Cu-24.6wt%Sn. Reference is made to Figure 2.4 which shows the binary equilibrium phase diagram for the copper-tin system.

The α phase is face-centred cubic (fcc) of the A1 type, and the β phase is a disordered body-centred cubic (bcc) electron compound (A2 type) with an electron to atom ratio

of 3:2 [21, 22, 23, 24, 25]. At the eutectoid composition, the β phase has the composition Cu_5Sn [21]. The γ phase is complex cubic with a DO_3 type superlattice, and is analogous to Fe_3Al [21, 22, 23, 26].

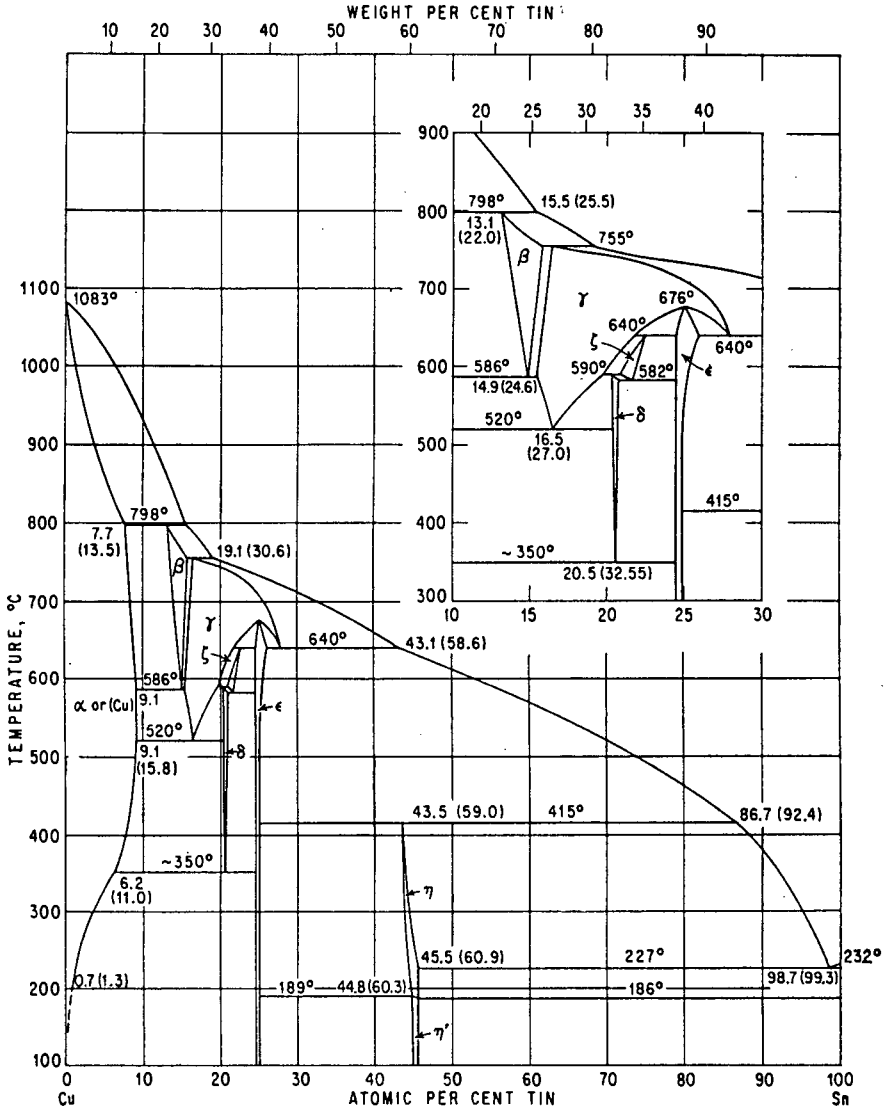

Figure 2.4: Binary Cu-Sn equilibrium phase diagram after Hansen [26].

The crystal structure of the δ phase intermetallic compound is complex cubic, and is analogous to that of the γ brass structure ($D8_2$ type superlattice) [22, 23, 24, 26]. The δ phase is an electron compound with an electron to atom ratio of 21:13, and has a slightly variable composition depending on the solute content of the material [26]. The stoichiometric formula varies from Cu_4Sn to $Cu_{31}Sn_8$ and $Cu_{41}Sn_{11}$ for the compositions of Cu-31.83wt%Sn, Cu-32.53wt%Sn and Cu-33.39wt%Sn respectively [26].

The ε phase intermetallic compound is orthorhombic and has a stoichiometric formula of Cu_3Sn, and the η phase is hexagonal (NiAs type) and nearly corresponds to the formula Cu_6Sn_5 [24, 26].

The δ phase decomposes into the α phase plus ε phase eutectoid at approximately 350 °C. This transformation occurs extremely slowly and it is difficult to obtain equilibrium in the α phase plus ε phase region as supersaturated α phase and supercooled δ phase usually persist [24, 26]. The δ phase can be considered stable below 350 °C [26].

Martensite can be produced by quenching the material from the β phase field. Martensite denoted β′ or β'_1 can be produced by quenching β phase containing between 22.0wt%Sn and 24.1wt%Sn to ambient temperatures [27, 28]. β′ may also be formed by the application of stress, either during metallographic specimen preparation or during the actual quenching process [29]. A martensite denoted γ'_1 or β″ is formed when β phase containing between 24.1wt%Sn and 25.6wt%Sn is quenched to cryogenic temperatures [27, 30].

Between 586 °C and 520 °C the β phase transforms to non-lamellar α phase plus γ phase via a eutectic decomposition by means of grain boundary and intergranular nucleation [26, 31]. The α phase takes the form of needles.

The β phase initially decomposes to the α phase plus γ phase instead of the α phase plus δ phase between 520 °C and 480 °C as the former transformation has a shorter incubation period than the latter [31]. This γ phase survives for approximately 10 seconds and then decomposes to the α phase plus δ phase [31].

During the interval 480 °C to 350 °C the β phase decomposes to a α phase plus δ phase bainite [31]. Below 350 °C the β phase decomposes to the α phase plus ε phase, although the transformation is extremely slow and only occurs with protracted annealing.

2.3 Milling

The objectives of conventional milling are particle size reduction, mixing or blending and particle shape changes [32]. However, milling at an intensity which results in a high energy transfer rate between the milling media and powder particles, or high energy milling (HEM), can lead to solid state alloying and high degrees of metastability and microstructural refinement [1, 2]. HEM can produce materials with a NC structure by the structural decomposition of coarse grained structures as a result of severe mechanical deformation [1, 2, 33].

HEM of powders with different compositions, in which material transfer occurs, is called mechanical alloying or MA, and milling of single component powders (such as compounds and elements) has been termed mechanical milling or MM [1, 34]. HEM can result in NC structures by both MM of single component systems and MA of multi-component powders.

The powders produced by HEM can have an amorphous or NC structure after milling, depending on the differences in free energy between the crystalline alloy and that of the amorphous phase [35], and the energy transfer rate between milling media and powder particles which the milling equipment is capable of [6]. The final structure after milling intermetallic compounds with a high stability and a large difference in free energy compared to the amorphous phase is most likely to be NC in nature [35].

If the equipment used is capable of imparting large amounts of energy into the system at a sufficiently high rate so that the material cannot dissipate the energy fast enough, and the free energy reaches a level where amorphisation can take place, the resulting structure will be amorphous. Thus, nanometer-sized grains can be produced by the low temperature crystallisation of an amorphous phase, or by HEM to a condition just before the alloy transforms into an amorphous phase [12, 20].

When the initial material is a single elemental powder or a mix of elemental powders which are structurally and chemically similar, the product after milling is usually a

NC powder [36]. Thermo-mechanical processing of these powders results in a material with a nanoscale grain size separated by relatively thick grain boundaries with a high dislocation density. The volume fraction of these domain walls can easily equal that of the crystalline domains as shown in Figure 2.2 on page 4.

The grain size of the material decreases logarithmically with milling time [1]. Several variables can influence the minimum grain size achievable and the rate at which the grain size reduces, namely the energy transfer rate during milling, the ball to powder weight ratio, processing time and temperature, type of milling control agent (used to prevent excessive agglomeration of the powder during milling), the work hardening rate of the constituents, the powder composition, and to some extent, the melting point of the material [1, 34, 37]. Another parameter which can in practice strongly influence the final powder is the contamination of the powder during processing, from erosion of the milling media and container, foreign gas leaking into the milling chamber, or even from the milling control agent.

The type of milling apparatus used limits the amount of energy which can be imparted to the powder. The energy transfer rate of the milling medium to the powder particles depends on the power supplied to drive the milling chamber as well as the internal mechanics of the specific mill. HEM is normally performed in equipment capable of high energy compressive impact forces such as attrition mills, vibrating ball mills and shaker mills [1, 38]. Conventional ball mills may be employed if sufficiently large diameter balls are used and the mill is operated just below the critical speed at which the centrifugal force pins the balls and the media to the mill chamber wall.

Figure 2.5 is a schematic diagram showing an attrition mill, in which the milling medium and powder charge are stirred by a central shaft and arms; a shaker mill, in which the milling medium and powder charge are shaken back and forth at high speeds in one plane inside a small capsule; and a conventional ball mill in which the milling medium and powder charge are contained inside a rotating cylinder.

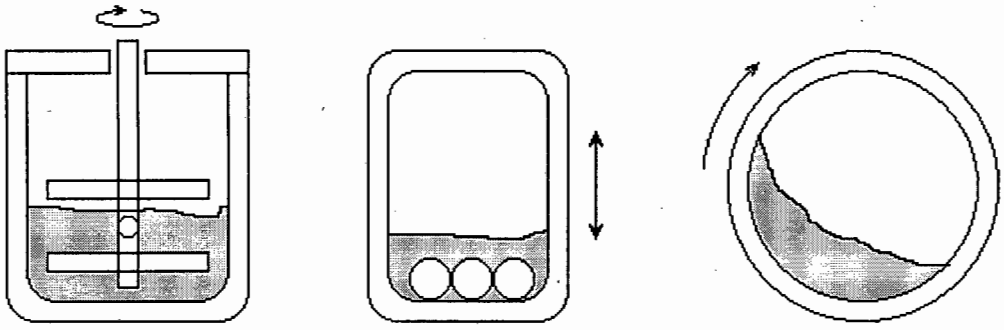

Figure 2.5: Diagrams of an attrition mill, a shaker mill and a conventional ball mill showing the direction of motion during milling (not to scale).

The mills are classed according to the milling time to produce a given microstructure, according to the variation in the energy transfer rate between the milling media and the powder particles [1]. It is possible to induce amorphisation after the formation of a NC structure in a shaker mill, but not in a less energetic conventional ball mill, where the grain size saturates to a larger constant value. It takes far more time (orders of magnitude) to attain a NC structure using a conventional ball mill compared with a shaker mill. A more energetic mill is thought to provide more lattice strain, which is related to the development of the finer grain size and amorphisation.

The ball to powder weight ratio has a similar effect: The higher the ratio, the lower the minimum achievable grain size will be [1]. The milling temperature influences the rate at which the NC structure develops: The higher the milling temperature the slower the rate. For fcc metals, the minimum attainable grain size scales inversely with the melting temperature of the material [39]. This trend does not extend to other classes of materials, such as intermetallic compounds and metals with an hcp or bcc structure as can be seen from Figure 2.6.

The effects of the energy transfer rate during milling, the milling temperature and the melting temperature of the material suggests a competition between defect creation by the cyclic plastic deformation and defect recovery by thermal activation [1, 37]. Lowering the temperature during milling accelerates the microstructural development of the powder compared with milling at room temperature, and also determines the minimum attainable grain size, i.e. milling at lower temperatures will favour fine NC

grain formation. Temperature rises between 100 °C and 350 °C have been estimated by modelling of the milling process, depending on the type of mill used [38].

Dislocation pileup models can be used to explain the development of nanoscale grain sizes by mechanical attrition. These models are typically employed to explain the strengthening of materials due to grain size refinement, e.g. Hall-Petch behaviour.

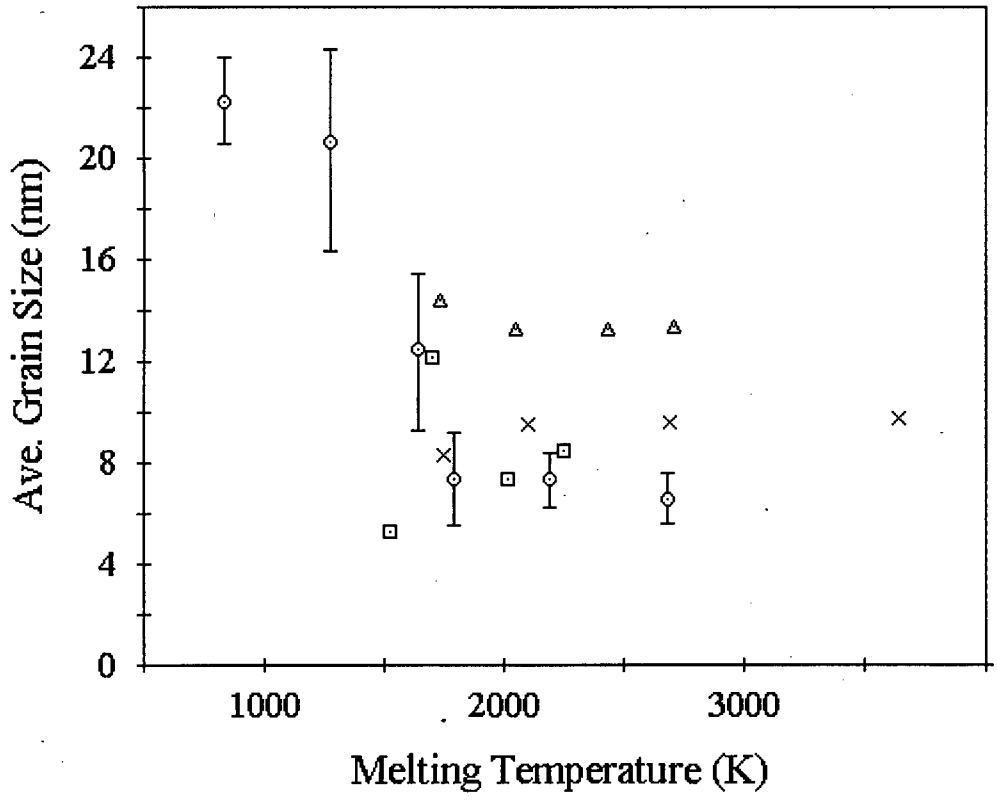

Figure 2.6: Minimum grain size for several fcc (o), bcc (×) and hcp (Δ) metals, and intermetallic compounds (□) versus the melting temperature of the materials. (Redrawn from [1].)

One method of achieving a high energy transfer rate between milling media and powder particles is in an attrition mill. Milling is achieved in a stationary tank by means of a rotating shaft and arms which agitate the media into a random state of internal porosity called kinematic porosity [40]. In this expanded condition, the media and particles are free to move, and collide and impinge upon one another. This process is illustrated in Figure 2.7.

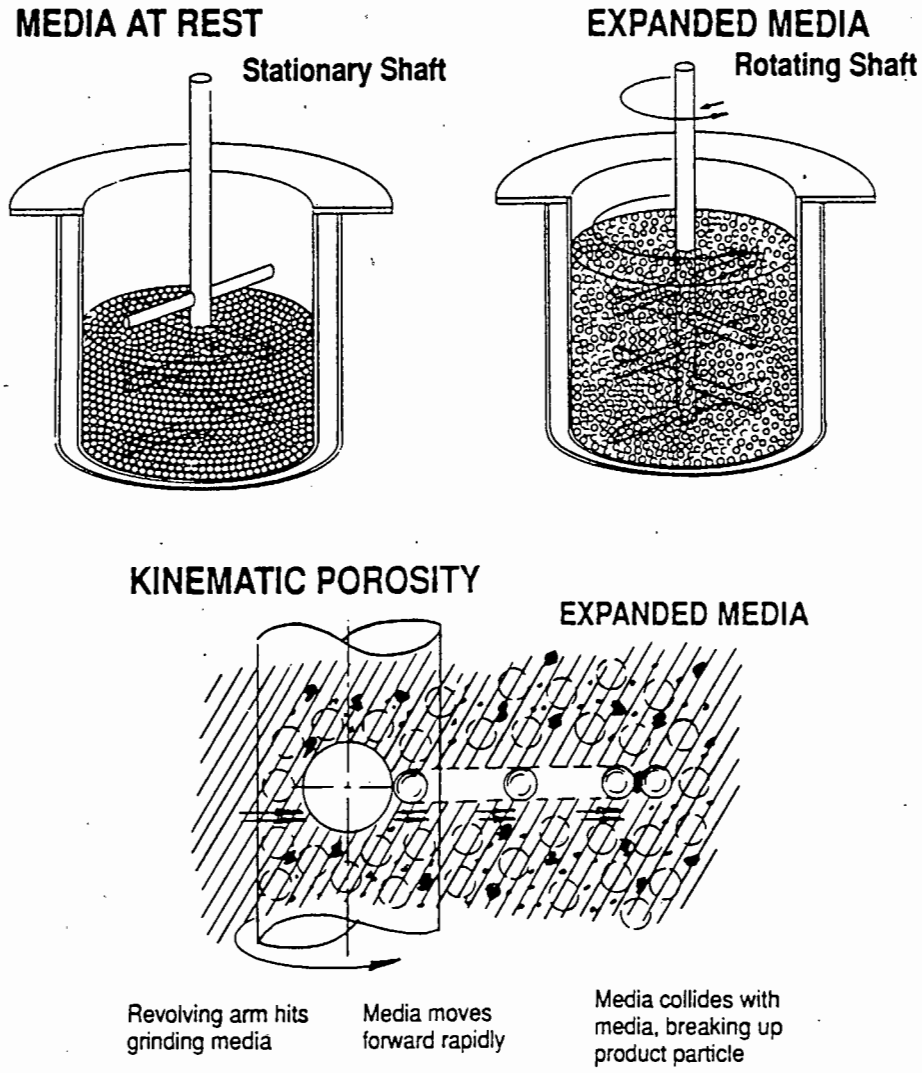

Figure 2.7: Schematic diagram showing the inside of an attrition mill with the media at rest and in an expanded condition, and a close-up of an attritor arm impinging upon the grinding media. (Reproduced from Union Processes, Inc. sales brochure [40].)

Advantages of HEM (for MA and MM) over other processes used to produce a material with a NC grain size are the following:

- It is possible to produce large volumes of material (half a kilogram using a *Szegvari*[◆] attritor mill, and up to two tonnes using large conventional ball mills [9, 41]), whereas it is only possible to produce small quantities in the region of grams using other techniques, for example gas condensation [4, 6]. This therefore makes MA attractive commercially.

◆ Registered Trademark of Union Processes, Inc., Akron, OH.

- Since MA is entirely a solid state process, the problems normally associated with melting and solidification (such as segregation and large differences in melting temperatures) are bypassed [13].

- Because of the high diffusion rate and the small size of the particles (and therefore the small pore size), the sinterability is increased, even at low temperatures [12].

- MA can be used to alloy elements which are normally difficult or impossible to combine by conventional melting techniques, i.e. alloys whose constituents are immiscible in the solid or liquid phase, or whose melting points are significantly different [32, 38, 41].

- It is possible to produce new phases with novel microstructures and properties which are not thermodynamically favoured [41].

The main disadvantages of the HEM process are the following:

- Control of the impurity content of the final powder is difficult to achieve as the powders become contaminated due to gases being present in the chamber during milling, or by erosion debris from the container and balls themselves. [1, 2, 6, 34, 37, 42].

- Most milled powders cannot be cold consolidated because of the particles' highly deformed state, and have to undergo thermo-mechanical processing in order to produce the desired microstructure [2, 41].

- It is difficult to produce fully dense bulk samples while still retaining a NC structure using conventional thermo-mechanical processing [43, 44]. The high energy stored in these structures provide driving forces for recovery and recrystallisation, and therefore the elevated temperatures employed during thermo-mechanical processing lead to significant grain growth [1, 7,45].

- There is the potential for excessive oxidation or elemental loss if the milling environment is not controlled or if the milling equipment is faulty [35, 37, 46]. The entrapped oxygen can have a detrimental effect on the properties of the compact. Even if oxidation is minimised, pre-existing oxide films can be folded into the alloyed structure during milling [13].

- The process of milling is very inefficient [2]. Tremendous energy losses occur during milling in the form of noise and heat.

2.3.1 Mechanical Alloying

Mechanical alloying (MA) involves the blending together of a mixture of powders (elemental or pre-alloyed) in a mill. MA differs from conventional blending in that the kinetic energy of the colliding balls inside the mill is orders of magnitudes higher. In conventional milling the energy transfer rate between the milling media and the powder particles is small. The powder particles trapped between the colliding balls may fracture, but the pressure during collision is insufficient to cause large amounts of plastic deformation in the powder particles. During MA, however, the powder particles are not only fractured, but are also heavily deformed and cold welded [1, 34, 38].

During MA, the repeated cold welding, fracturing and rewelding of a mixture of elemental powder particles in a high energy ball charge occurs to produce an alloyed powder with a controlled, extremely fine microstructure [4, 6, 34, 47]. Mixtures of elemental powders are subject to grinding under a protective atmosphere in equipment capable of high energy compressive impact forces such as attrition (or stirrer) mills, vibratory ball mills and shaker mills (shown in Figure 2.5 on page 12) [6, 47].

Interdispersion of the ingredients occurs by the process of repeated cold welding and fracturing of the powder particles which effectively kneads the internal structure of the powder particles so that the particles are continually refined and homogenised [38, 47]. The crystalline grain size of the material can be reduced to nano-scale dimensions through MA [5]. This process has been shown to produce materials with

nano-sized grains from elemental powders, intermetallic compound powders or immiscible powders.

The technique of MA was developed in the 1970's by the International Nickel Company (INCO) to combine in a nickel based superalloy the high temperature strength of a fine oxide dispersion with the intermediate temperature strength of a γ' phase precipitate, while including the required corrosion and oxidation resistance [48]. Recently it has been used to explore solid solubility extension, novel phase production and microstructural refinement [4, 5].

In conventional low-energy ball milling, particle welding is inhibited by the use of liquids and surface-active agents or surfactants such as heptane, hexane, octane, toluene or alcohol [2, 13, 42, 49, 50]. The correct surfactant needs to be selected for MA as it is critical to obtain the correct balance between fracture and welding necessary [38]. This depends on the alloy system as well as the processing conditions as welding in some systems does not have to be inhibited by a surfactant. For example, MA of equal parts of iron and chromium can be performed without any process modifications.

The deformation mode of the powder particles may also be altered so that the particles fracture before they are able to deform to the large compressive strains necessary for flattening and cold welding [38]. This can be accomplished by cryogenic milling. For example, lead is difficult to MA as it is extremely ductile at room temperature, but cooling to cryogenic temperatures promotes fracturing of the lead particles.

a) Macrostructural Changes During Mechanical Alloying

The MA process can be divided up into five stages in terms of morphological development (Figure 2.8) and powder size distribution (Figure 2.9) of the milled powder during MA of a ductile/ductile metal powder blend: 1) At the beginning of the initial stage, plate-like particles are formed by flattening of equiaxed starting particles under successive compressive ball/ball, ball/stirrer arm and ball/container

wall impacts [44, 47]. Towards the end of this stage the flattened elemental particles become welded and there emerges an increasing amount of composite particles with the different constituents arranged in parallel layers [41, 47]. When metal particles overlap during flattening, atomically clean metal interfaces are brought into intimate contact forming cold welds and building up layered composite powder particles consisting of various combinations of the starting ingredients [38]. The powder particles are still soft and ductile at this stage.

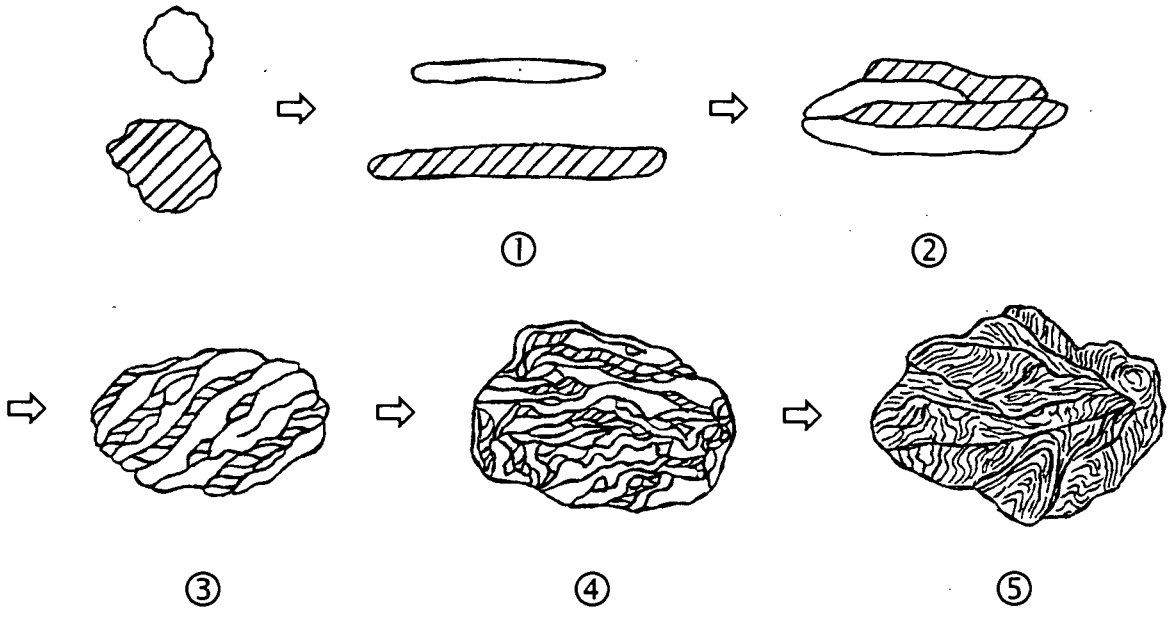

Figure 2.8: Diagram showing the five stages of the morphological development of an elemental powder mixture during MA. (Redrawn from [38].)

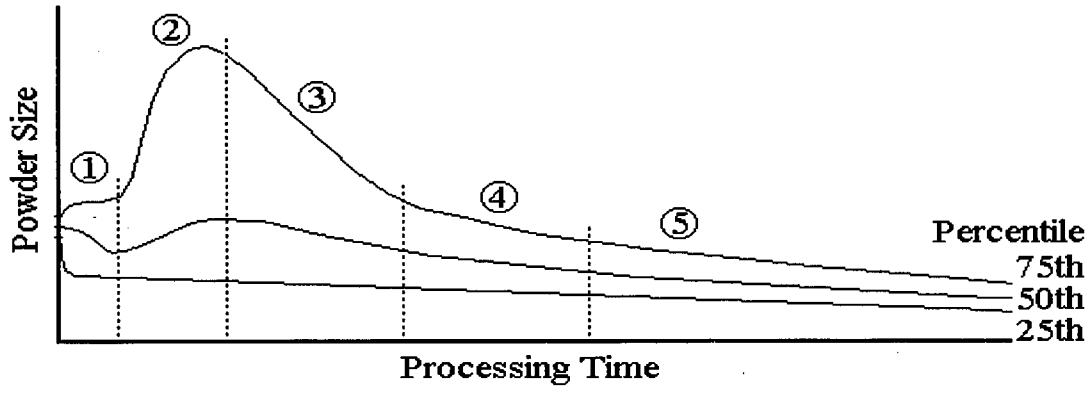

Figure 2.9: Powder size distribution during MA of an elemental powder mixture as a function of milling time showing the five stages of the morphological development. (Redrawn from [47].)

2) The next stage shows a predominance of welding together of individual elemental platelets [47]. During this stage, there is an increase in the amount of powder particles which display a multilayered composite structure with lamellae running parallel to the long axis of the flake-like particles [35]. The individual volume of these particles is approximately the same as the individual volume of the starting particles, indicating that the individual elemental lamellae within these particles are comminuted fragments of the elemental starting powders. This shows that the particles are starting to fracture as a result of loss of ductility due to work hardening, and are then welding together [38, 47]. The hardness of the particles shows a substantial increase over that of the starting particles, since virtually all the material has been severely deformed.

3) In the next stage there is a decrease in the amount of very coarse plate-like particles, and a trend towards particles consisting of parallel lamellae with more equiaxed dimensions [47]. This is a result of a significant decrease in ductility of the composite powder particles.

4) A stage of random orientation then emerges in which the elemental lamellae of the powder particles become convoluted [38, 41, 47]. This convoluted structure is a result of the welding together of equiaxed powder particulates without preference to orientation. There is a substantial increase in hardness of the material as well as a decrease in the proportion of coarser particles as the ductility of the powders continues to decrease, causing the particles to fracture into smaller particles [44, 47].

5) Finally, a steady state is reached which is characterised by an increasing internal homogeneity of the powder [41, 47]. The individual lamellae become too small to be optically resolved due to a repetitive cold welding and fracturing of the particles, and the composition of the individual particles tends towards the blend composition. The powder particle size reaches a steady state distribution which is dependent upon the composition of the system and of the processing parameters. At this stage, the hardness values of the powder particles attains a saturation value [38].

b) Microstructural Changes During Mechanical Alloying

Dissolution of the elemental constituents starts to occur during the formation of the particles with a multilayered composite structure of elemental lamellae during the third stage of MA. A solid state reaction (SSR) is induced between the elemental layers. Dissolution of the solute elements and the formation of areas of solid solution throughout the powder particle matrix during milling are facilitated by heating, lattice defects and short diffusion distances [38]. Heating occurs as the kinetic energy of the balls is absorbed by the powder during processing. The severe cold work resulting from MA reduces the diffusion distance to the micrometer range by providing many sites for low activation energy pipe diffusion [38].

SSR can lead to crystalline or amorphous phases, depending on the physical and chemical characteristics of the starting elements and on the milling conditions [39, 41]. During the early stages of alloying, alloy phase NC grains form at the interface between the elemental lamellae due to diffusion of the constituent elements. It has been suggested that these NC alloy phase grains originate owing to the multiple nucleation events and slow grain growth which occurs during milling, as each ball-powder-ball collision causes the local temperature to rise by only 100 °C to 350 °C above ambient [32].

What has been occurring throughout milling, and which becomes the dominant mechanism even after a steady state particle size distribution has been achieved, is extensive plastic straining of the material [51]. This straining of the material leads to a highly deformed powder. When the dislocation density reaches a critical value the structure relaxes into grains with a size in the nano-dimensional range, causing a reduction in strain. The grain size of the resulting material also depends on the energy transfer rate during milling [6]. It has been postulated that the rate at which MA occurs is strain rate dependent [52]. The rate of MA is ultimately controlled by the rate at which strain is accumulated in the powders as this determines the number of short circuit diffusion paths.

The formation of an extended solid solution can be induced by MA. The miscibility of a solute A in a solvent B is controlled by the chemical potential μ_A of A in the given solvent. If the atomic structure of B is changed, by HEM for example, the chemical potential and thus the solubility of A in B may be enhanced or reduced. Consequentially, the solute solubility of NC materials is expected to be different from that in conventional microcrystalline materials with the same composition [10]. For example, a supersaturated solid solution has been produced during MA of elemental molybdenum and silicon powders [53] and during MA of cobalt and tantalum powders [54].

2.3.2 Mechanical Milling

MM of a single component powder such as an intermetallic compound or an element can produce structural changes similar to those encountered during MA. The change of structure is thought to be induced as a result of the accumulation of defects brought about by the severe deformation which takes place during milling [1]. MM has been found to produce amorphous and NC structures via milling of intermetallics [1, 55, 56]. This is believed to occur when the stored energy of the defects accumulated during the milling process exceeds the difference in the free energy between the crystalline and amorphous states. Amorphisation through MM involves the energisation of the crystalline solid by the severe cyclic plastic deformation that HEM induces. MM has been found to induce plastic deformation in even highly brittle materials such as intermetallic compounds, presumably due to the partially hydrostatic stresses existing during milling [57].

Through the action of heavy mechanical deformation during MM the grain size of single component systems can be reduced to nanometer scales [9, 51]. Plastic deformation generally occurs by slip and twinning at low to moderate strain rates, whereas at high strain rates it occurs by the formation of shear bands consisting of dense networks of dislocations [12, 51].

In the early stages of HEM of single component systems, the plastic strain in the material increases due to the increased dislocation density [51]. Deformation is localised in shear bands approximately 0.1 μm to 1 μm wide [1, 9, 51]. At a threshold dislocation density, nanometer-sized grains are nucleated within these shear bands due to the material relaxing into subgrains separated by low-angle boundaries [51]. This results in a decrease in atomic level strain. The process of high deformation and subgrain formation is repeated during subsequent milling, resulting in a further reduction in grain size and shear band coalescence [1, 51]. Low angle grain boundaries are replaced by high angle grain boundaries. The crystal lattice breaks up into nanosized grains with shear bands upon further deformation.

This ultimately leads to a material with an extremely fine-grained microstructure with randomly oriented grains separated by high angle grain boundaries [51]. Once the grains reach a critical size, further refinement becomes impossible since the stresses required for dislocation movement become enormously high. At this stage, amorphisation of the material may take place if further grain refinement is not possible [51].

2.4 Thermo-Mechanical Processing Techniques

Thermo-mechanical processing of powders to high density as well as achieving good interparticle bonding requires both high pressures and sufficient atomic diffusion across the interface between the particles [16]. External pressure applied will create shear forces at particle contact points and lead to local plastic flow and an increase in the density of the powder compact. As the shear stress produced is typically about half the applied pressure, an excessively large applied pressure must be applied to achieve significantly high densities in the milled powder at low temperatures. Alternatively, the temperature may be increased when the pressure is applied to reduce the flow stress of the powder [16].

To remove the porosity and to ensure diffusional bonding of the powder particles, which do not normally have atomically clean surfaces, the temperature needs to be

raised to allow diffusional transport of vacancies out from remnant pores and diffusional intermixing of atoms across the powder particle interfaces [16]. The temperature needs to be raised to between approximately one half and four-fifths of the melting temperature of the material in order to thermo-mechanically process the powders [38].

During thermo-mechanical processing, most of the metastability induced through HEM of the powders will be lost due at the elevated processing temperature [16]. Atomic transport over dimensions of the order of the grain size or particle size is required for thermo-mechanical processing. Grain coarsening will occur to a much larger scale since grain growth is a much more rapid process than vacancy transport, a mechanism required for pore removal [16]. Therefore the final grain size will be determined not by the intrinsic boundary mobility, but by other limiting factors such as grain boundary pinning by secondary particles or when the microstructure is composed of two interpenetrating phases which are not continuous throughout the material. The defects introduced during milling will anneal out, and grain growth and secondary grain recrystallisation can occur [16, 33]. The final structure will consist of the equilibrium crystal structure.

During sintering of conventional materials, pores are removed by sintering at high temperatures for long times, the driving force for pore removal being the reduction in surface energy. Nanophase powders also require high temperatures for densification, but the processing temperatures required are considerably lower than those required for conventional coarse-grained materials [58]. Lowering the sintering temperature can have a number of beneficial effects, such as a reduction in contamination and compositional changes, lower residual stresses and less cracking during cooling.

A number of factors contribute to this processing advantage. HEM produces a powder with a very broad size distribution, and this leads to easier filling of pores of different sizes [2]. The high dislocation densities in these powders also assist sintering. Due to these effects, densification is possible at relatively low temperatures. A disadvantage of these effects is that the diffusional processes

occurring during sintering lead to undesired grain growth and loss of the nanoscale grain size [2]. The driving force for grain growth increases as the grain size decreases, and therefore the enhanced sinterability that nanophase materials have is lost due to grain growth. The processing temperature therefore needs to be kept as low as possible so as to avoid grain growth, but high enough to effect sintering.

A reduced sintering temperature can be compensated for by using pressing and forging involving high pressures to enhance the contribution of plastic deformation to densification and bonding, rather than relying primarily on long range diffusion [2]. The enhanced ductility that nano-grained materials are purported to have at low temperatures can contribute to densification. Another advantage in employing high thermo-mechanical processing pressure is that high processing stresses ensures the disruption of any surface oxide films on the powder particles, which otherwise may degrade bonding and lead to a reduction in strength [2].

Compactability measures the ability to densify a powder under an applied load [2]. The compactability is expressed in terms of the green density, which is the volume of the green compact or the powder compact prior to thermo-mechanical processing. The green density is a percentage of the theoretical density of the material. Factors influencing the green density are interparticle friction, particle size, chemistry, lubrication and metallurgical properties [2]. Metal powders formed by milling exhibit poor compaction characteristics due to their work hardened state and irregular morphology [2, 38].

Most powders formed by MA are processed via hot compaction followed by hot extrusion, or by direct hot extrusion at temperatures greater than half the melting temperature of the material followed by thermo-mechanical processing to produce the desired grain structure [36, 38]. Pressing and sintering has not been a successful thermo-mechanical processing technique for powders formed by MA. The high hardness of the powders prevents cold pressing.

For most applications, the powders which have been produced via milling and now have a NC structure need to be processed by thermo-mechanical means, and therefore the thermal stability of the NC structure is very important. In comparison to thermo-mechanical processing of NC powders produced by other methods, powders milled at a high energy transfer rate exhibit promising thermal behaviour which may be related to the chemistry of the grain boundary. Nanosize powder particles prepared by the condensation of evaporated metal vapours in partial inert atmospheres when processed differ from the material resulting from thermo-mechanical processing of powders milled at a high energy transfer rate [36]. Materials prepared by evaporation-condensation have crystalline grains which are dislocation free, and are separated by clean grain boundaries which are only one or two atomic dimensions thick, whereas thermo-mechanical processing of powders milled at a high energy transfer rate results in a material consisting of crystalline grains separated by thick grain boundaries with a high dislocation density.

3. MATERIALS AND EXPERIMENTAL METHODS

3.1 Materials and Specimen Preparation

Material with a composition of Cu-24.6wt%Sn (hereafter referred to as CuSn) was produced using a previously described method [31]: Industrial purity copper and tin stock were sectioned into pieces not greater than 10 mm, weighed and mixed in the correct proportion. Granulated charcoal or carbon was added to the mix to control oxidation. The mix was placed in a ceramic crucible and then in a *Naber N11* resistance heated furnace preheated to 1000 °C. The melt was 'poled' with a green twig to de-oxidise it before pouring.

Pre-alloyed powders were produced via the following two routes: In the first route, the melt was cast by pouring into a steel mould. The second route involved pouring the molten alloy directly into water from a height of 1 m. In both cases, the resulting material was pulverised into a fine powder with a size not greater than 1 mm using a rock crusher and a mortar and pestle.

As no XRD data was available in the XRD peak matching software database (*JCPDS-ICDD* Copyright © 1992) regarding the β phase, α phase and γ phase, XRD was performed on cast material which had been heat treated to produce a single phase structure. CuSn was cast with the composition Cu-24.6wt%Sn (β eutectoid) for the β phase and Cu27.0wt%Sn (γ eutectoid) for the γ phase. After casting, the material was solutionised for 1 hour at 650 °C for the β phase and at 550 °C for the γ phase, and then quenched into iced brine to produce a single phase structure at room temperature. The α phase peaks were determined by annealing the milled elemental powder blend at 450 °C for 1 hour followed by XRD of the powder.

The microhardness of the α phase, β phase, δ phase and γ phase was determined in order to aid phase identification during ageing and thermo-mechanical processing of the milled powder. Samples of bulk CuSn were solutionised at 650 °C for 1 hour and quenched into iced brine in order to obtain a β phase microstructure at room

temperature. Samples of the quenched material were then solutionised for 1 hour at 550 °C to produce an α phase plus γ phase microstructure and 500 °C to produce an α phase plus δ phase microstructure, and then quenched into iced brine to retain these phases at room temperature.

Microhardness measurements were performed using a *Matsuzawa MXT-CX7* digital microhardness tester with a Vickers diamond pyramid indenter. Ten measurements were taken and the average microhardness value calculated.

Specimen preparation consisted of mounting the specimens in a cold-curing resin, followed by grinding on silicon carbide grinding pads to 1200 grit and polishing using diamond paste to a 0.25 μm finish. The mounted and polished samples were etched in acid ferric chloride (10 % HCl, 30 % water, 60 % methanol, 20 g/l $FeCl_3$) to obtain phase contrast [59].

3.2 Ageing of Quenched Bulk CuSn

The bulk quenched CuSn was aged over a range of temperatures. This was performed so as to provide a reference when comparing the properties of the powders produced via milling to the properties of the aged bulk CuSn. Specimens were sectioned from the bulk material after being solutionised at 750 °C for 30 minutes followed by an iced brine quench. The dimensions of these samples are approximately 20 mm × 10 mm × 5 mm. The material was aged at 150 °C, 200 °C, 310 °C, 370 °C and 500 °C.

The microstructure of the material was examined before being aged, after ageing, and after being aged to peak hardness for specimens which exhibited a significant difference between the final hardness and the peak hardness. A *Naber N11* furnace was used to solutionise the specimens. A molten salt bath was used for ageing at 310 °C, 370 °C and 500 °C, while an oil bath was used for ageing at 150 °C and 200 °C. These media were used to ensure rapid heating. The specimens were quenched in iced brine after each ageing period prior to hardness determination. The

samples were ground after each ageing period to provide a flat, clean surface for hardness determination and also to remove any oxidation scale or topographical change caused by phase changes during ageing.

Hardness measurements were performed on an *Eseway* hardness tester using a Vickers diamond pyramid indenter and a 30 kg load. Five measurements were taken per interval, and the average, maximum and minimum hardness values determined using standard tables. Optical photographs were taken on a *Reichert MeF3A* microscope with a *Yashika 108* camera. The microhardness of the phases formed during ageing was determined in order to aid phase identification.

3.3 Milling

HEM of CuSn powder was undertaken as follows: The initial powder charge was milled in a reducing gaseous environment of Ar + 2% H_2 in the presence of hexane in a water cooled attrition mill for 48 hours using a shaft speed of 222 rpm and a ball to powder weight ratio of 10:1. The mill is shown in Figure 3.1.

The apparatus used in this study was modified to gain more control over the milling conditions and to speed up sampling as the mill was not originally designed for HEM. The mill was prone to oxygen contamination which caused the powder to become highly oxidised and therefore useless for further thermo-mechanical processing. A flexible seal was added between the stirrer shaft and the mill chamber opening to limit oxygen contamination.

The sampling time was reduced by the addition of four toggle clamps to the mill chamber lid, and the insertion of a removable mill chamber into the shell of the mill. The stirrer arm was also brought closer to the base of the mill chamber, as it was found that the powder charge tended to sink to the bottom of the chamber where conditions were stagnant. These modifications are shown in Figure 3.1 and Figure 3.2.

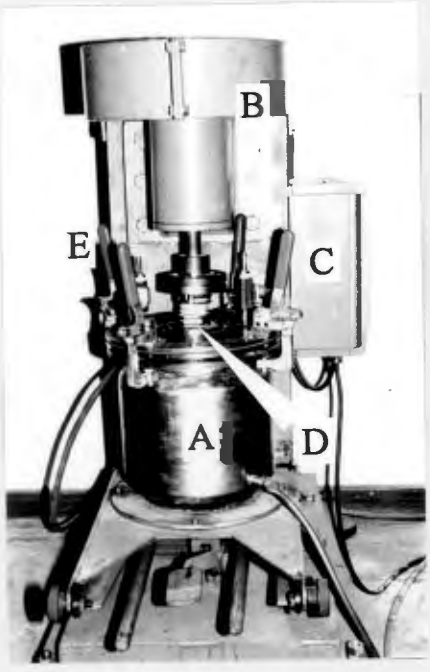

Figure 3.1: Photograph of mill used in this study showing attrition mill chamber (A), attrition mill stand and motor housing (B), speed controller (C), flexible coupling (D) and toggle clamps (E).

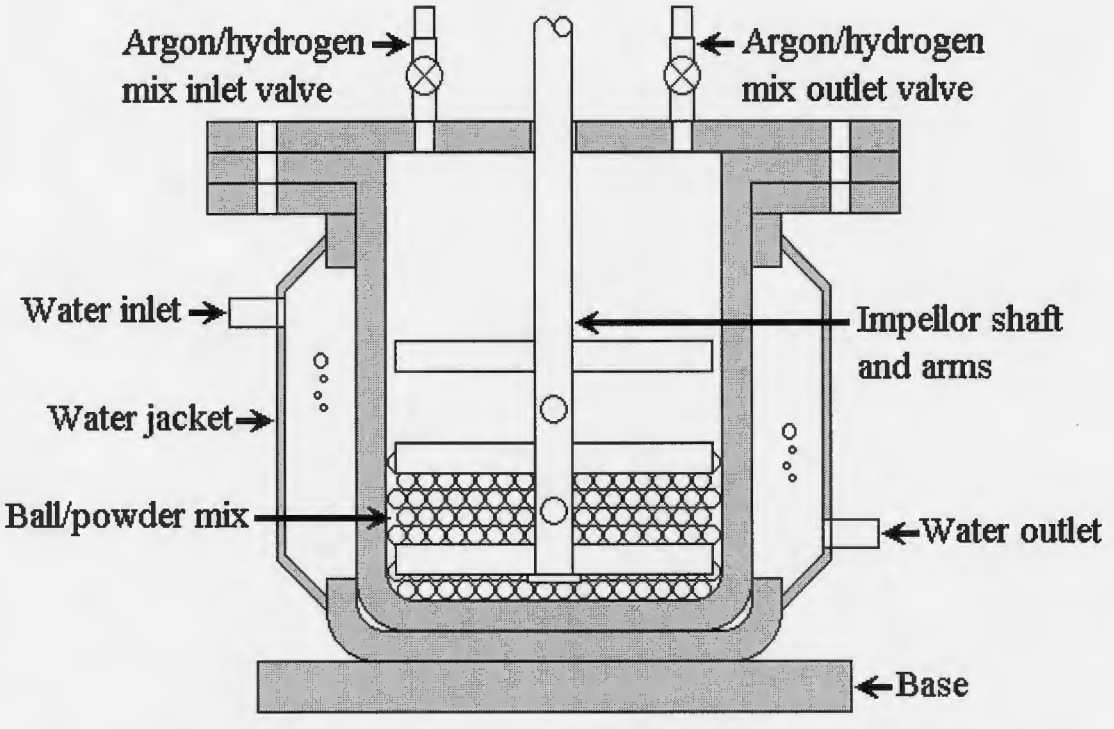

Figure 3.2: Internal view of the milling equipment after modification. (Not to scale. Flexible coupling not show.)

Three initial CuSn powder charges were milled. They were a mix of elemental copper and tin powder, and the two pre-alloyed powders produced via the method outlined in section 3.1. The milling balls are high chromium steel ball bearings with a diameter of approximately 6 mm and a hardness of 816 HV. A reducing environment was used to reverse any oxidation which might occur during milling.

Due to the ductile nature of the powders, dry milling caused cold welding to dominate over fracture during milling, causing excessive powder agglomeration. In addition, dry milling caused the majority of the powder to stick to the container walls and not participate in the milling process. This slowed milling down considerably and produced a powder with inhomogeneous properties. For this reason, hexane (C_6H_{14}) was added to the powder as a surfactant to limit cold welding and thus provide a uniformly processed powder. The same result was found when comparing wet milling to dry milling of copper and zinc, another ductile/ductile system [60].

One millilitre of hexane was added per gram of powder. Following milling, the hexane was removed by evaporation in a fume cupboard. MA of intermetallics using a *SPEX 8000*✧ shaker mill and between 6.0 ml and 6.5 ml of hexane has shown that between 0.08 g and 0.15 g of hexane is retained in a powder charge of 5 g over a 20 hour milling period [42]. The hexane decomposes into elemental carbon and hydrogen; the former component goes into solution while the latter may form hydrides.

Powder samples were drawn at times of 4 hours, 8 hours 24 hours and 48 hours during milling. The mill chamber was flushed with an argon/hydrogen gas mix to purge the chamber of any oxygen which was present before each milling period. Additional hexane was added if the powder charge had started to dry up. After milling, powder samples from each of the three powders were annealed at 450 °C for 1 hour so that the phases present in the milled powders and the annealed powders may be compared, and also to simulate the influence of the high temperature to which the powders would be exposed to during thermo-mechanical processing.

✧ Registered Trademark of Sytech Corporation, Houston, TX.

A *Cambridge Stereoscan 2000* scanning electron microscope (SEM) operated at 25 keV was used to examine the morphology of the milled powder. The powders were mounted on standard SEM stubs with a conductive adhesive for examination.

The microstructure of the final powders were examined in a *JEOL 200CX* transmission electron microscope (TEM) operated at 200 keV. The powder was suspended in a methanol ultrasound bath and then deposited onto an electron-transparent carbon film, supported by a copper grid, with the aid of a pipette. The grain size range of the final powders was determined directly from TEM observations.

The electron diffraction patterns (EDPs) of the milled powders have been analysed in order to determine the phases present in the samples. The radii r of the EDPs have been converted into an interplanar spacing distance d using the formula:

$$d = L\lambda/r \qquad \text{...Equation 1}$$

where L is the camera length (a uniform length of 82 cm has been used throughout) and λ is the relatavistically corrected electron wavelength (2.5 pm) [61]. These interplanar spacings have been compared to tables of interplanar spacings (Appendix A) for the various phases which are expected to be present, and to the experimentally determined d-values from XRD.

Microhardness measurements were performed on the powder drawn during milling by mixing the powder in a cold-curing resin and then polishing the sample using the same metallographic procedure described previously. This technique provided flat sections of the individual powder particles supported in a resin matrix. Ten microhardness measurements were taken for each sample drawn. In addition, the morphology of the flat powder sections was examined using an optical light microscope.

The ageing behaviour of the bulk CuSn was determined using bulk hardness measurements, while the hardness development of the milled powders was determined

using microhardness measurements. These measurements cannot be directly compared as they were determined under different test conditions. In order to facilitate comparison, microhardness and bulk hardness tests were performed on aluminium, copper and bronze. The results of this test are presented in Figure 3.3.

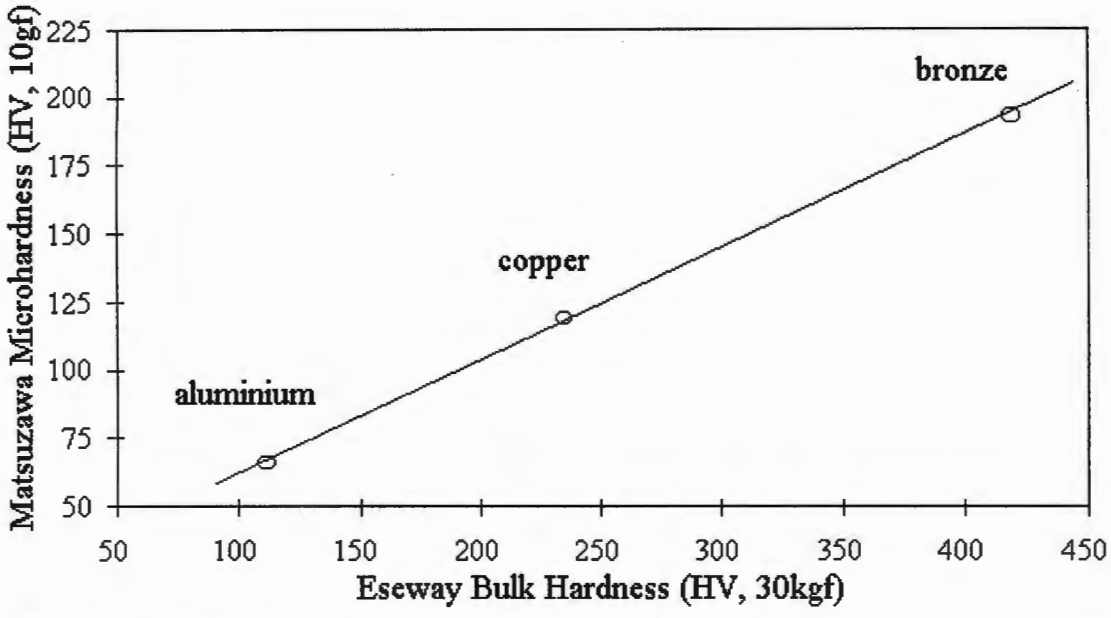

Figure 3.3: Plot of *Eseway* bulk hardness versus *Matsuzawa* microhardness for aluminium, copper and bronze (CuSn).

The graph yields a straight line equation which converts the bulk hardness H_b to an equivalent microhardness H_m:

$$H_m = 0.414H_b + 19.8 \qquad \text{...Equation 2}$$

All subsequent hardness data will be quoted either as true or converted microhardness values in this report.

X-ray diffraction (XRD) scans were performed on the milled powders, in order to determine the degree of milling and the phase changes during milling, as well as on the annealed powders. The instrument used was a *Philips PW1130/90* diffractometer with Cu K_α radiation. The scan range selected was 2θ= 25.0 ° to 55.0 °. Scanning

was performed in step mode with a step size of 0.1 ° and a scan time of 1 second per step.

The XRD diffraction peaks were labelled by converting the interplanar distances of the relevant phases into diffraction angles using the Bragg equation [2]:

$$2\theta = 2\sin^{-1}(\lambda/2d_{hkl}) \qquad \text{...Equation 3}$$

where 2θ is the diffraction angle, λ is the wavelength of the X-ray radiation (1.542 Å for Cu K_α radiation) and d_{hkl} is the interplanar spacing (sometimes referred to as the *d*-spacing or simply *d*) where *hkl* are the Miller indices of the plane. Tables listing the *d*-spacings, intensities and diffraction angles of the phases relevant to this study are presented in Appendix A.

3.4 Thermo-Mechanical Processing of Milled Powders

Three thermo-mechanical processing techniques were employed, namely sintering, hot isostatic pressing and a modified powder forging method. The production of a bulk material by thermo-mechanical processing of the cast powder which had been milled for 48 hours is described in the following sections.

3.4.1 Pressureless Sintering

The milled cast powder was sintered for 1 hour at 400 °C, 500 °C and 600 °C in a static reducing atmosphere of Ar + 2% H_2 gas with a positive pressure of 30 kPa. A compaction pressure of 830 MPa was used to form green powder compacts for sintering. The microstructure of the pellets was examined to determine the phases present after sintering, and to determine, according to the microstructure, the degree of sintering.

The microhardness of the sintered pellets was measured in order to determine the optimum sintering temperature. The grain size and density was determined using

lineal analysis, and the porosity of the compacts determined before and after sintering using point counting.

3.4.2 Hot Isostatic Pressing

Hot isostatic pressing or HIP was used to process the milled cast powder into a bulk form. The powder was degreased before HIP using acetone, and the powder encapsulated or canned using a mild steel capsule. HIP was performed at 500 °C for 3 hours at 55 MPa in a recycled argon environment. As the HIP service was rendered free of charge, no influence over the processing parameters was possible.

The HIPed compact was mounted, polished and etched following the procedure outlined in section 3.2, and examined in the optical microscope. The microhardness of the compact was determined using the same procedure as before, as was the porosity, density and grain size.

3.4.3 Hot Uniaxial Pressing

The milled cast powder was processed using a combination of uniaxial pressing and resistance heating. This process is hereafter referred to as hot uniaxial pressing or HUP. The apparatus used for thermo-mechanical processing is shown in Figure 3.4. The apparatus used was an *ESH* (*Electro Server Hydraulic*) tensometer with a 250 kg load cell and a compression stage. Steel jaws were machined from *Bohler V155* steel. The jaws were hardened by heating to 860 °C for 1 hour and then quenched into oil, followed by tempering at 540 °C for 30 minutes. This heat treatment gave the jaws a hardness of 386 HV.

Green compacts with dimensions 3 mm × 10 mm ∅ were produced by cold compacting the powder at a pressure of 25 MPa. A 1.5 mm hole was drilled into the side of the green compact or pellet so that the temperature could be monitored during thermo-mechanical processing by inserting a thermocouple into the hole. The thermocouple used is a nickel-chromium thermocouple with a reference junction at

0 °C, and the temperature was monitored with a *Philips PM2535* multimeter using a voltage to temperature conversion table.

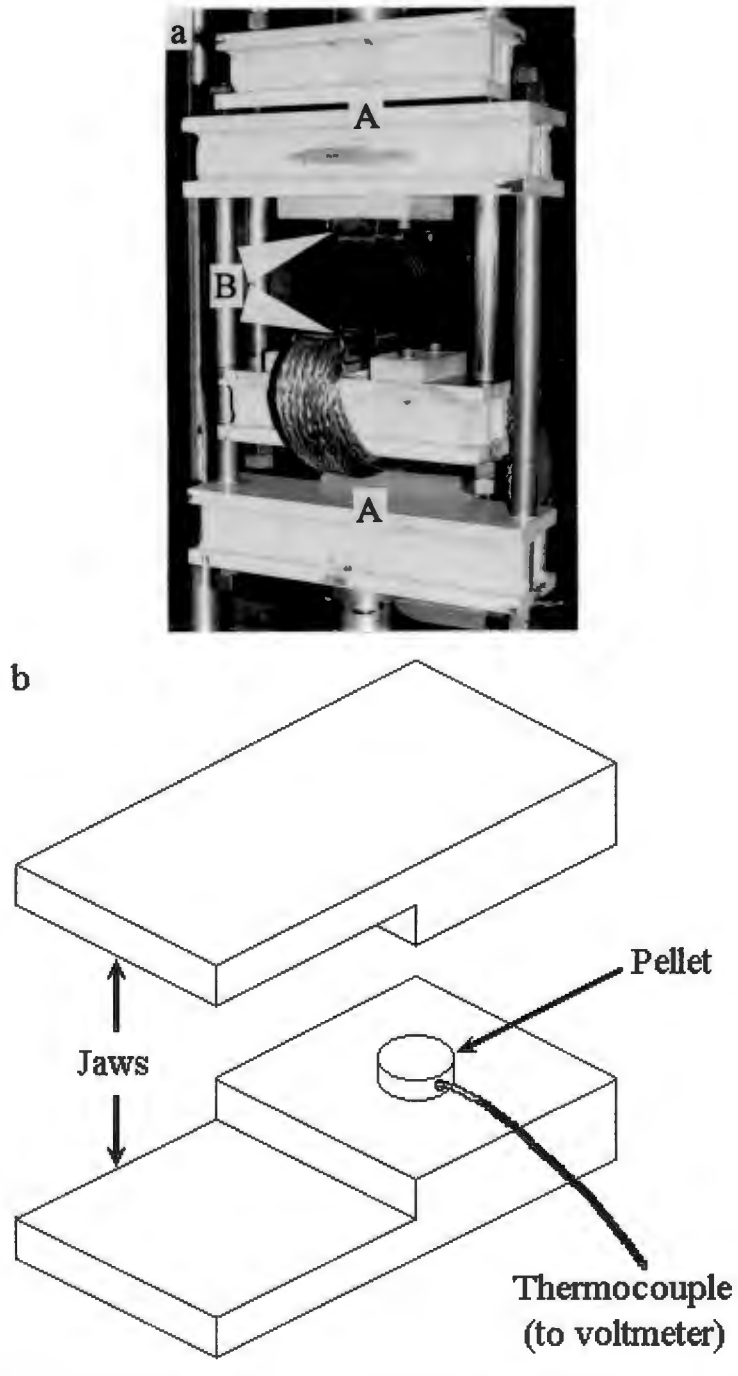

Figure 3.4: Figure showing (a) a photograph of the *ESH* with compression stage (A) and jaws with electrical contacts (B), and (b) a schematic diagram of the experimental apparatus for HUP.

The pellets were processed using the following procedure: A pre-load of 2 kN was applied prior to heating. The transformer was switched on causing the full current

generated to be applied to the pellet. Immediately following that the load was ramped to between 10 kN and 15 kN. The temperature was allowed to rise to 400 °C before the load was slowly increased to 80 kN, which gave a processing pressure of 840 MPa. The transformer was then turned off and the compact allowed to air cool to room temperature under the applied load.

The hot-pressed samples were mounted, polished and etched, and examined in the optical microscope. The microhardness, porosity, density and grain size of the compacts was determined using the same procedure as before.

4. RESULTS

4.1 Ageing of Quenched Bulk CuSn

Figure 4.1 shows the structure of quenched bulk CuSn prior to ageing. The structure consists of bands of beta martensite within a β phase matrix. As this martensite was formed by quenching the material into iced brine, the martensite formed is β′ phase martensite, and therefore the material used for ageing has a tin content between 22.0wt% and 24.1wt% [27, 28], and not 24.6wt% tin. A small percentage of tin may have been lost to oxidation during melting as reported in [31]. The average hardness of the quenched bulk CuSn was 106 HV.

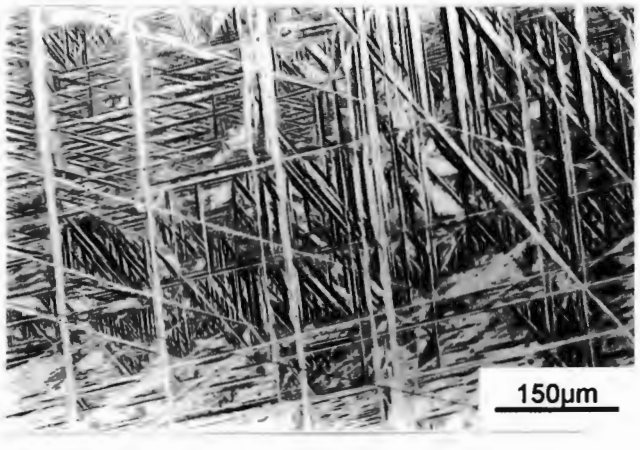

Figure 4.1: Optical micrograph showing the structure of the quenched beta phase which consists of bands of β′ phase in a β phase matrix.

The microhardness of the individual phases produced by solutionising and quenching the bulk material are shown in Table 4.1. Figure 4.2 shows the change in hardness of the quenched bulk CuSn aged at 150 °C as a function of ageing time.

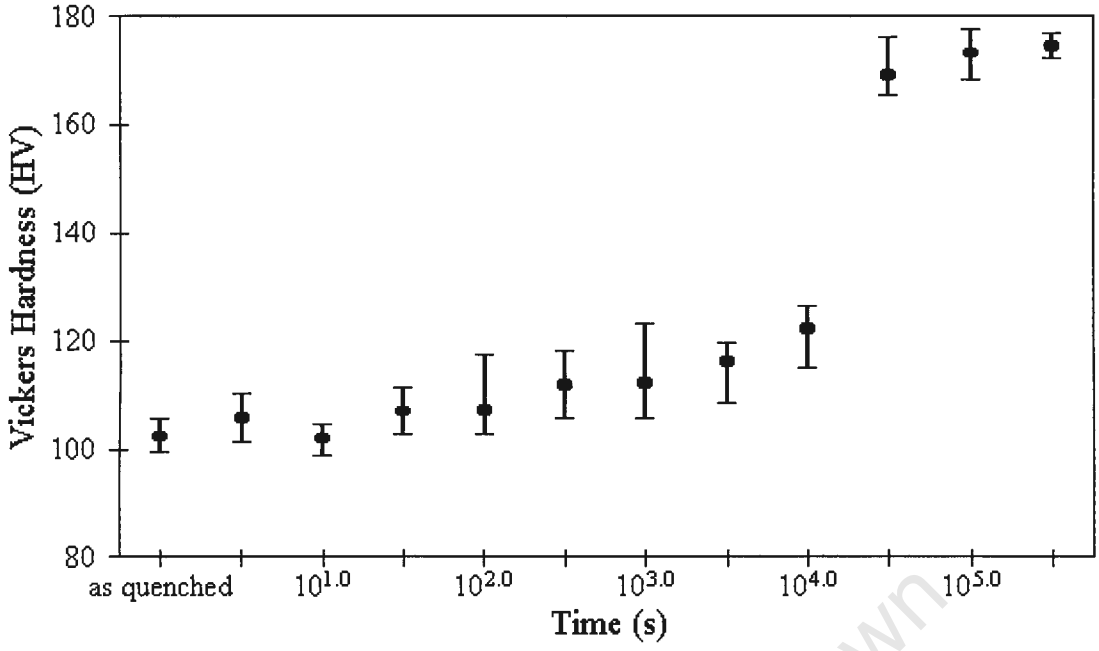

Figure 4.2: Graph of Vickers hardness versus log time for quenched CuSn aged at 150 °C. Maximum and minimum hardness values plotted as error bars.

Table 4.1: Microhardness of the phases produced by solutionising and quenching.

Phase	Microhardness (HV, 10 gf)
α	79.9
β	128
δ	177
γ	192

The specimen aged at 150 °C exhibits a small but steady hardness increase over the first $10^{4.0}$ seconds, then increases significantly over the next ageing period and reaches an average hardness of 169 HV after $10^{4.5}$ seconds of ageing. The hardness range does not increase beyond the upper limit of 176 HV thereafter. The material changes from being ductile to brittle after $10^{5.0}$ seconds of ageing, indicated by cracking at the corners of the hardness indent and chipping of the material at the indent corners and edges.

The same behaviour is exhibited during ageing at 200 °C (Figure 4.3), although the incubation period is much shorter ($10^{2.0}$ seconds). In addition, a slightly higher peak hardness of 175 HV is attained after $10^{3.0}$ seconds. Thereafter the hardness range does not increase beyond the upper limit of 180 HV. The ductile to brittle transition time decreases to $10^{3.0}$ seconds. The microstructure of the material after completion of ageing at both the ageing temperatures consists of an extremely fine distribution of a grey phase and a white phase, which is barely resolvable under optical microscopy at high magnification (×100), with an average size of 2.1 μm. The phases formed at ageing temperatures of 150 °C and 200 °C are thought to be α phase plus δ phase bainite, as the microstructure is similar to that encountered during ageing of quenched CuSn at 325 °C [31]. It has also been reported that supersaturated α phase and supercooled δ phase usually persist in the α phase plus ε phase equilibrium phase region [24, 26].

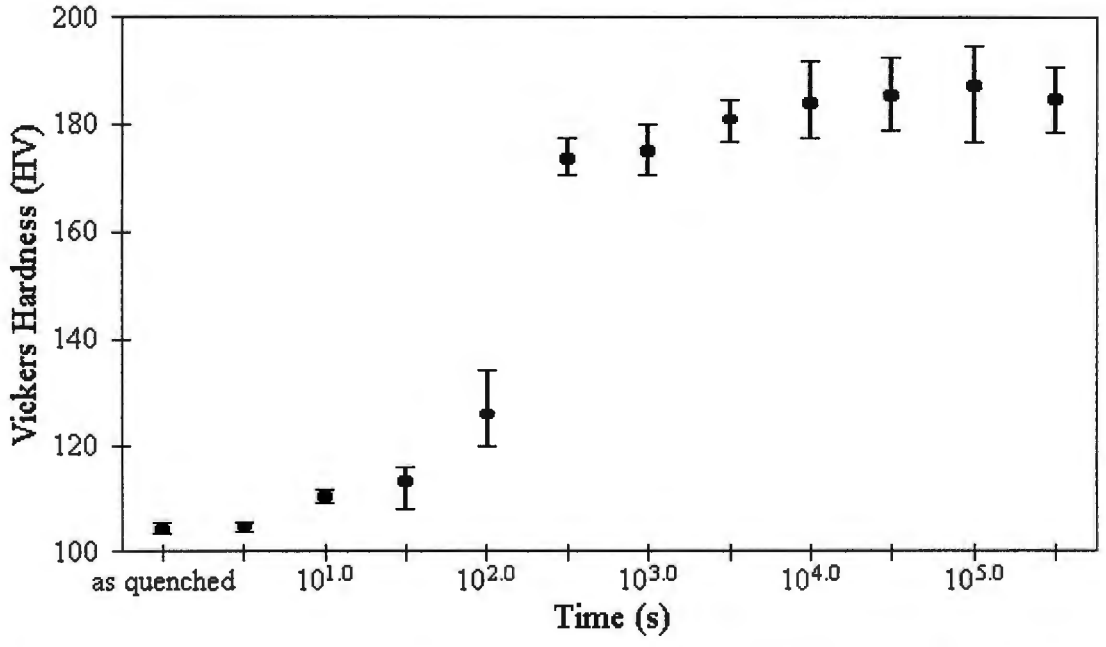

Figure 4.3: Graph of Vickers hardness versus log time for quenched CuSn aged at 200 °C. Maximum and minimum hardness values plotted as error bars.

The incubation time of the hardness development decreases to $10^{1.0}$ seconds for the specimen aged at 310 °C. From Figure 4.4 it can be seen that the hardness peaks at an average value of 186 HV after $10^{4.0}$ seconds of ageing. Thereafter, the experimental

range does not increase beyond the upper limit (196 HV) after $10^{4.0}$ seconds of ageing. The ductile to brittle transition time has decreased to $10^{1.5}$ seconds, and the material remains brittle for the remainder of the ageing period. The microstructure after ageing at 310 °C is shown in Figure 4.5, and is similar to that encountered at the two previous ageing temperatures. The size of the α phase and δ phase is approximately 2.4 μm.

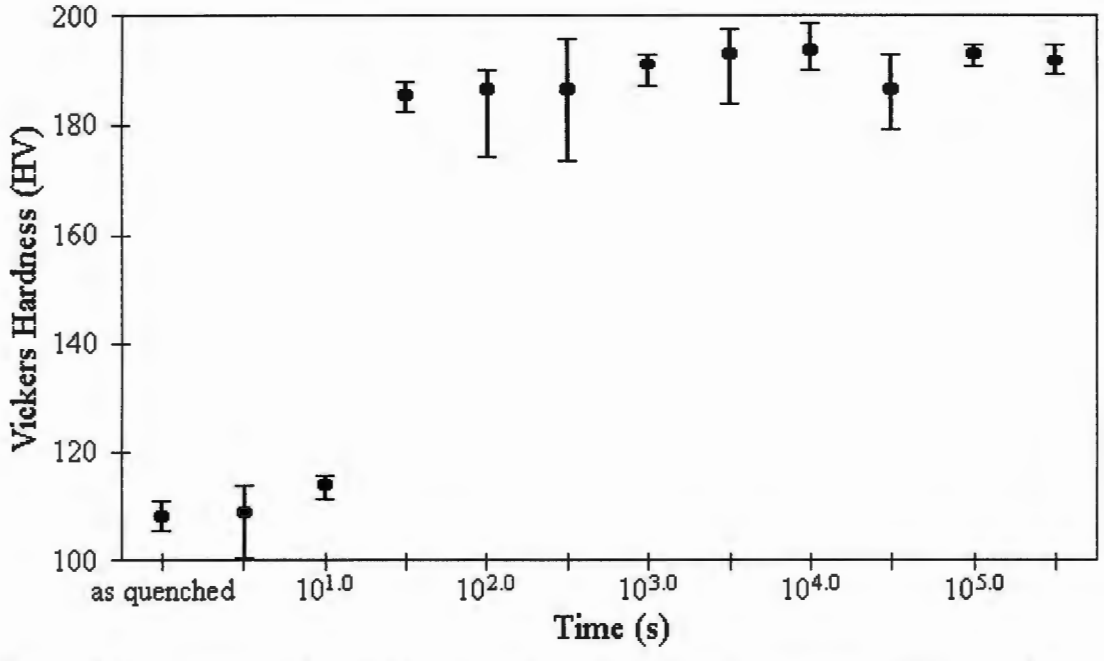

Figure 4.4: Graph of Vickers hardness versus log time for quenched CuSn aged at 310 °C. Maximum and minimum hardness values plotted as error bars.

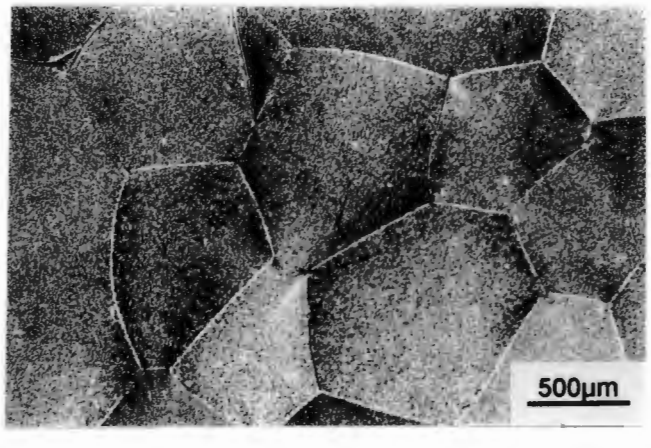

Figure 4.5: Optical micrograph of quenched CuSn aged at 310 °C for $10^{5.5}$ seconds showing the general structure which consists of a fine α phase (white) plus δ phase (dark) structure formed in the prior β phase grains.

There is no incubation period for the quenched bulk CuSn aged at 370 °C as seen in Figure 4.6. There is a steady increase in hardness over the first $10^{1.5}$ seconds, then after $10^{2.5}$ seconds the hardness peaks at 195 HV. Thereafter the hardness decreases to a minimum value of 170 HV after ageing for $10^{5.0}$ seconds. The material becomes brittle after ageing for $10^{1.5}$ seconds, indicated by cracking at the indent corners, and then reverts to being ductile again after $10^{4.0}$ seconds indicated by the disappearance of cracking at the indent corners. The microstructure appears the same as the structure after ageing at 310 °C, i.e. the structure consists of a fine distribution of the α phase and the δ phase with an average size of 2.5 μm.

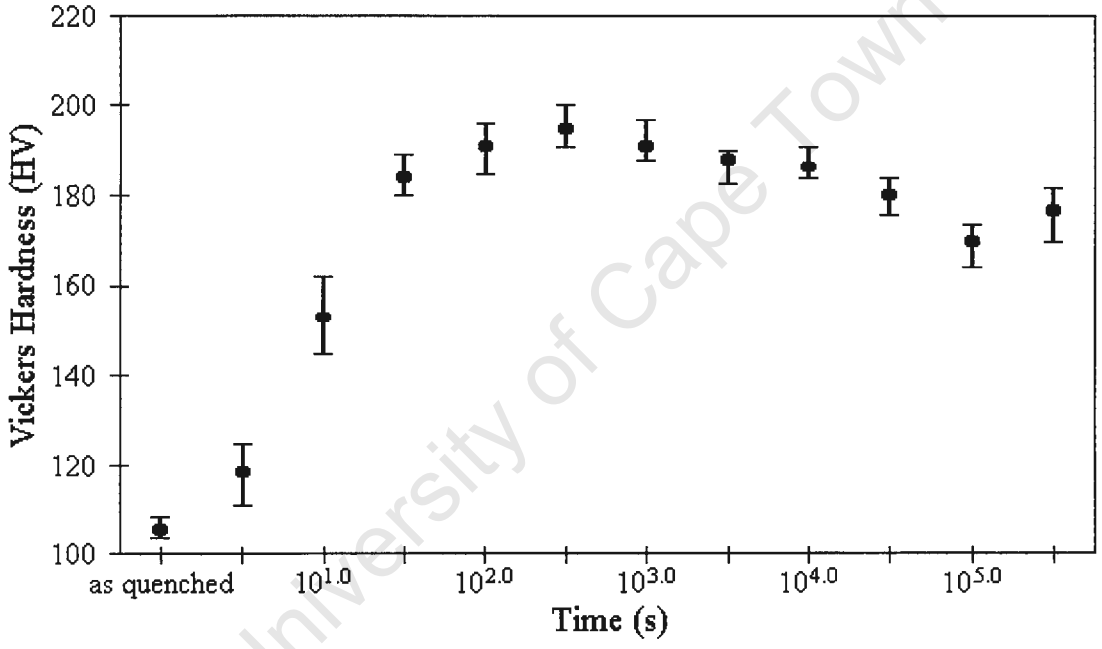

Figure 4.6: Graph of Vickers hardness versus log time for quenched CuSn aged at 370° C. Maximum and minimum hardness values plotted as error bars.

The bulk specimen aged at 500 °C exhibits a behaviour similar to the specimen aged at 370 °C, the difference being that the average peak hardness (184 HV) is reached after $10^{1.0}$ seconds, i.e. faster than the time to peak hardness for the material aged at 370 °C. After the peak value had been reached, the hardness decreases after $10^{5.5}$ seconds of ageing to an average value of 129 HV (Figure 4.7). The material becomes brittle after $10^{1.0}$ seconds of ageing, and then ductile again after $10^{2.5}$ seconds, indicated by the disappearance of cracking at the indent corners. The

microstructure of the material at its peak hardness appears the same as the microstructure for the material aged at 370 °C, that is, an extremely fine distribution of α phase and δ phase with an average size of 2.3 μm. At the end of the ageing period the microstructure consists of coarser α phase precipitates in a δ phase matrix as shown in Figure 4.8.

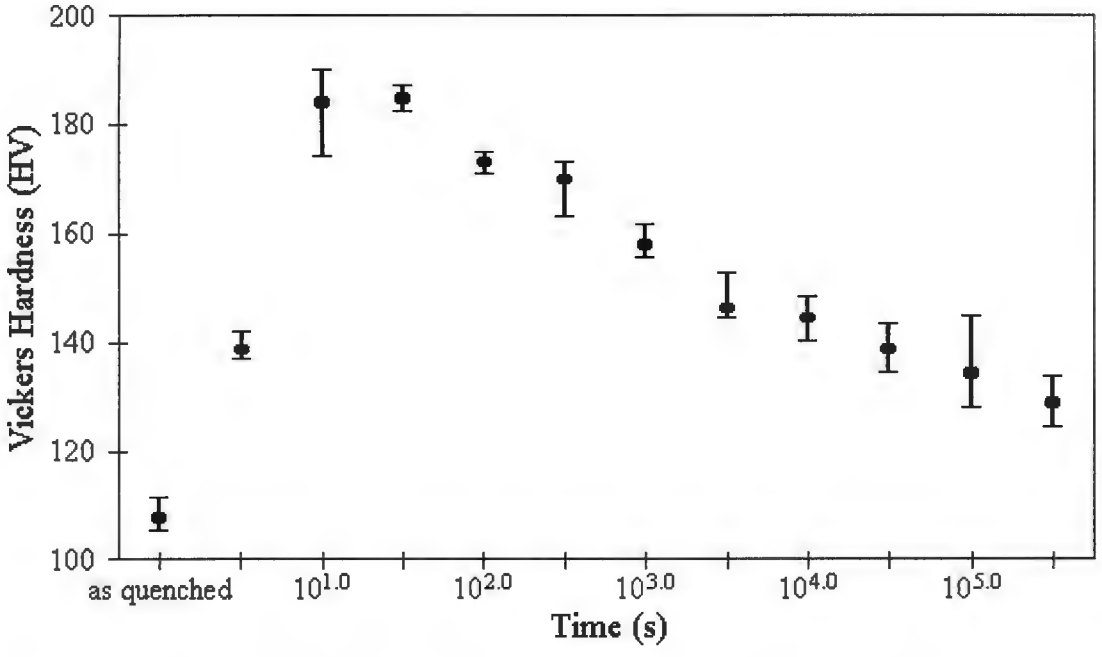

Figure 4.7: Graph of Vickers hardness versus log time for quenched CuSn aged at 500 °C. Maximum and minimum hardness values plotted as error bars.

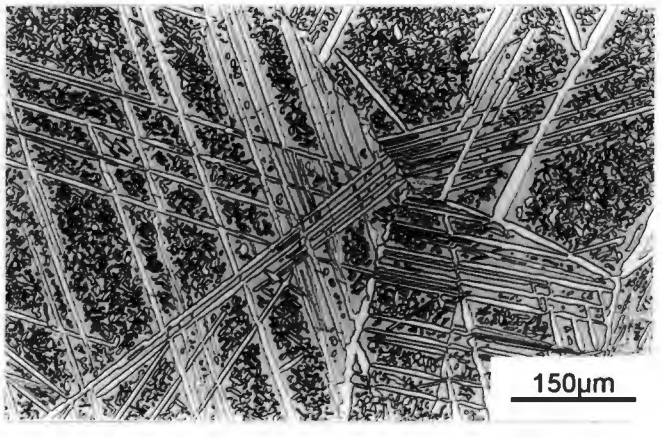

Figure 4.8: Optical micrograph of quenched CuSn aged at 500 °C for $10^{5.5}$ seconds showing precipitates and bands of α phase within a δ phase matrix formed in the prior β phase grains.

This result was confirmed by comparing the microhardness of the phases, 82.4 HV and 175 HV for the precipitates and matrix respectively, to the microhardness of known phases (Table 4.1), and by visual examination, as the α phase appears white and the δ phase grey under optical microscopy [31]. The grain size of the α phase precipitates has increased to 3.5 μm. Accompanying this change is the appearance of long bands of α phase with an average width of 4.0 μm. The α phase precipitates and bands may be oriented along the [1 1 1] direction of the previous β phase as reported in [62]. Due to the fine scale of the microstructure obtained at the lower ageing temperatures, microhardness testing could not be performed in order to confirm the identity of the phases precipitated.

The observed hardness response of the bulk material is typical of that of an age-hardenable material [14]. Phase precipitation has led to an increase in hardness with ageing time, and an increase in ageing temperature has led to a hastening of the onset of hardening, and in the case of the material aged at 500 °C, a loss in hardness due to overageing.

4.2 Morphological Development and Hardness Development of the Milled Powder

Three powders: 1) an elemental copper-tin blend, 2) a powder which had been cast and subsequently crushed, and 3) a powder which had been melt quenched and crushed (hereafter referred to as the elemental powder blend, the cast powder and the melt quenched powder respectively) were milled for 48 hours, and samples were drawn during milling for examination.

4.2.1 Elemental Powder Blend

Figure 4.9 is a series of SEM micrographs showing the morphological development of the elemental powder blend during milling. The initial powder consists of a mix of rounded copper and tin particles. After milling for 4 hours the morphology of the particles is plate-like, and the particles consist of layers of flattened elemental

particles which are welded together. After milling for 8 hours the powder consists of conglomerates of equiaxed particles. These particles become separated after milling for 24 hours, and after milling for 48 hours the powder consists of discrete rounded equiaxed particles.

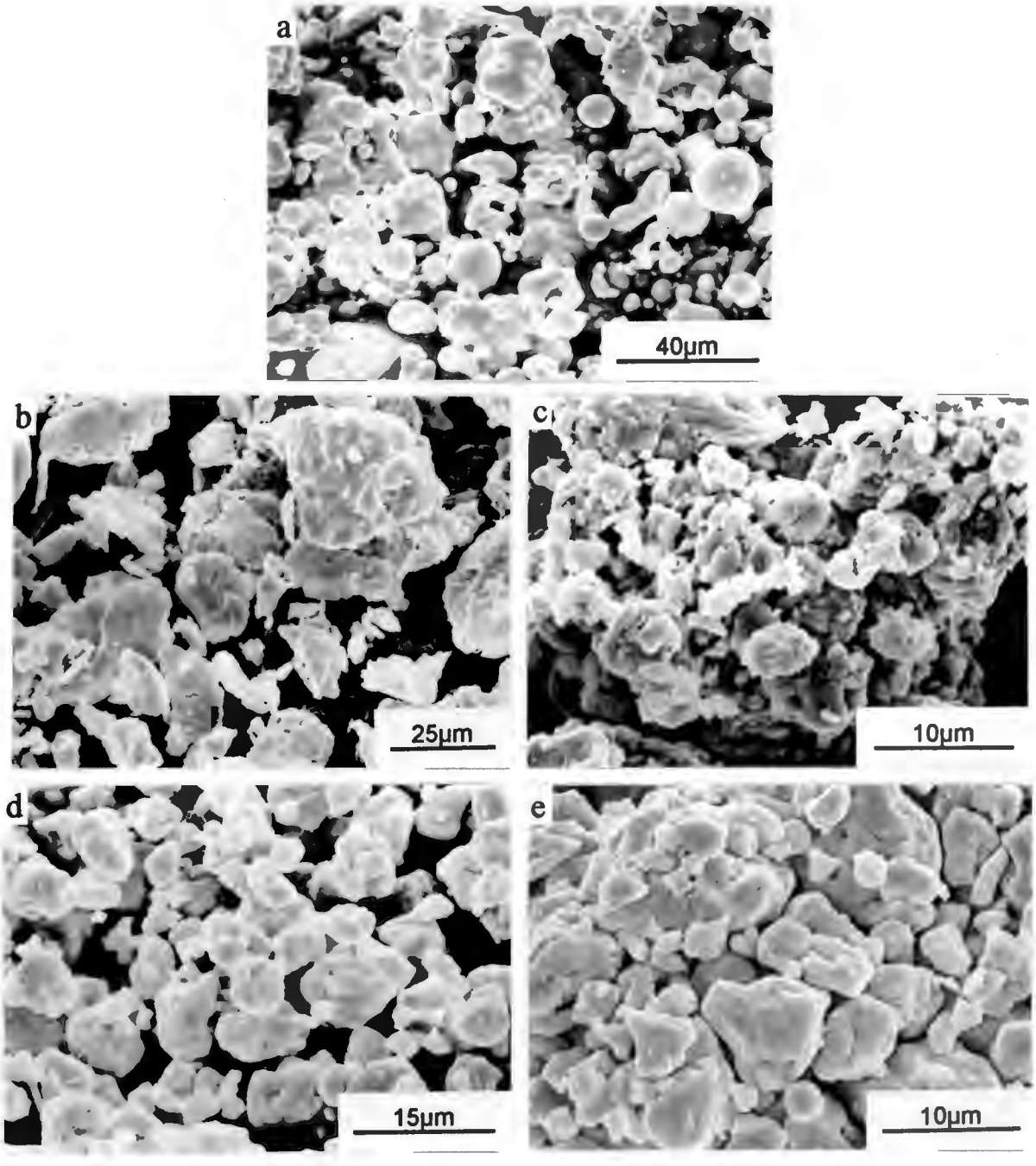

Figure 4.9: A series of SEM micrographs showing the morphological development of the elemental powder mix during milling. (a) Initial powder charge, milling for (b) 4 hours, (c) 8 hours, (d) 24 hours and (e) 48 hours.

Figure 4.10 shows the particle size of the elemental powder blend as a function of milling time. The initial powder consists of a mix of copper and tin particles with an average size of 9.9 μm ± 3.2 μm. After milling for 4 hours the average particle size has increased to 15 μm ± 5.1 μm due to the formation of welded flattened elemental particles. The average particle size decreases to 5.9 μm ± 1.8 μm after milling for 8 hours due to work hardening and fracture of the particles. There is no significant change in the particle size within the experimental range on subsequent milling.

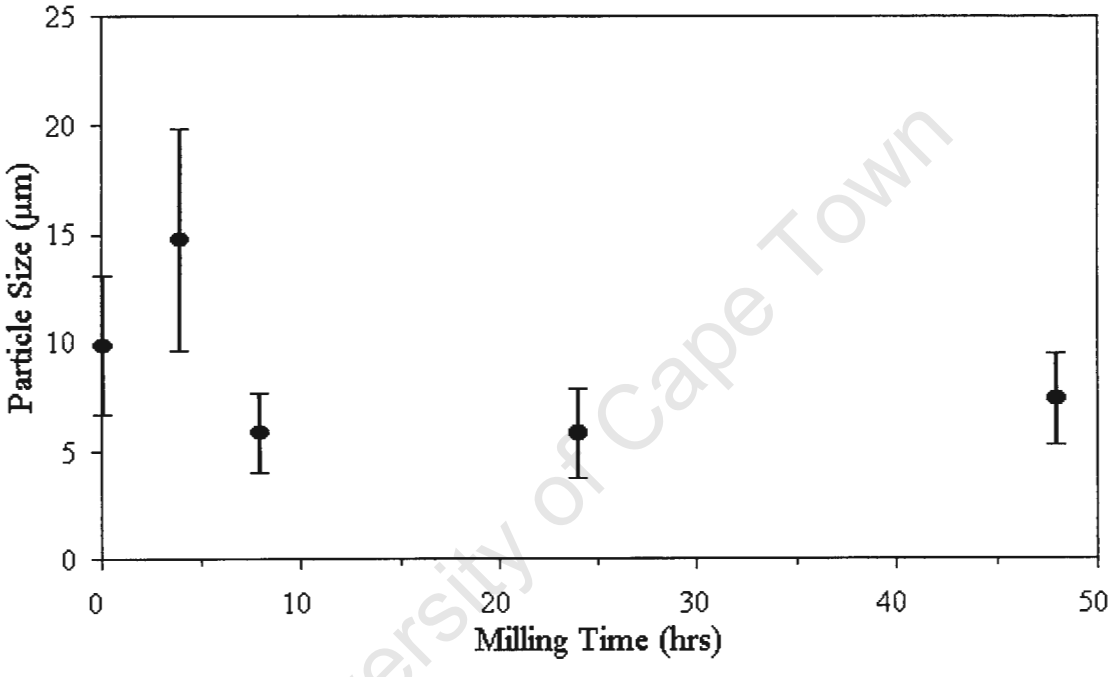

Figure 4.10: Graph showing particle size of the elemental powder blend versus milling time. Error bars are ± standard deviation.

Figure 4.11 shows the microhardness of the elemental powder blend as a function of milling time. The elemental copper and tin particles in the initial powder blend have a microhardness of 45 HV and 9.8 HV respectively. After milling for 4 hours the powder consists of particles comprised of flattened elemental particles which have become welded together, with an average microhardness of 118 HV. The average microhardness of the particles rises to 132 HV after milling for 8 hours with a maximum determined microhardness of 156 HV. The hardness of the particles does not rise significantly within the experimental range during further milling.

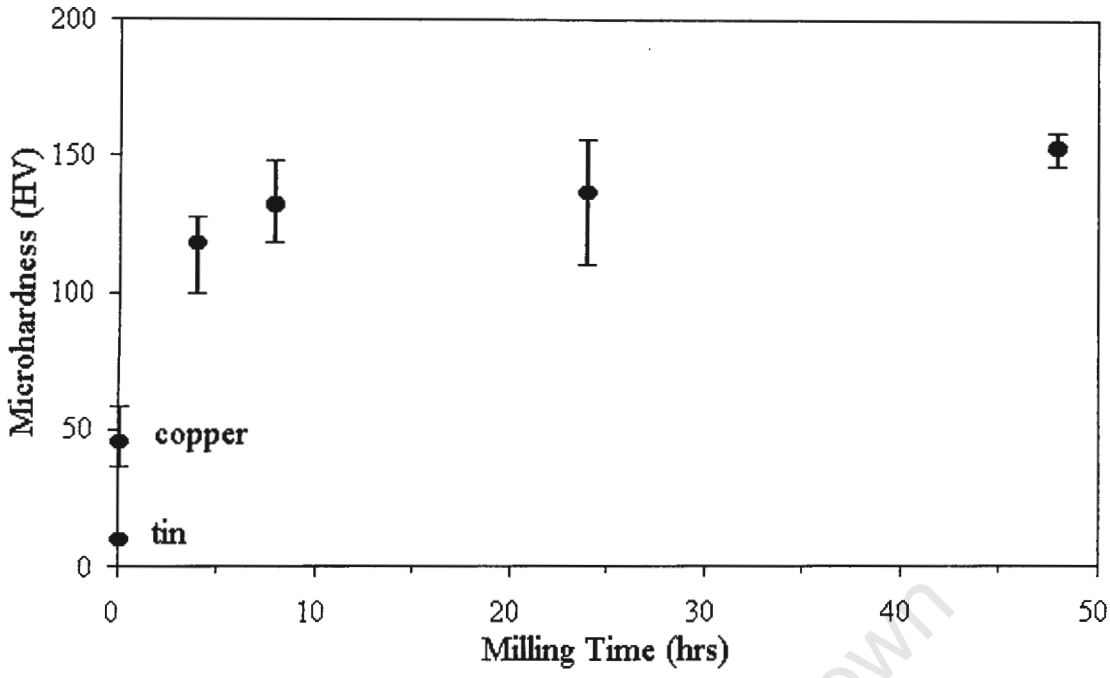

Figure 4.11: Graph showing the microhardness of the elemental powder blend versus milling time. Maximum and minimum values plotted as error bars.

Figure 4.12 is a SEM micrograph of an edge-on view of a plate-like particle obtained after milling the elemental powder blend for 4 hours. The micrograph shows that the particle consists of flattened elemental particles which are welded together to form a parallel lamellae structure when viewed edge-on. Figure 4.13 is a SEM micrograph of a cross-section through a particle obtained from the same sampling interval, obtained using back-scattered electron (BSE) detection in place of conventional secondary electron (SE) detection. This technique results in atomic number contrast between elements. The micrograph shows that the particle consists of elemental lamellae which are welded together.

Figure 4.14 is an optical micrograph of an elemental powder blend particle milled for 4 hours which has been mounted, polished and etched, and shows the same structure observed using SEM BSE examination, namely elemental particles which have become welded together. The etchant has attacked the tin component preferentially, and the micrograph reveals good welding between the two elements.

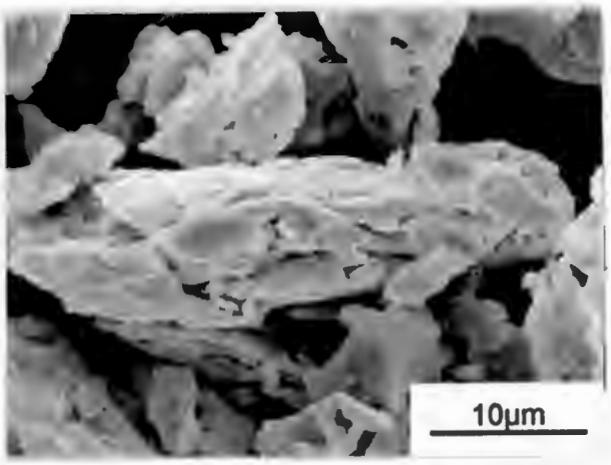

Figure 4.12: SEM micrograph showing an edge-on view of a particle from the elemental powder blend after milling for 4 hours.

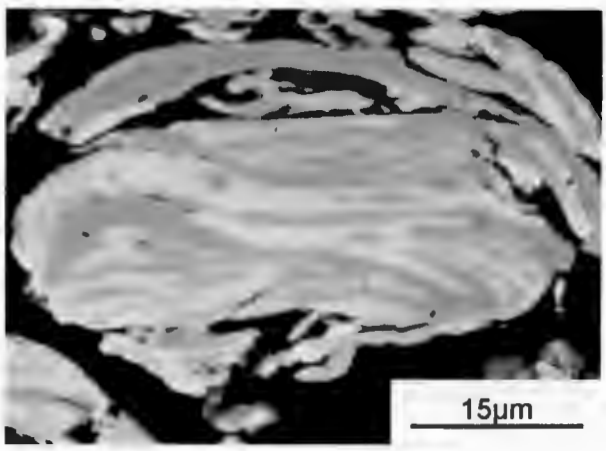

Figure 4.13: BSE SEM micrograph of a cross-section of a particle from the elemental powder blend after milling for 4 hours.

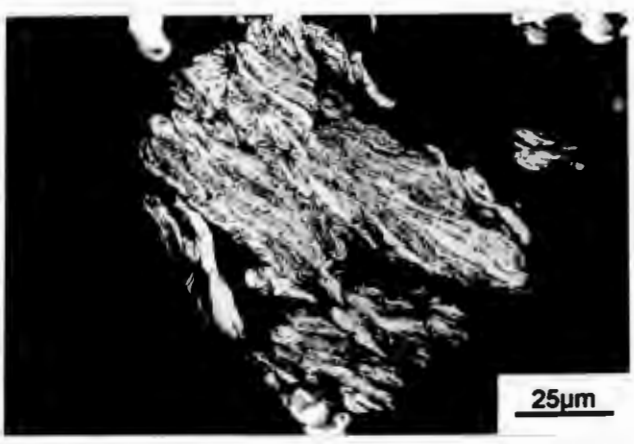

Figure 4.14: Optical micrograph of a cross-section of a particle from the elemental powder blend after milling for 4 hours.

4.2.2 Cast Powder

Figure 4.15 is a series of SEM micrographs showing the morphological development of the cast powder during milling.

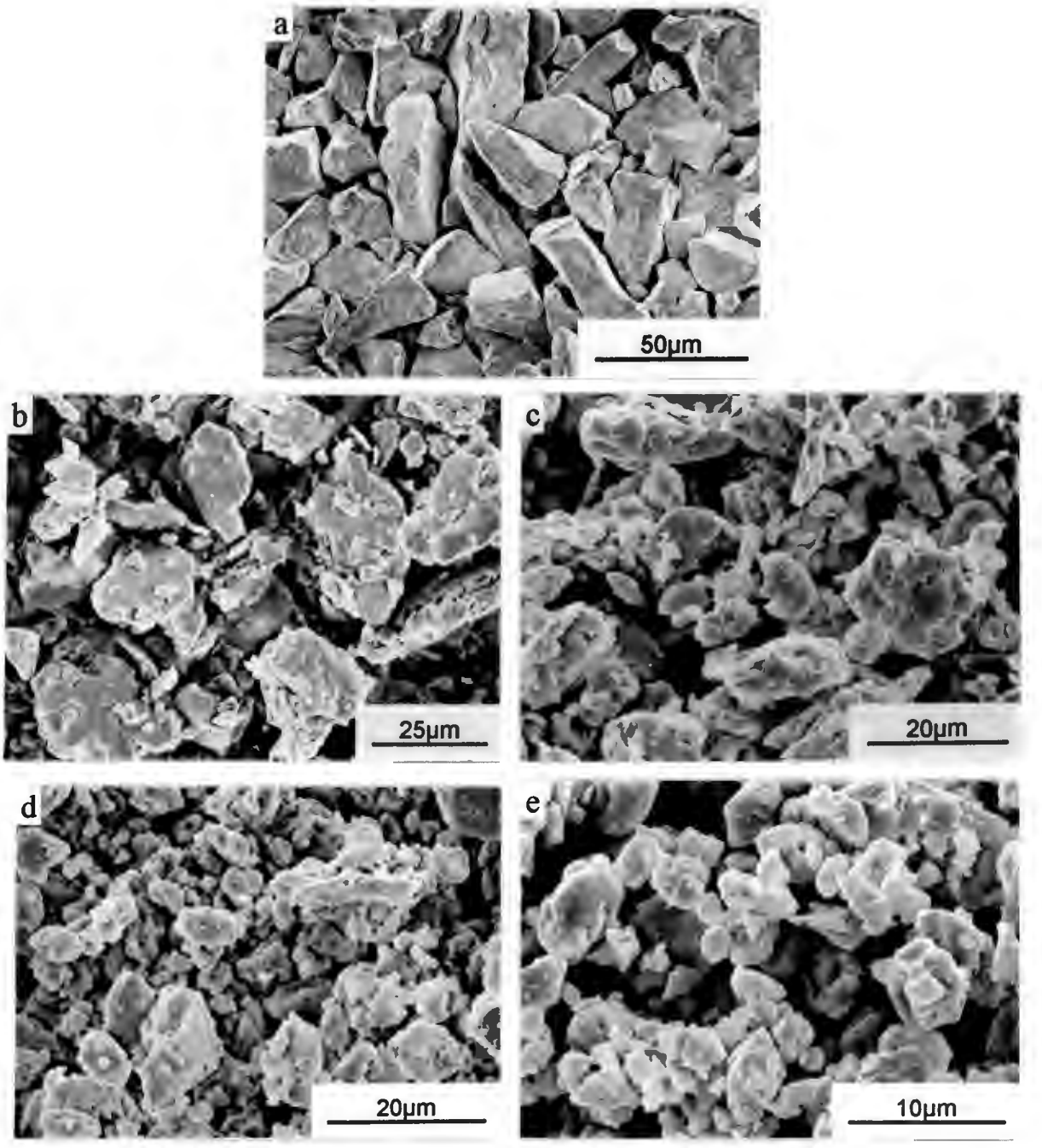

Figure 4.15: A series of SEM micrographs showing the morphological development of the cast powder during milling. (a) Initial powder charge, milling for (b) 4 hours, (c) 8 hours, (d) 24 hours and (e) 48 hours.

The initial powder consists of sharp-edged angular particles. After milling for 4 hours the powder consists mostly of conglomerates of smaller equiaxed particles which have become welded together. After milling for 24 hours the majority of the powder particles are equiaxed, but have become more rounded in appearance. Most of the conglomerates have disappeared. At the final stage of milling the conglomerates have disappeared completely, and the powder consists of discrete equiaxed particles.

Figure 4.16 is a graph showing the particle size of the cast powder as a function of milling time. The initial powder has a size of 71 μm ± 36 μm. After milling for 4 hours the particle size decreases to 8.7 μm ± 3.8 μm, and does not change beyond the experimental range on subsequent milling.

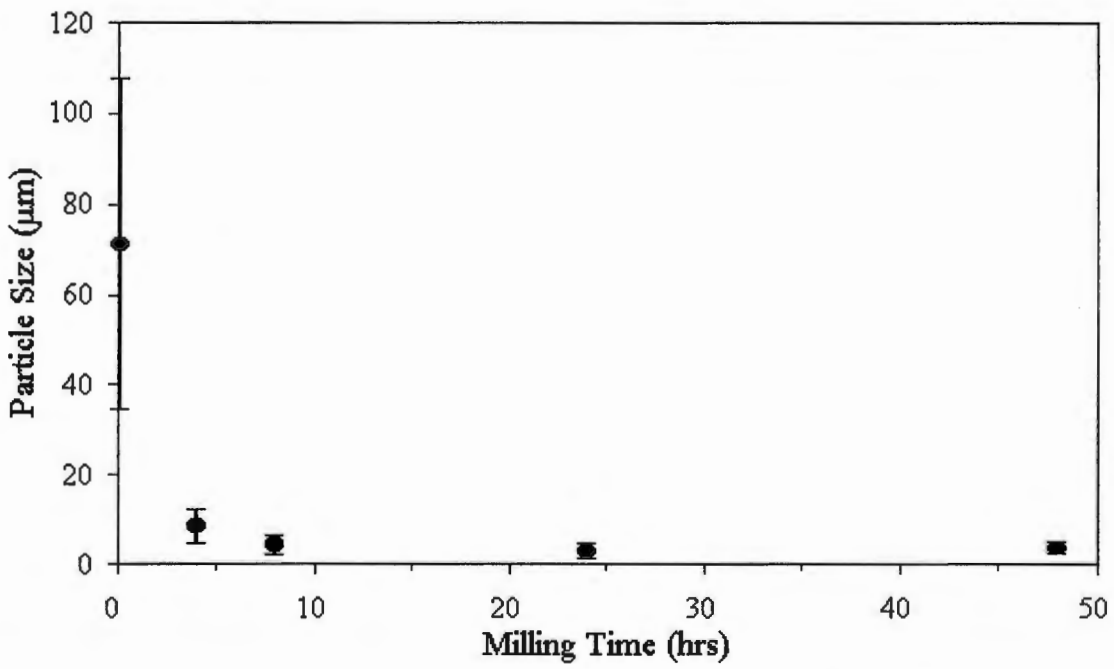

Figure 4.16: Graph showing particle size of the cast powder versus milling time. Error bars are ± standard deviation.

The average microhardness of the starting particles is 182 HV. The microhardness of the particles decreases during milling to an average microhardness of 143 HV after milling for 48 hours. This is not a reliable indication of the microhardness of the powder because as milling progresses, the particle size decreases until a level is

reached a where the particles are not big enough to support the microhardness indenter.

Figure 4.17 is an optical micrograph of a cast powder particle after milling for 4 hours which has been mounted, polished and etched. It shows two powder conglomerates which consist of smaller flattened particles loosely welded together.

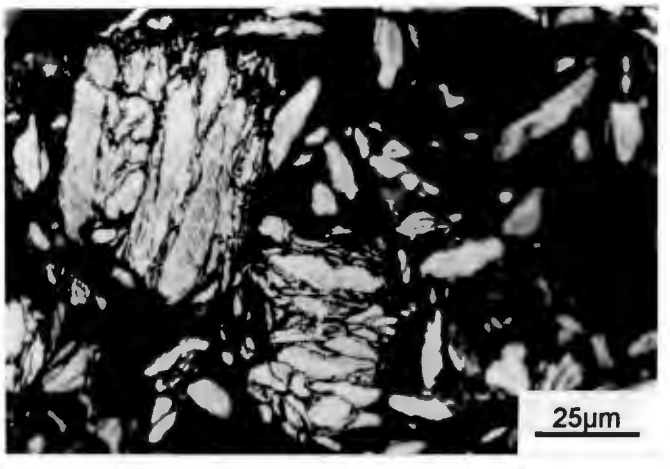

Figure 4.17: Optical micrograph of a cross-section of a particle from the cast powder after milling for 4 hours.

4.2.3 Melt Quenched Powder

The morphology of the melt quenched material prior to pulverisation is shown in Figure 4.18. The material is in the form of irregularly shaped splats ranging from 2 mm to 20 mm in size with a through thickness between 50 μm and 2 mm. During pulverisation of the splats, fracture has taken place predominantly via intergranular fracture, as shown by the many grain facets on the through thickness fracture surface in Figure 4.19.

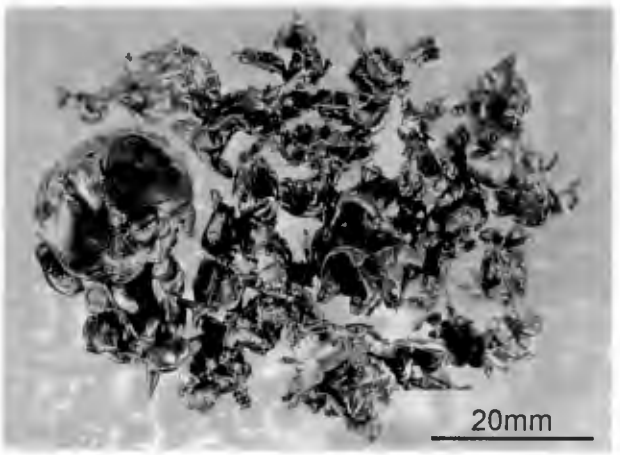

Figure 4.18: Optical micrograph showing the morphology of the melt quenched material prior to pulverisation.

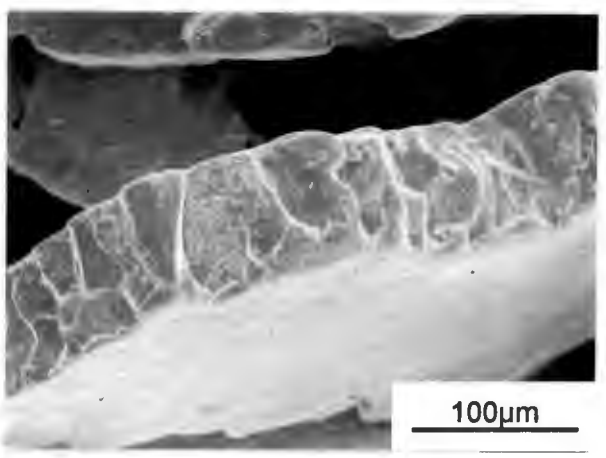

Figure 4.19: SEM micrograph of a through thickness fracture surface of a pulverised melt quenched splat.

Figure 4.20 is a series of SEM micrographs showing the morphological development of the melt quenched powder particles during milling. The initial powder consists of flat, smooth-surfaced particles with rough, square edges where fracture has taken place. The morphology of the particles has not changed from that of the initial powder after milling for 8 hours. After milling for 24 hours the powder morphology changes to a mix of flat, plate-like particles and equiaxed particles. After milling for 48 hours the powder consists of equiaxed particles.

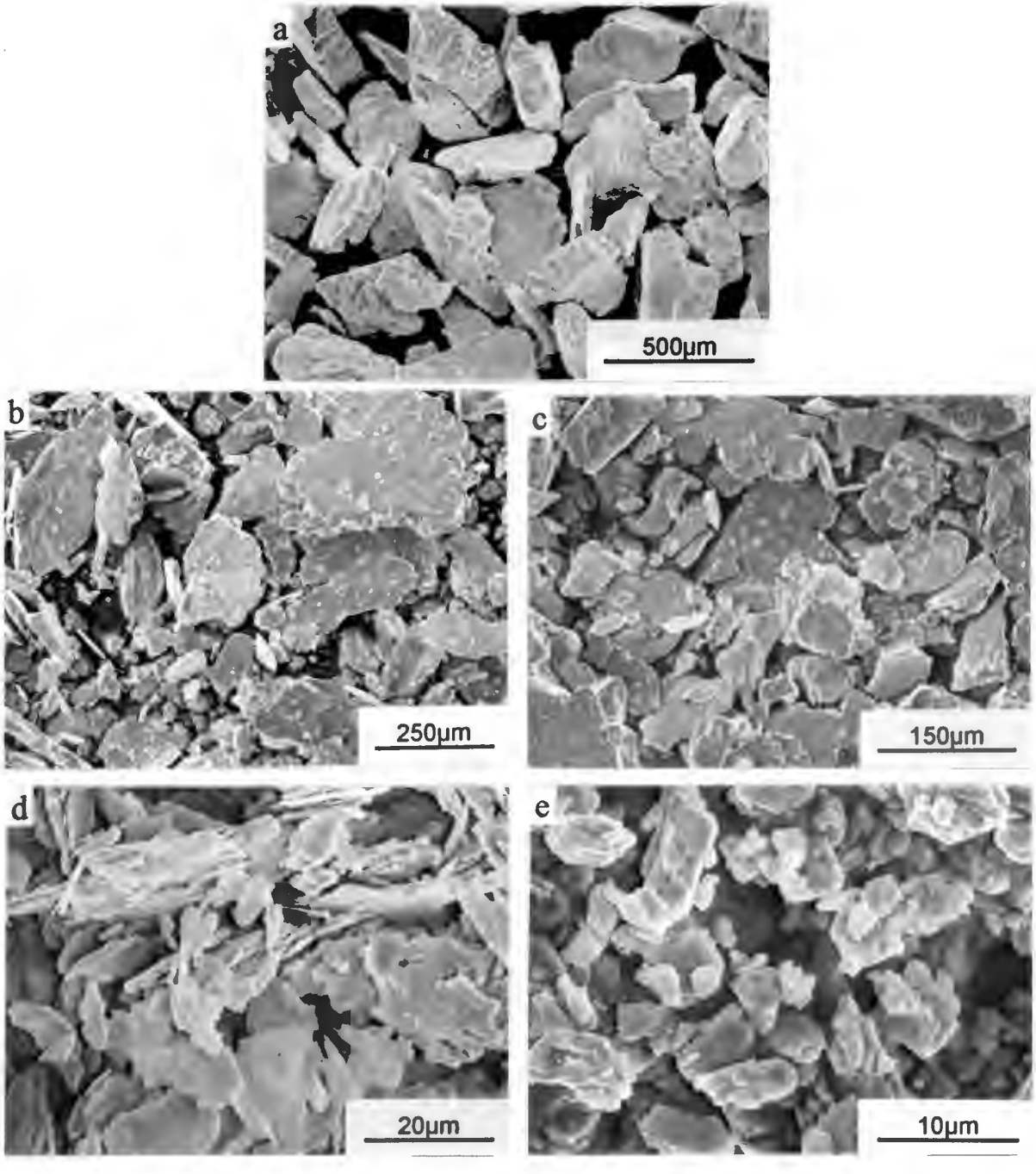

Figure 4.20: A series of SEM micrographs showing the morphological development of the melt quenched powder during milling. (a) Initial powder charge, milling for (b) 4 hours, (c) 8 hours, (d) 24 hours and (e) 48 hours.

Figure 4.21 is a graph showing the particle size of the melt quenched powder as a function of milling time. The size of the initial powder is in the range 104 µm ± 28.1 µm. The particle size decreases linearly to 51.7 µm ± 27.4 µm after milling for 8 hours. After milling for 24 hours the average particle size and experimental range

has decreased, and the particles are in the 8.2 μm ± 3.6 μm size range. On subsequent milling the particle size does not change beyond the experimental error.

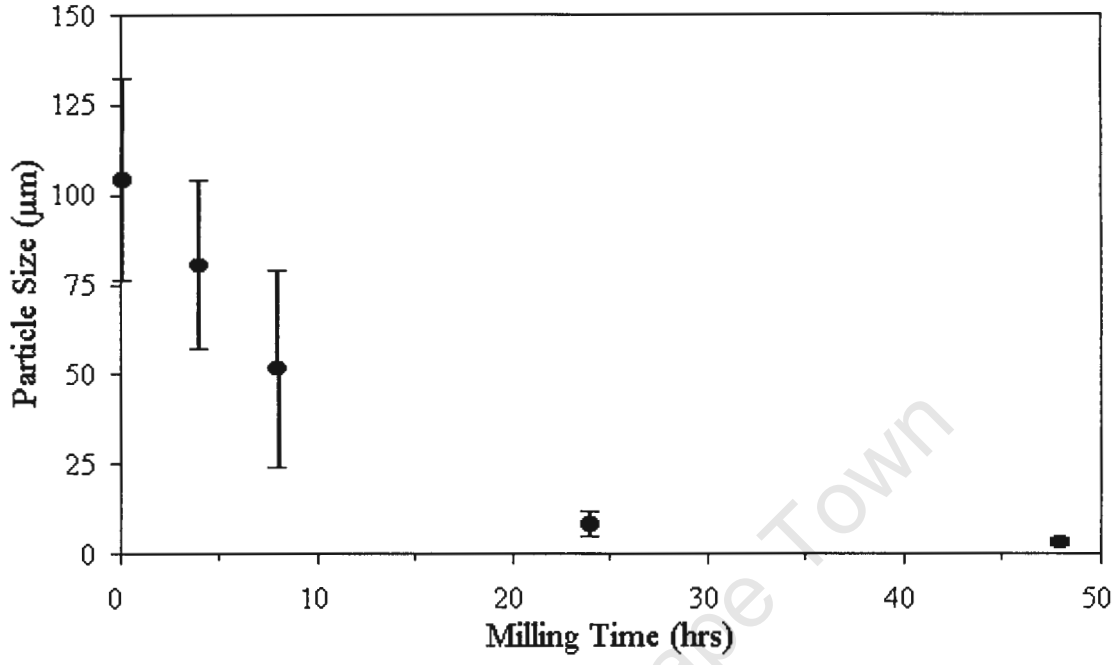

Figure 4.21: Graph showing particle size of the melt quenched powder versus milling time. Error bars are ± standard deviation.

The initial melt quenched particles have an average microhardness of 161 HV. After milling for 4 hours and 8 hours the average microhardness of the particles is unchanged. The microhardness development during subsequent milling could not be determined as the particles became too small for accurate microhardness measurement.

Figure 4.22 is an optical micrograph of a large particle from the sample drawn after milling for 4 hours which has been mounted and polished to obtain a cross-sectional view though the particle. The micrograph shows intergranular cracking, indicating that the mode of fracture at this interval is the same as that observed during pulverisation of the splats, namely intergranular fracture.

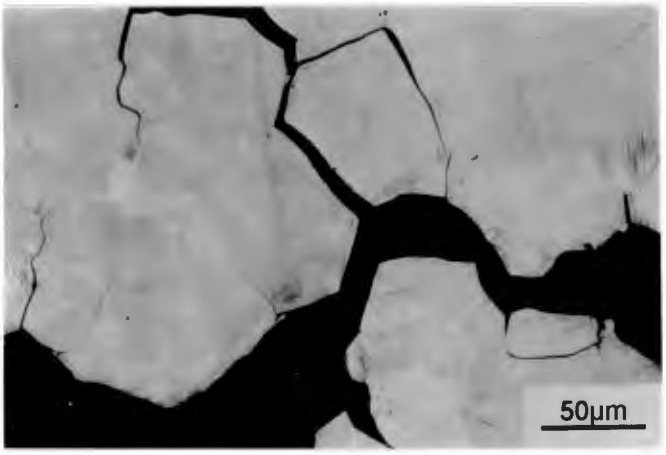

Figure 4.22: Optical micrograph of a polished section of a melt quenched particle after 4 hours of milling showing intergranular cracking.

4.3 Phase Changes and Microstructural Changes During Milling

X-ray diffraction (XRD) has been performed on the samples drawn during milling in order to determine the phase changes during milling. The XRD traces of the material heat treated to produce an α phase, β phase and γ phase microstructure are presented in Appendix B. All the traces have only one peak except for the milled and annealed elemental powder blend scan which has two α phase peaks and one δ phase peak. No martensite was detected in the sample quenched from the β phase, indicating that the bulk material had a tin composition between 24.1wt% and 25.6wt% [27, 30].

The *d*-spacings for the phases were calculated using Equation 3 on page 33 by making d_{hkl} the subject of the formula. This was done to aid phase identification during subsequent analysis. The peaks for the individual phases along with the *d*-spacings of the phases are presented in Table 4.2.

Table 4.2: Table of phases and determined diffraction peak positions, with *d*-spacings.

Phase	2θ(°)	*d* (Å)
α	42.4	2.13
α	49.3	1.85
δ	42.7	2.12
β	39.3	2.29
γ	42.9	2.11

4.3.1 Elemental Powder Blend

Figure 4.23 is an XRD trace of the initial elemental powder blend. The XRD trace shows that the powder consists of a mix of elemental copper and tin, as expected.

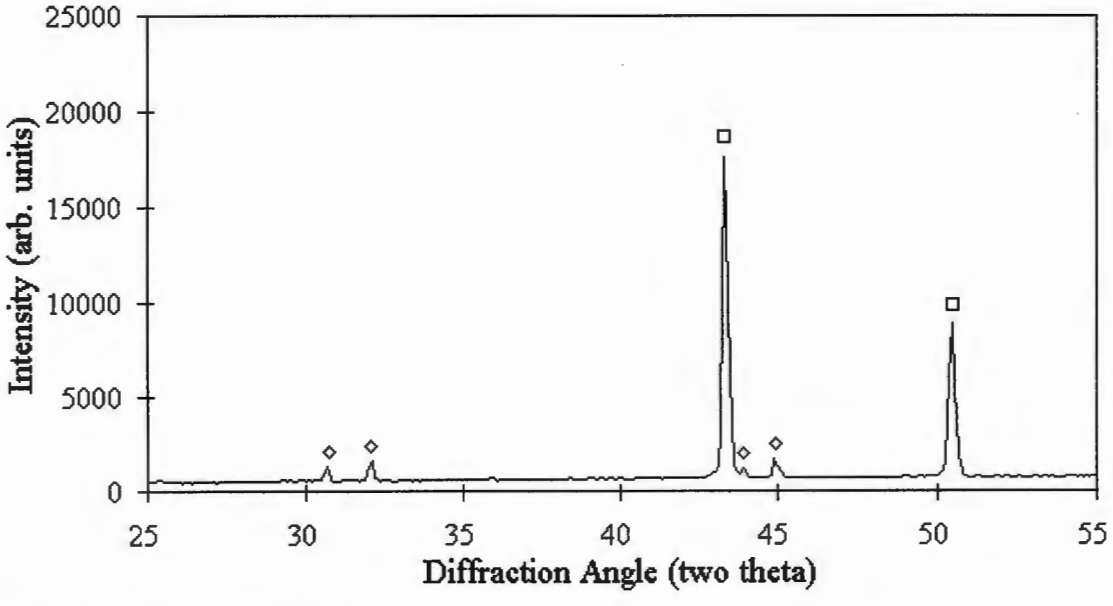

Figure 4.23: XRD trace of initial elemental powder blend charge.
Labels: □ Cu, ◇ Sn.

After milling for 4 hours the main peaks have decreased in intensity (indicated by the lower scale of the y-axis) and have begun to broaden, as seen in Figure 4.24. The primary copper diffraction peak at $2\theta = 43.3$ ° has developed a distinct shoulder in the

range 42.4 ° to 42.9 °, indicating the formation of the δ phase. The main diffraction peak of this phase is between 42.60 ° and 42.72 ° (Appendix A, Table A7 to Table A10). A surprising occurrence is the formation of the tin-rich η phase at this sampling interval. This phase is normally stable only at higher tin compositions as shown in the binary phase diagram in Figure 2.4 on page 8.

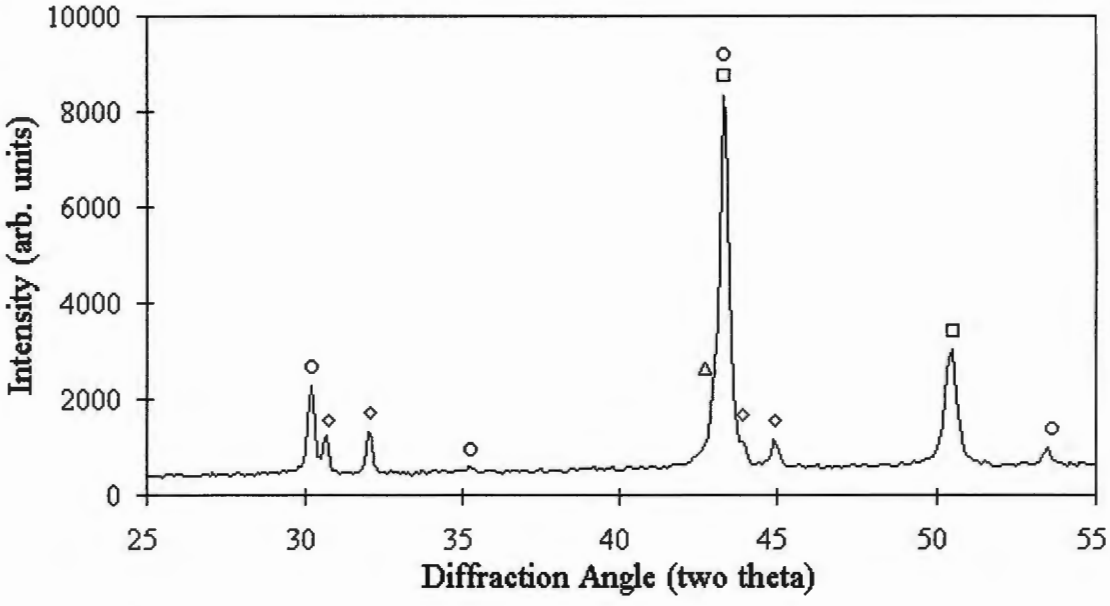

Figure 4.24: XRD trace of elemental powder blend milled for 4 hours.
Labels: □ Cu, ◇ Sn, ○ η phase, △ δ phase.

After milling for 8 hours the XRD peaks have further decreased in intensity and have broadened further as can be seen from Figure 4.25. The tin peaks have disappeared, indicating solid solution formation. Accompanying the disappearance of the tin peaks is the formation of the α phase on the shoulder of the primary copper peak at $2\theta = 42.4$ °.

Figure 4.26 shows that after milling for 24 hours the intensity of the diffraction peaks has decreased and broadened further, and the primary phase present is the δ phase. The contribution of the α phase intensity to the XRD trace is approximately equal to that of the copper, and the η phase has almost totally dissolved.

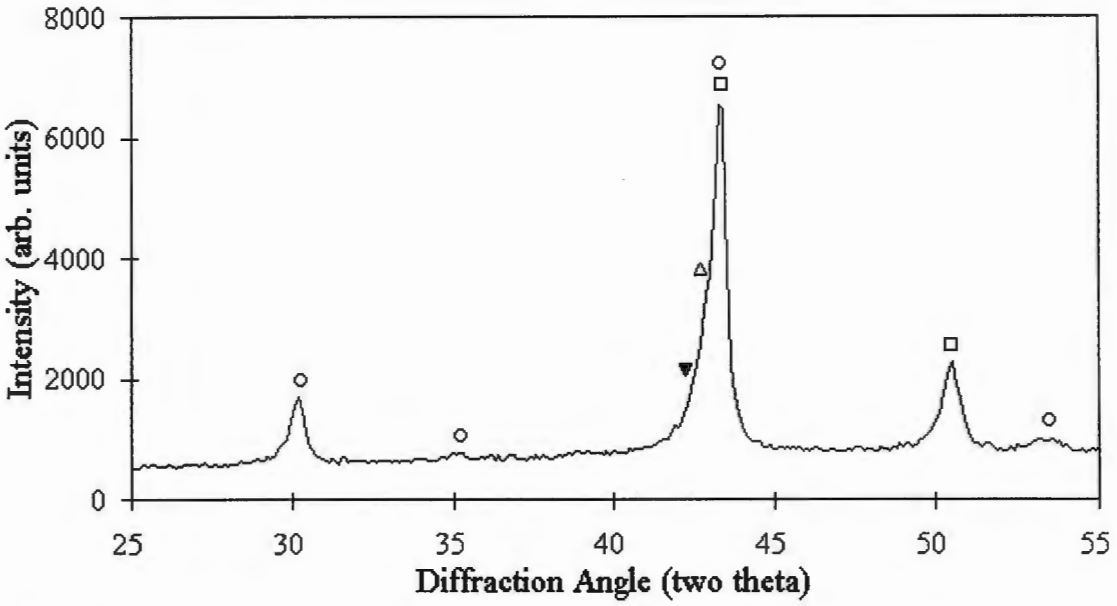

Figure 4.25: XRD trace of elemental powder blend milled for 8 hours.

Labels: □ Cu, ○ η phase, △ δ phase, ▼ α phase.

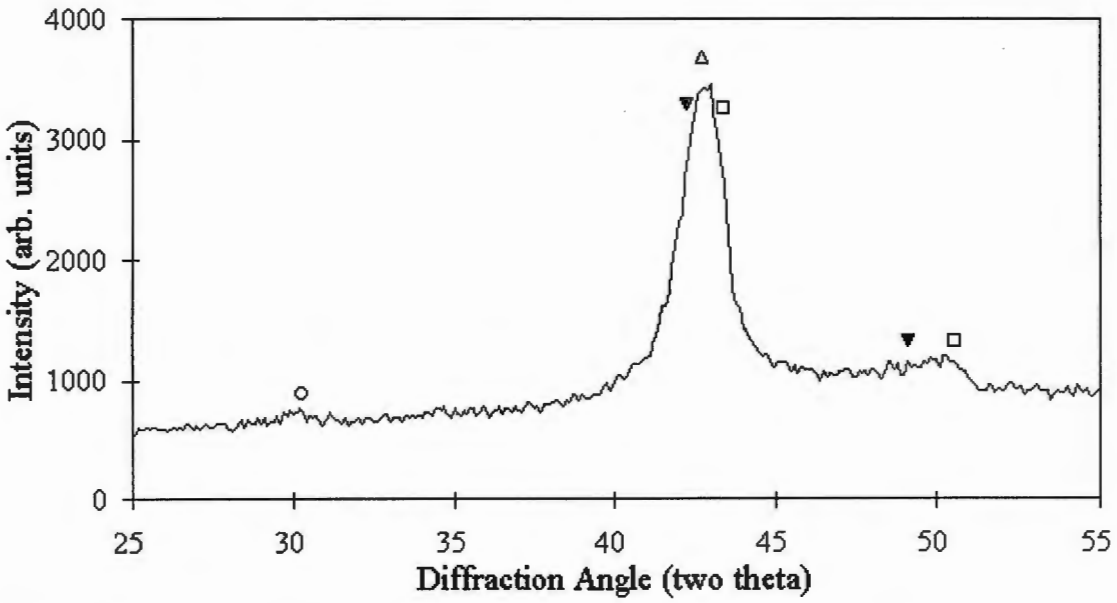

Figure 4.26: XRD trace of elemental powder blend milled for 24 hours.

Labels: □ Cu, ○ η phase, △ δ phase, ▼ α phase.

At the final stage of milling, Figure 4.27 shows that the XRD trace is comprised of two broad overlapping peaks corresponding to the α phase and δ phase, and a broad low-intensity peak. The latter peak, which is visible between approximately 37.5 ° and 41.0 ° (above which it is obscured by the remainder of the trace) is thought to

correspond to the amorphous phase. This is understood by making use of Figure 4.28 which shows separate XRD data for crystalline and amorphous versions of the Pd_3Si composition [2]. A simplistic analysis of Figure 4.27 based on the separate XRD traces shown in Figure 4.28 is shown in Figure 4.29. It shows how the XRD trace may have been made up of separate but additive contributions from the amorphous phase and the broadened peaks of the crystalline α phase and δ phase. The amorphous phase is also visible to a lesser extent in the elemental powder milled for 24 hours.

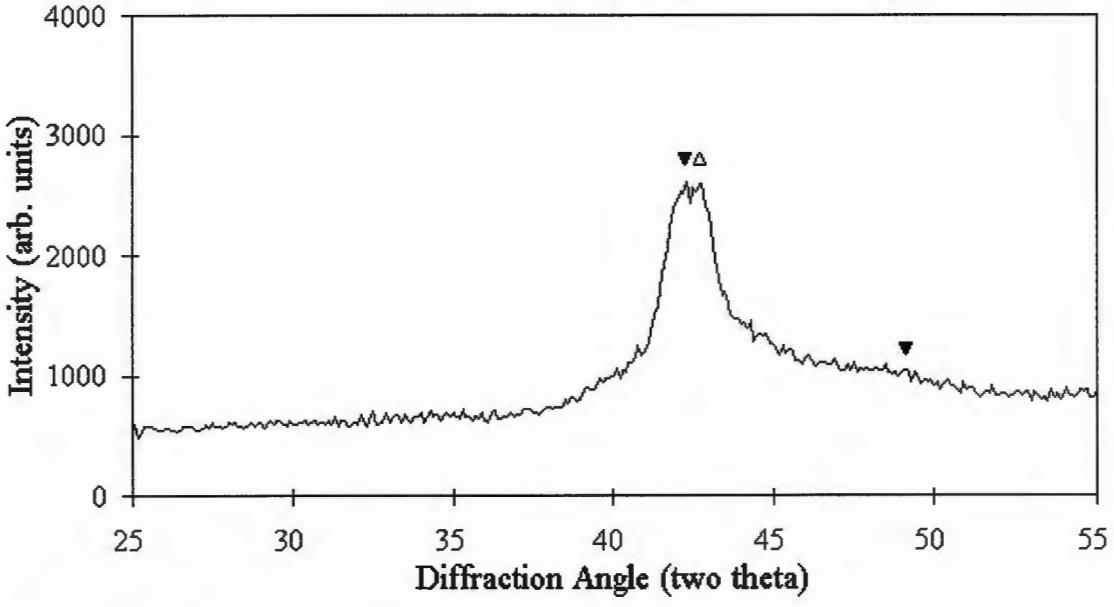

Figure 4.27: XRD trace of elemental powder blend milled for 48 hours.
Labels: △ δ phase, ▼ α phase.

A second possibility for the broad, low-intensity peak is that of strain. During HEM, the powder particles become highly deformed as a result of continuous collisions [1, 34, 38]. This produces a powder which is highly strained. It is thought that strain is only a minor component of the observed peak broadening and not the major component.

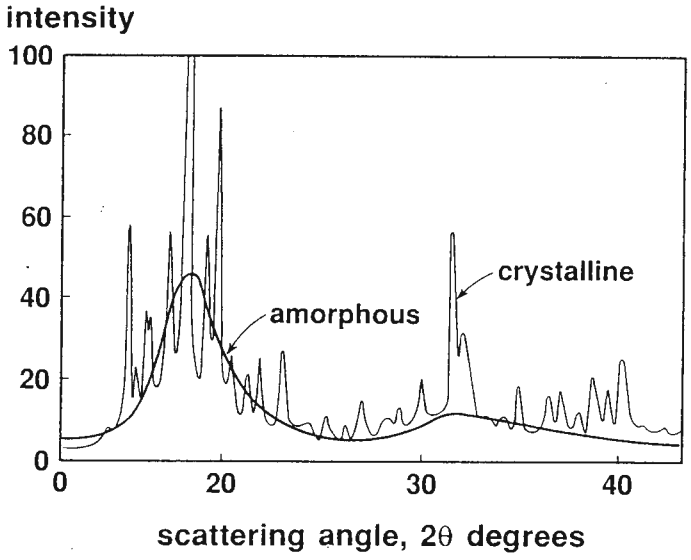

Figure 4.28: Diagram comparing XRD traces of crystalline and amorphous versions of the Pd_3Si composition (reproduced from [2]).

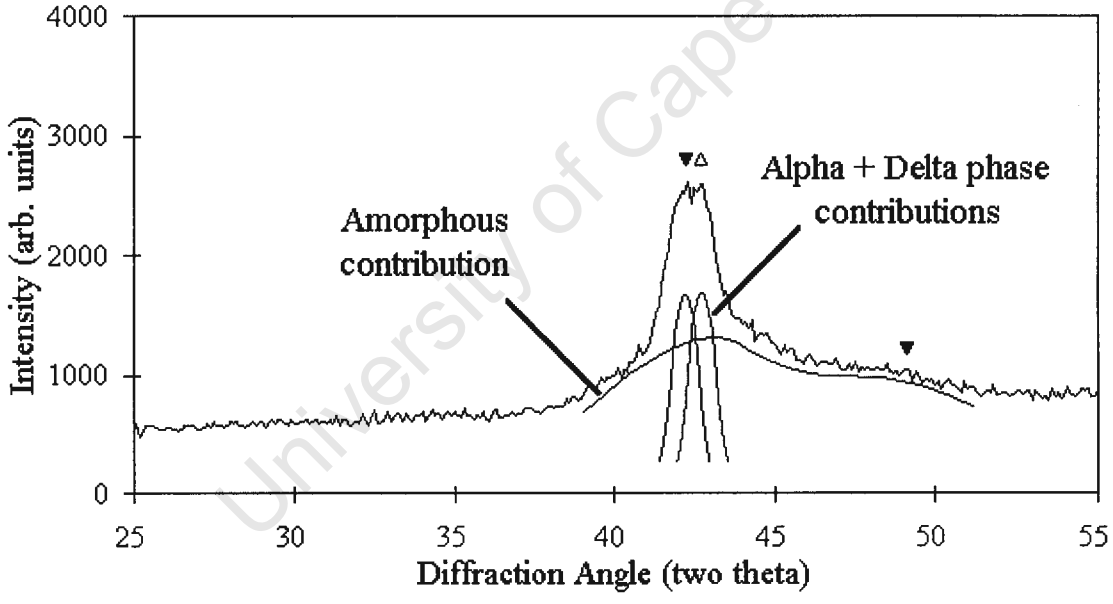

Figure 4.29: XRD trace after milling for 48 h showing amorphous contribution and α phase plus δ phase contributions. Labels: ▵ δ phase, ▼ α phase.

A summary of the sequence of phase formation during mechanical alloying of the elemental powder blend based on analysis of the XRD traces is shown in Table 4.3.

Table 4.3: Table showing the sequence of phase formation during mechanical alloying of the elemental powder blend.

Milling Time (hours)	Phases Present					
	Sn	Cu	η	δ	α	amorph.
0	×	×				
4	×	×	×	×		
8		×	×	×	×	
24		×	×	×	×	×
48				×	×	×

Figure 4.30 is a bright field transmission electron micrograph of a portion of a particle from the elemental blend powder which had been milled for 48 hours in the attrition mill, with corresponding electron diffraction pattern (EDP). The structure consists of contrast regions which are fairly equiaxed in appearance with an observed size range of approximately 5 nm to 40 nm. The EDP is comprised of concentric circles.

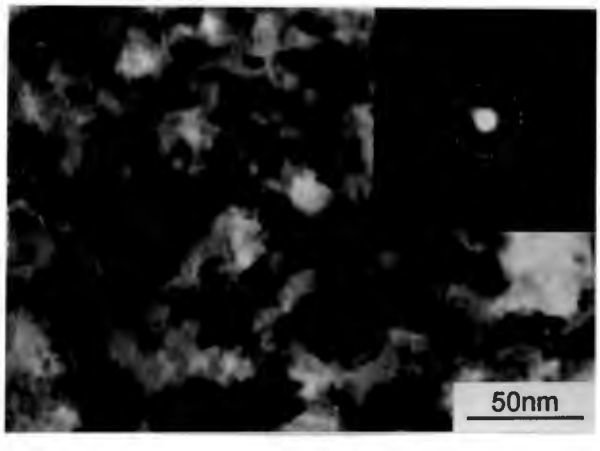

Figure 4.30: Bright field TEM micrograph of an elemental blend powder particle milled for 48 hours with corresponding EDP.

The presence of an EDP which consists of concentric circles can be understood by examining Figure 4.31. The aperture utilised to produce an EDP from a certain area is

of a standard size. A single crystal will produce a single spot pattern if electron diffraction occurs, whereas if the aperture is positioned over an area which includes more than one diffracting grain, a triple junction for example, the diffraction pattern produced will consist of a number of individual EDPs depending on the orientation of the crystals to one another [63].

If there are a number of crystals in the area selected with a grain size smaller than the aperture size which will cause electron diffraction to occur, but which differ in orientation to the beam direction and each other, then the resulting EDP will consist of numerous individual EDPs each differing in orientation to each other [63]. These individual EDPs overlap to produce an EDP with concentric rings.

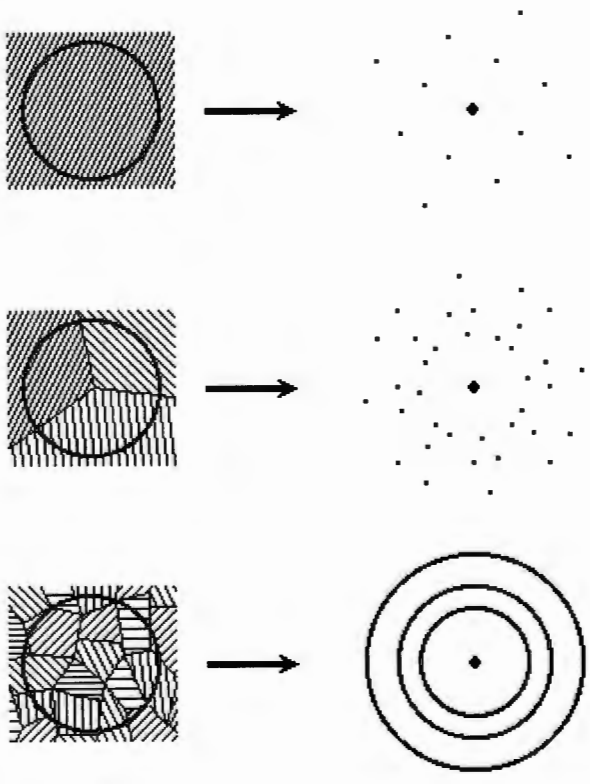

Figure 4.31: Schematic diagram showing the microstructure and resulting EDP of crystalline samples of various grain sizes using a standard aperture (circle). (Redrawn from [63].)

An EDP with concentric circles may also be caused by the presence of oxides in the sample under examination. Oxidation of the powders may have taken place during

storage in air between completion of milling and TEM examination, therefore this factor is to be taken into consideration when analysing the EDPs.

4.3.2 Cast Powder

Figure 4.32 is an optical micrograph of the cast structure prior to pulverisation of the material to a powder. The micrograph shows α phase grains with α phase plus δ phase bainite which has formed at the boundaries, and some δ phase precipitates inside the previous β phase grains.

The initial cast powder was analysed using XRD and the resulting XRD trace is presented in Figure 4.33. XRD indicates that the initial powder consists of the δ phase with a small amount of tin which may have segregated to the grain boundaries during solidification from the melt. The normalised intensity I_n of the main diffraction peak (the ratio of the peak intensity I_p to the background intensity I_0) is 12.9.

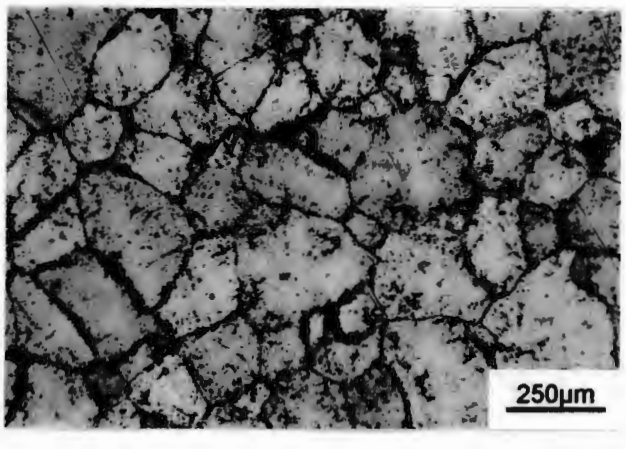

Figure 4.32: Optical micrograph showing the microstructure of the cast CuSn which consists of α phase grains and α phase plus δ phase bainite at the grain boundaries, with intragranular δ phase precipitates.

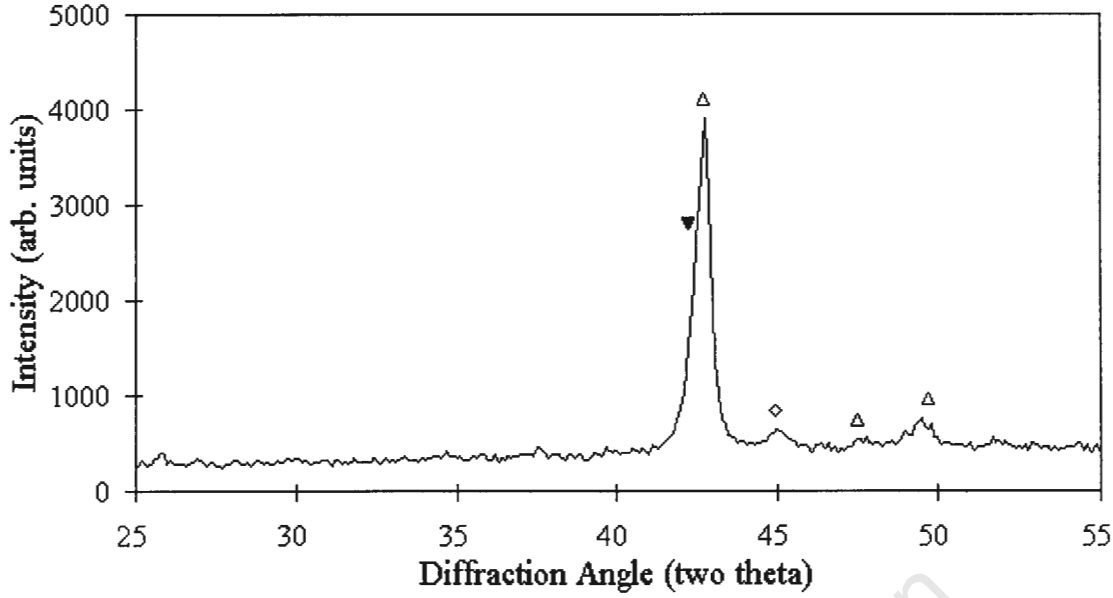

Figure 4.33: XRD trace of initial cast powder charge.
Labels: △ δ phase, ▼ α phase, ◇ Sn.

The discrepancy between phase detection using optical examination (which reveals that the material consists of the α phase and δ phase) and XRD (which reveals only the δ phase) can be explained due to the proximity of the diffraction peaks of the two phases. The δ phase peak is located at 42.7 ° and the α phase peak at 42.4 °. A stronger δ phase peak may also mask a weaker α phase peak. This is the reason for the insertion of the α phase marker on the XRD traces for the milled cast powder.

The main peak broadens as milling progresses and the normalised intensity I_n decreases from an initial value of 12.9 to 8.7 after milling for 8 hours (Figure 4.34). The tin peak disappears after milling for 8 hours, indicating that the tin has gone into solution.

After milling for 48 hours the position of the combined α phase plus δ phase peak has shifted from its initial position of 42.8 ° to 42.5 ° (Figure 4.35). The main peak has broadened further during milling, and the normalised intensity I_n has decreased further from 8.7 after milling for 8 hours to 5.1 after milling for 48 hours, indicating that the intensity of the diffraction peaks have decreased due to milling. The amorphous plus crystalline structure found after complete milling of the elemental powder blend

(section 4.3.1) is found in the cast powder milled for 48 hours. Evidence of this is the broad, low-intensity peak underlying the combined α phase plus δ phase peak in Figure 4.35, similar to that shown in Figure 4.29 on page 59.

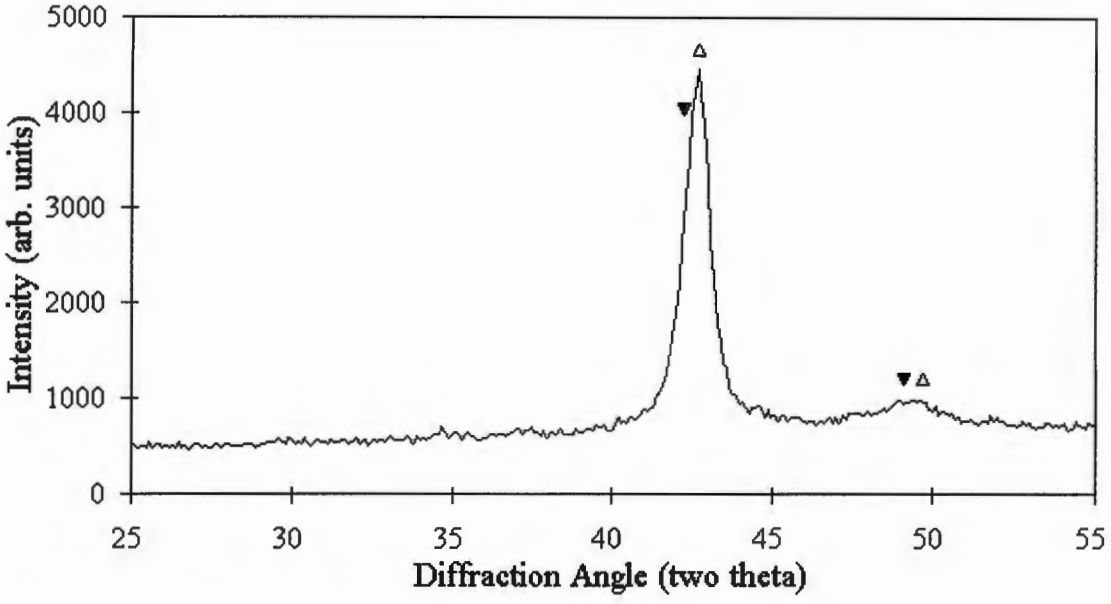

Figure 4.34: XRD trace of cast powder milled for 8 hours.

Labels: ▵ δ phase, ▼ α phase.

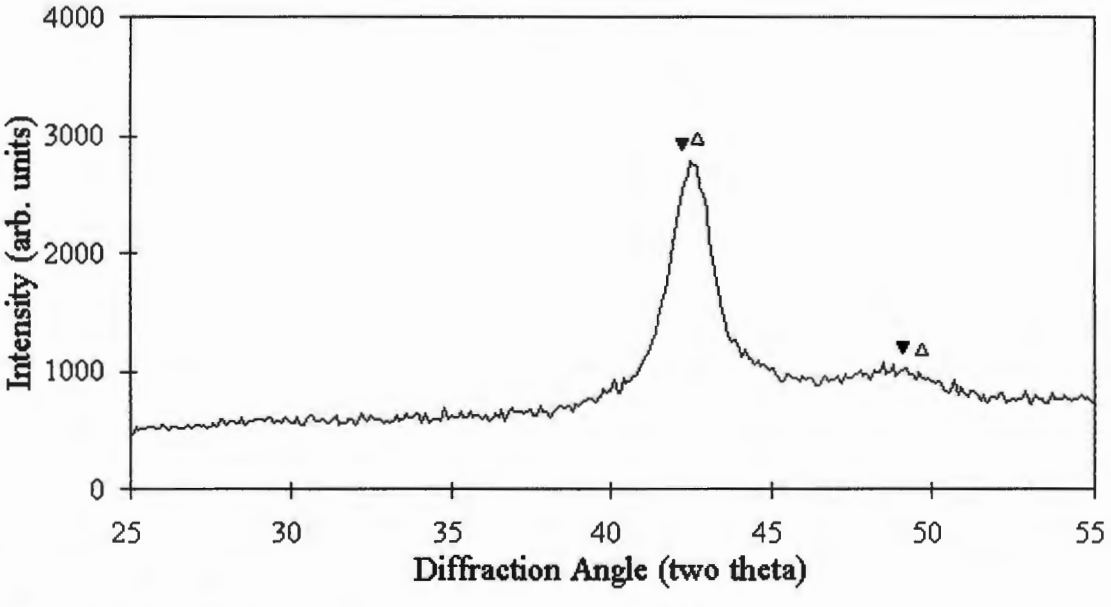

Figure 4.35: XRD trace of cast powder milled for 48 hours.

Labels: ▵ δ phase, ▼ α phase.

Figure 4.36 (a) is a bright field TEM micrograph of a cast powder particle milled for 48 hours with corresponding EDP. The structure consists of polygonal regions with well defined boundaries and an EDP with concentric circles. The size of these polygonal regions ranged from approximately 10 nm to 50 nm. Figure 4.36 (b) is a close-up of a group of polygonal regions in the same particle.

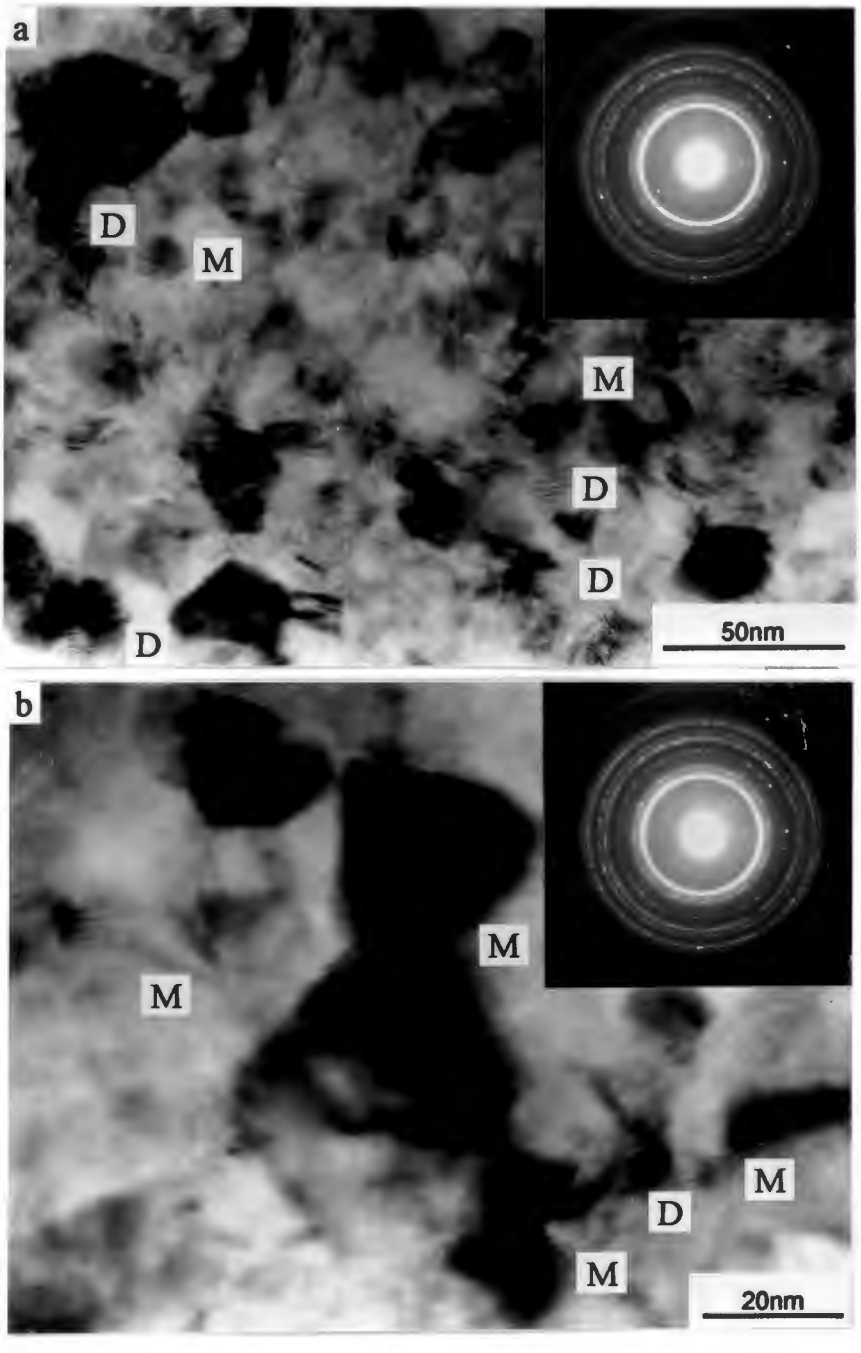

Figure 4.36: Bright field TEM micrographs of a cast powder particle milled for 48 hours with corresponding EDPs. 'M' indicates a Moiré pattern and 'D' a Moiré pattern containing a screw dislocation.

The fringes seen in Figure 4.36 are Moiré patterns [25, 63, 64]. Moiré patterns are produced when two thin crystals overlap. Figure 4.37 demonstrates the formation of Moiré patterns using overlapping line gratings to represent the crystal lattices. Parallel Moiré patterns are generated when two lattices with interplanar lattice spacings which differ slightly lie parallel to each other, while rotation Moiré patterns are generated when two lattices with the same interplanar spacing are rotated against one another by a small angle [61, 64], shown in Figure 4.37 (a) and Figure 4.37 (b).

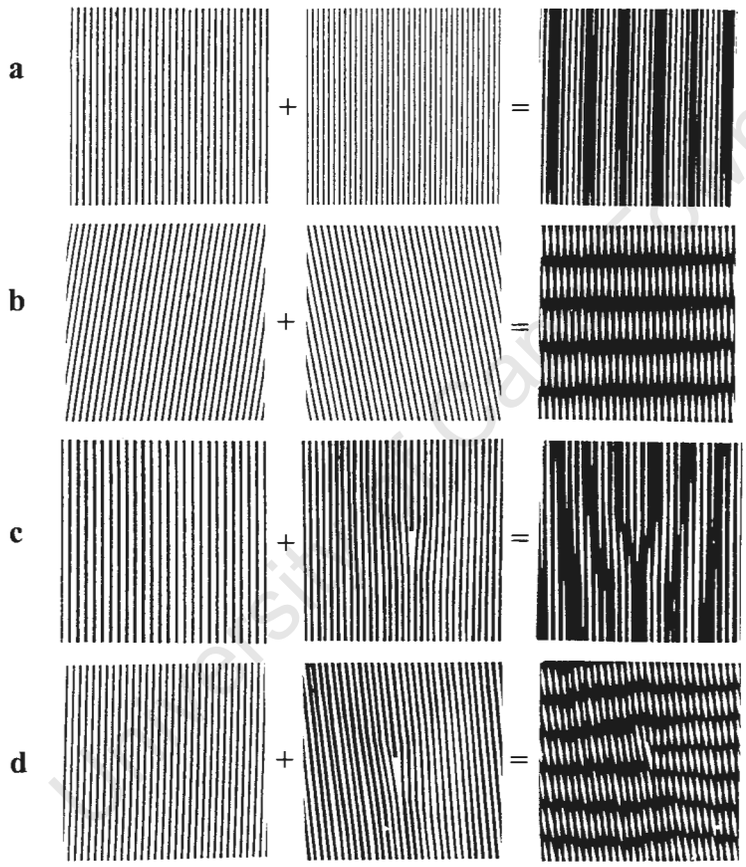

Figure 4.37: Diagrams using overlapping line gratings to demonstrate the formation of (a) & (c) parallel Moiré patterns and (b) & (d) rotation Moiré patterns, where one of the gratings contains a dislocation in (c) & (d). (Reproduced from [61].)

The image produced is a structure with double periodicity consisting of beats which can be sufficiently large to be resolved in the transmission electron microscope, even though the individual lattice spacings are below the resolution limit [61]. Mixed

Moiré patterns can also be formed, due to overlapping gratings with different spacings and a small relative twist. An edge dislocation introduced into one of the superimposed lattices is also imaged in the Moiré pattern, shown in Figure 4.37 (c) and Figure 4.37 (d). Moiré patterns of these and the former type are shown in Figure 4.36. Moiré patterns were also observed in the elemental blend powder which had been mechanically alloyed.

The presence of Moiré patterns in the TEM micrographs reveals that the contrasted regions in the powder have a crystalline structure. This confirms the deduction that the EDPs obtained during TEM examination of the milled powders (Figure 4.28 on page 59 and Figure 4.36) consists of concentric circles as a result of numerous diffracting crystals being present in the area selected by the diffraction aperture. Moiré patterns revealing the presence of dislocations indicates that the material has been deformed during milling, as expected, as high deformation occurs during high energy milling [1, 51, 57].

The diffuse ring in the EDP in Figure 4.36 may be an indication that the material is amorphous due to a variation in the lattice parameter of the material, or that there is a strongly preferred orientation of some of the diffracting nanocrystals [25]. Preferred orientation of the nanocrystals would have resulted in clustering of the diffraction spots in some of the other diffraction rings due to the periodicity of the diffraction patterns. Therefore the diffuse ring in the EDP is thought to be an indication that the powder particle is partially amorphous.

4.3.3 Melt Quenched Powder

Figure 4.38 is an optical micrograph of the structure of the melt quenched splats prior to pulverisation, showing β′ phase needles within β phase grains. This indicates that the material has a tin content between 20.0wt% and 24.1wt% [21]. A small percentage of tin may have been lost to oxidation during preparation of the alloy from bulk elemental stock, as reported in [31]. Coarse α phase precipitates and fine δ phase

precipitates with a size of 4.8 μm and 0.6 μm respectively have formed within the β phase grains during melt quenching.

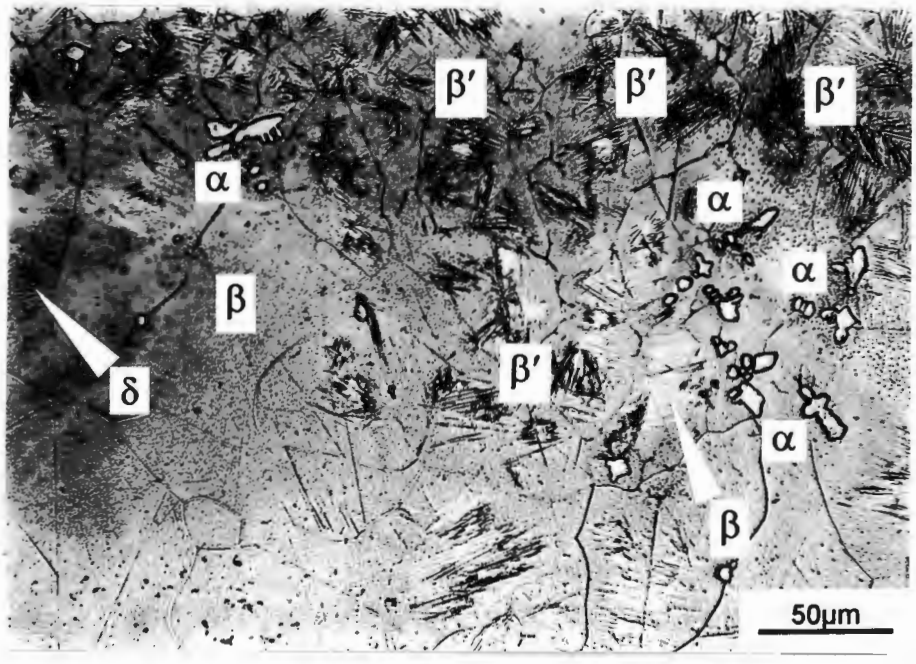

Figure 4.38: Optical micrograph showing the microstructure of melt quenched CuSn, consisting of coarse α phase and fine δ phase precipitates, and β′ phase needles within a β phase matrix.

Bands of martensite form in the matrix during microhardness testing, confirming that the matrix is in fact the β phase [29]. The microhardness of the matrix is 155 HV, which is close to the experimentally determined microhardness of 128 HV for the β phase (Table 4.1 on page 43), and indicates that the fine δ phase precipitates have strengthened the matrix by precipitation hardening [14].

Figure 4.39 is an XRD trace of the initial pulverised melt quenched powder. XRD indicates that the initial powder consists of the δ phase, β phase and α phase, as observed during optical examination of the melt quenched splats, as well as the ε phase and Cu_4O_3. The copper oxide detected has formed during melt quenching of the material. It is a coherent oxide which does not flake off the splats, and is visible as a tarnishing on the surface of the splats. The ε phase which was detected by XRD was not observed during optical examination and was not expected to precipitate due

to the difficulty of formation [24, 26]. The normalised intensity I_n of the main δ phase peak is 9.3.

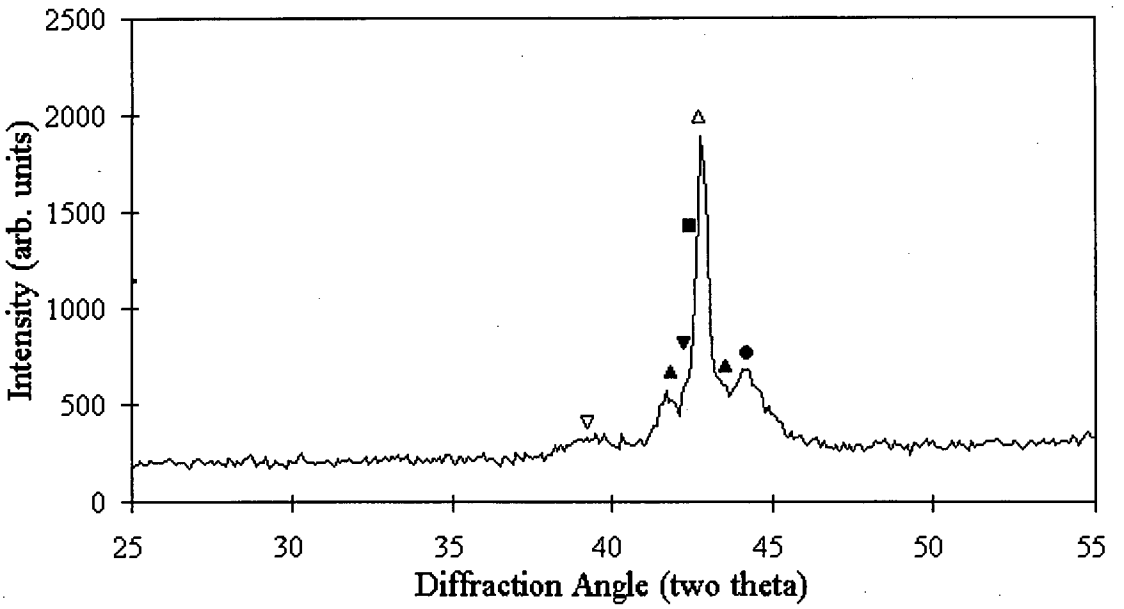

Figure 4.39: XRD trace of initial melt quenched powder charge.

Labels: ▵ δ phase, ▼ α phase, ▽ β phase, ■ β′ phase, ▲ ε phase, ● Cu_4O_3.

Figure 3.40 shows the XRD trace of the melt quenched powder after milling for 4 hours. The ε phase peak at 41.8 ° is more visible in the trace, but otherwise there is no other noticeable change in the trace apart from broadening of the diffraction peaks.

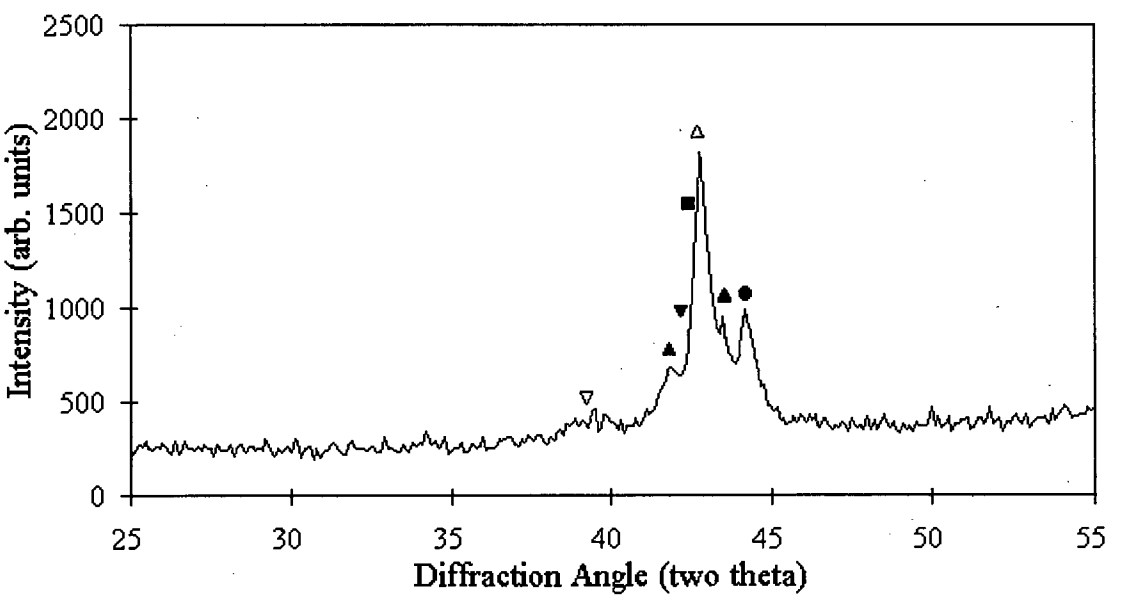

Figure 4.40: XRD trace of melt quenched powder milled for 4 hours.

Labels: ▵ δ phase, ▼ α phase, ▽ β phase, ■ β′ phase, ▲ ε phase, ● Cu_4O_3.

The normalised intensity I_n of the main δ phase peak has decreased from 9.3 for the initial powder to 4.9 for the powder milled for 8 hours, while that of the ε phase and the Cu_4O_3 peak has remained constant (Figure 4.41).

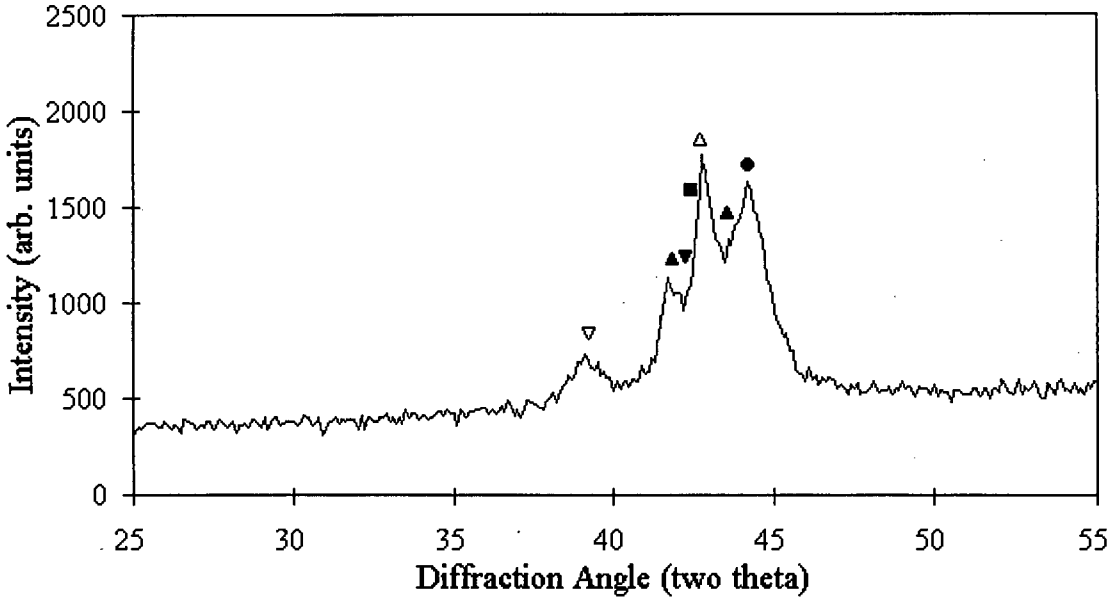

Figure 4.41: XRD trace of melt quenched powder milled for 8 hours.
Labels: △ δ phase, ▼ α phase, ▽ β phase, ■ β′ phase, ▲ ε phase, ● Cu_4O_3.

After milling for 24 hours, Figure 4.42 shows that the peaks have broadened to such an extent that it is impossible to distinguish between the individual diffraction peaks. The intensities of the α phase, β′ phase and ε phase peaks have increased relative to the intensities of the other phases. The intensity of the α phase peak is equal to that of the δ phase peak, indicating that the α phase is forming in increasing amounts during milling as the δ phase undergoes dissolution.

This process of dissolution of the δ phase and formation of the α phase during milling is repeated in the XRD trace of the powder sample drawn after completion of milling. Figure 4.43 shows that the intensity of the α phase is greater than the intensity of the δ phase. It also shows the same effect encountered after milling of the elemental powder blend and cast powder for 48 hours, namely an extremely broad, low-intensity peak underlying the crystalline peaks seen in Figure 4.29 on page 59. This indicates

that the powder is composed not only of crystalline phases, but also of an amorphous component.

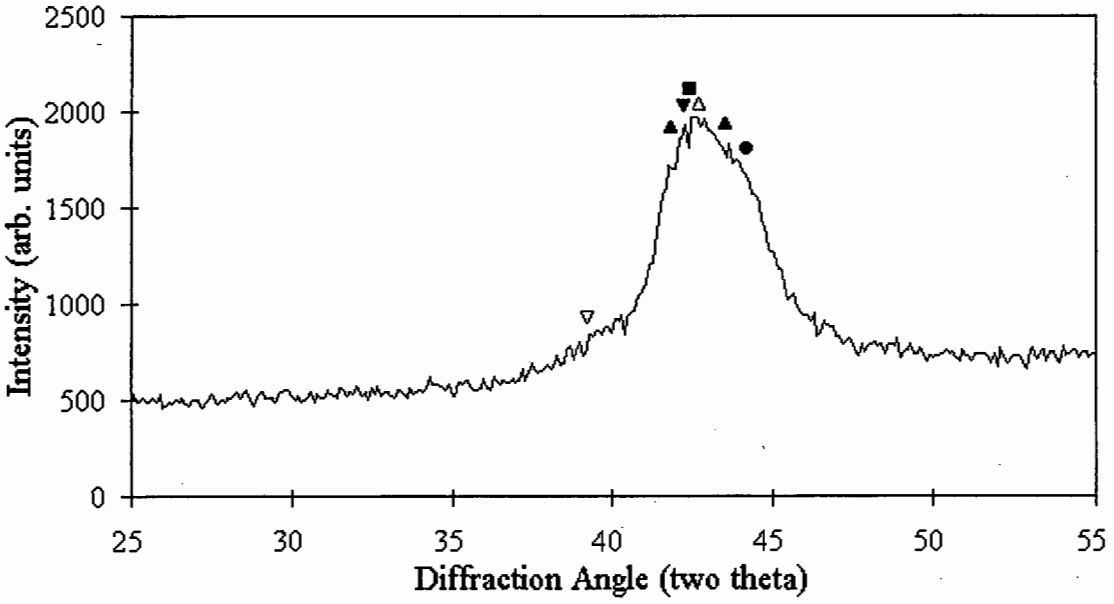

Figure 4.42: XRD trace of melt quenched powder milled for 24 hours.

Labels: △ δ phase, ▼ α phase, ▽ β phase, ■ β′ phase, ▲ ε phase, ● Cu_4O_3.

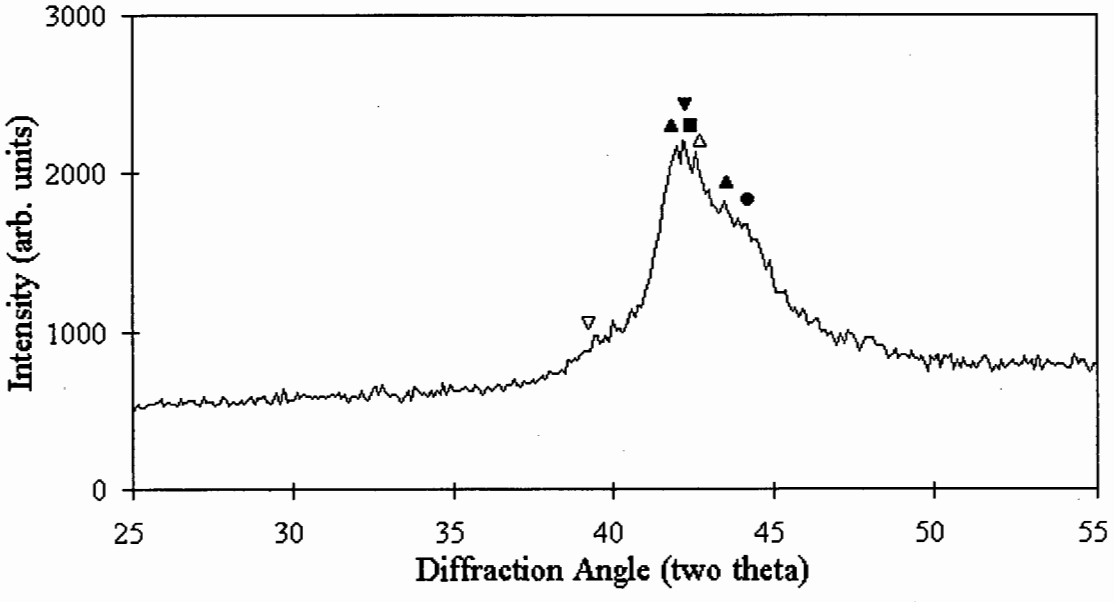

Figure 4.43: XRD trace of melt quenched powder milled for 48 hours.

Labels: △ δ phase, ▼ α phase, ▽ β phase, ■ β′ phase, ▲ ε phase, ● Cu_4O_3.

Figure 4.44 is a bright field TEM micrograph of a melt quenched powder particle milled for 48 hours in the attrition mill, with corresponding EDP. As observed in the microstructure of the elemental blend and the cast powder which had been milled for 48 hours, the structure of the particle consists of equiaxed regions, and has an EDP comprised of concentric circles. The size of these equiaxed regions ranged from approximately 5 nm to 40 nm. Moiré fringes were also seen in the TEM micrographs, indicating that these regions are crystalline.

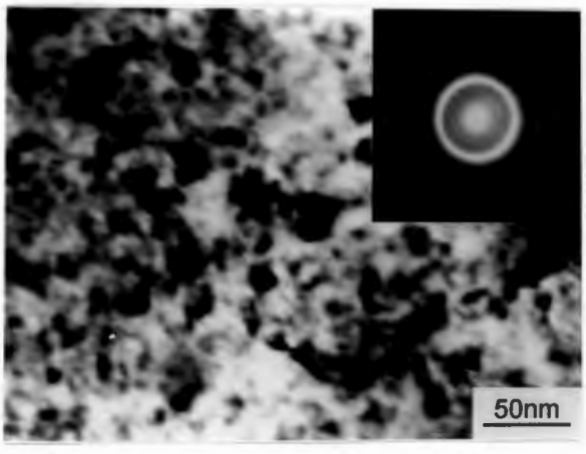

Figure 4.44: Bright field TEM micrograph of a melt quenched powder particle milled for 48 hours with corresponding EDP.

4.4 Annealing of Milled Powders

The powders which had been milled for 48 hours in the attrition mill were annealed at 450 °C for 1 hour. Figure 4.45 compares the XRD trace of the milled elemental powder blend to that of the annealed powder.

The annealed powder consists of the equilibrium structure encountered at 450 °C for CuSn, namely the α phase plus the δ phase. No oxide formation was detected. The peaks have narrowed considerably indicating that crystalline grain growth and strain release has taken place [5]. There is no evidence of the amorphous phase after annealing. The intensity of the δ phase is greater than that of the α phase, indicating that dissolution of a portion the α phase has led to complementary formation of the δ phase.

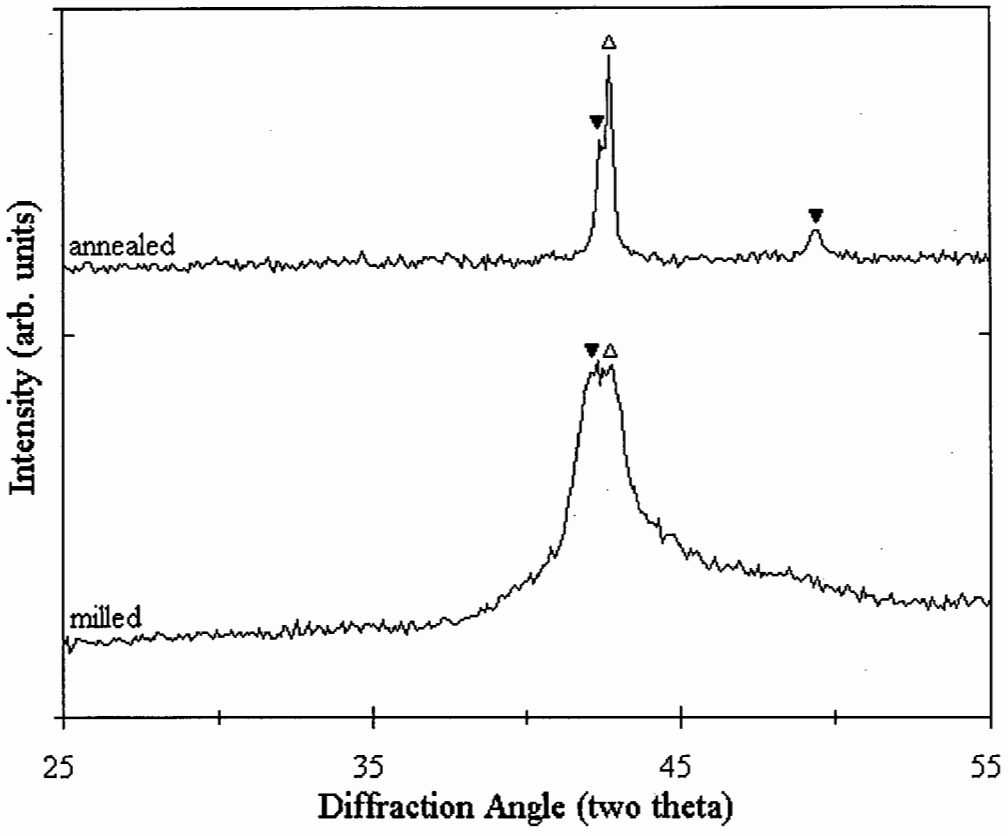

Figure 4.45: Plot showing XRD traces of the elemental powder blend after milling for 48 hours and after the milled powder had been annealed at 450 °C for 1 hour.
Labels: ▵ δ phase, ▼ α phase.

After MA of the elemental powder blend the α phase peaks have moved to a lower diffraction angle compared with pure copper powder indicating an increase in the *d*-spacing and therefore in the lattice parameter of the α phase (in Figure 4.23 to Figure 4.27 on pages 55-58). Annealing of the milled powder at 450 °C causes a slight shift in the diffraction peak position to a higher diffraction angle, indicating a slight decrease in the *d*-spacing and therefore in the lattice parameter. The α phase is face-centred cubic (fcc) [23], and the lattice parameter *a* of the α phase can be calculated using the following formula for materials with an fcc crystal structure [65]:

$$a = d_{hkl}\sqrt{h^2 + k^2 + l^2} \qquad \text{...Equation 4}$$

Using the primary α phase diffraction peak position, i.e. $hkl = 1\ 1\ 1$, and Equation 3 on page 33 to calculate d_{hkl} by making d_{hkl} the subject of the formula, the lattice parameter a of the α phase has been calculated for elemental copper, the elemental powder blend milled for 48 hours and the milled elemental powder blend annealed at 450 °C for 1 hour, and is listed in Table 4.4

Table 4.4: Table comparing diffraction angle, interplanar spacing and lattice parameter of the (1 1 1) reflection of the α phase of elemental copper, the milled elemental powder blend, and the milled and annealed powder.

	Elemental copper	Milled 48 hours	Annealed 1 hour
2θ(°)	43.3	42.1	42.4
d_{111} (Å)	2.09	2.15	2.13
a (Å)	3.62	3.72	3.69

Table 4.4 shows that the lattice parameter a of the α phase increases from an initial value of 3.62 Å for elemental copper to 3.72 Å for the α phase in the milled elemental powder blend due to formation of a solid solution. The lattice parameter decreases to 3.69 Å after annealing of the milled powder.

The diffraction peaks of the milled cast powder and melt quenched powder are close together and could not be separately identified. Therefore a detailed analysis of the change in lattice parameter during milling of these powders, as was performed on the milled elemental powder blend, could not be performed.

XRD revealed that annealing of the milled cast powder and milled melt quenched powder at 450 °C for 1 hour produced the same results after annealing of the milled elemental powder blend. Annealing of these powders led to the formation of the equilibrium structure, namely the α phase plus the δ phase. The diffraction peaks had narrowed considerably and were located at the same positions as those for the milled and annealed elemental powder blend. Therefore, graphs comparing the XRD traces

of the milled cast powder and milled melt quenched powder to those of the respective annealed powders have been omitted from the results section and have been placed in Appendix C.

4.5 Analysis of Electron Diffraction Patterns

The EDPs of the milled powders have been analysed in order to verify the phases present in the samples. The radii *r* of the diffraction rings in the EDPs have been converted into an interplanar spacing distance *d* using Equation 1 on page 31 and have been compared to the standard tables of *d*-spacings (Appendix A) for the various phases which are expected to be present, and to the experimentally determined *d*-spacings (Table 4.2 on page 55 and Table 4.4 on page 72).

Table 4.5 shows the measured radii *r* of the rings in the EDP of the milled elemental powder blend (insert in Figure 4.28 on page 59) with calculated *d*-values and possible phases present. As no ε phase was detected in the milled elemental powder blend, the second ring is caused by diffraction from the δ phase and SnO_2. This confirms that the δ phase is formed during milling of the elemental powder blend.

Table 4.5: Table of possible phases and oxides present in the milled elemental powder blend.

Ring no.	*r* (Å)	*d* (Å)	Possible phases
1	7.6	2.7	SnO*
2	8.6	2.4	δ*, ε*, SnO_2*
3	12.3	1.67	SnO_2*

* Denotes strong diffraction.

As no oxides were detected by XRD of the elemental powder blend during milling, the tin oxides detected could have formed due to storage of the milled elemental powder blend in air.

Table 4.6 shows the measured radii *r* of the rings in the EDP of the milled cast powder (inserts in Figure 4.36 on page 65) with calculated *d*-values and possible phases present. The strong ring could be due a number of phases as indicated. Conclusive identification of the diffracting phase is difficult due to the experimental inaccuracy. Diffraction is most likely due to either the α phase, the δ phase or the amorphous phase as these were the only phases detected by XRD during milling of the cast powder. The oxides detected could have formed during storage of the milled powder in air as no oxides were detected by XRD during milling of the cast powder.

Table 4.6: Table of possible phases and oxides present in the milled cast powder.

Ring no.	*r* (Å)	*d* (Å)	Possible phases
1	7.1	2.9	Cu_4O_3*
2	8.3	2.5	Cu_4O_3*, CuO*, Cu_2O*
3*	9.9	2.1	α*, δ*, β′*, γ*, ε*, η*, Cu_2O, SnO_2, amorphous
4	10.9	1.88	Cu_4O_3*
5	11.2	1.83	δ
6	14.0	1.46	δ, Cu_4O_3
7	16.1	1.27	δ, η
8	17.1	1.20	η, CuO, SnO
9	18.9	1.08	ε, β″*, CuO, SnO, SnO_2
10	19.6	1.05	η

* Denotes strong diffraction.

Table 4.7 shows the measured radii *r* of the rings in the EDP of the milled melt quenched powder (insert in Figure 4.44 on page 72) with calculated *d*-values and possible phases present. The strong, wide band (ring no. 1) could be due to the addition of a number of phases as indicated, but is most likely due to the amorphous phase and the α phase as the β″ phase, γ phase and η phase were not detected by XRD during milling of the melt quenched powder.

Table 4.7: Table of possible phases and oxides present in the milled melt quenched powder.

Ring no.	r (Å)	d (Å)	Possible phases
1*	9.3 - 10.3	2.2 - 1.99	α*, δ*, β'*, β''*, γ*, ε*, η*, Cu_4O_3*, Cu_2O*, SnO, SnO_2, amorphous
2	13.6	1.51	Cu_2O*
3	14.6	1.41	CuO*
4	16.8	1.22	δ*, β'*, β''*, SnO*, SnO_2
5	18.4	1.11	δ*, β'*

* Denotes strong diffraction.

Cu_4O_3 was present prior to milling due to preparation of the melt in air and melt quenching into water. The other oxides detected could have formed during storage of the milled melt quenched powder in air as no other oxides besides Cu_4O_3 were detected by XRD during milling of the powder.

4.6 Thermo-Mechanical Processing of Milled Powders

The milled powders were processed using a number of techniques, namely sintering, hot isostatic pressing (HIP) and hot uniaxial pressing (HUP). The results are as follows:

4.6.1 Pressureless Sintering

Figure 4.46 shows a plot of the microhardness of the milled cast powder which had been sintered for 1 hour at the temperatures indicated compared with the hardness of the green compact. The average green microhardness is 108 HV. The sintered compacts had an average microhardness of 193 HV, 168 HV and 48.9 HV for sintering temperatures of 400 °C, 500 °C and 600 °C respectively. Sintering at 400 °C led to the greatest increase in hardness compared to the green compact, and

sintering at 600 °C led to a loss in hardness. The maximum experimental error was low (1.9 % to 10 %) and therefore the error bars were not plotted.

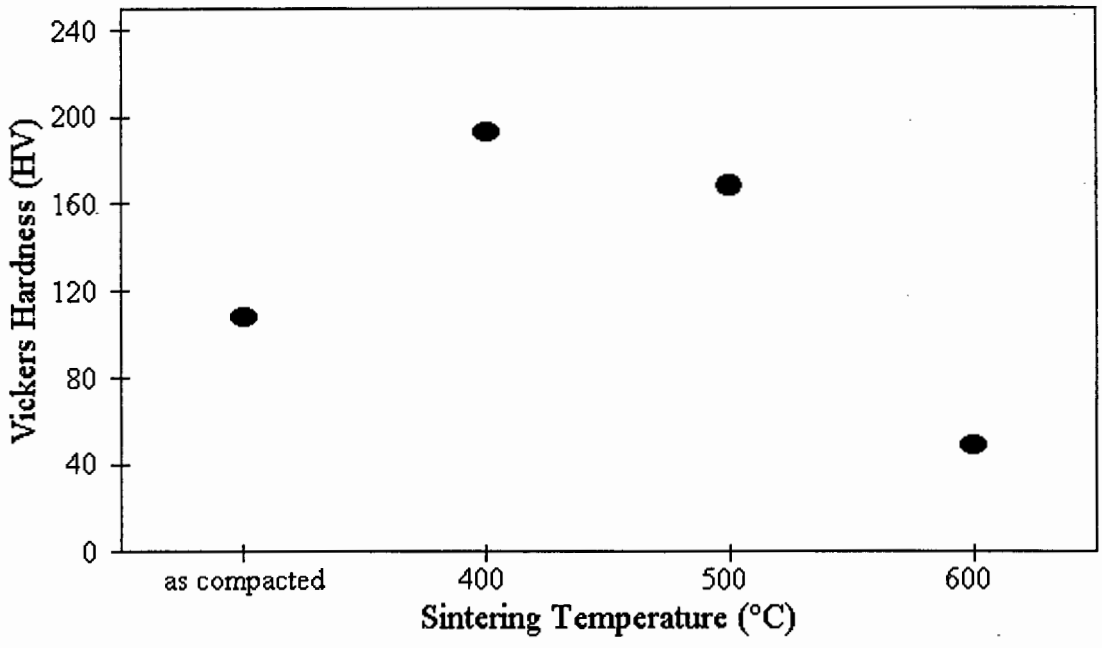

Figure 4.46: Plot of microhardness (Vickers hardness) as a function of sintering temperature of the milled cast material compared to the hardness of the green compact.

Figure 4.47 is a series of optical micrographs comparing the etched microstructures of the sintered compacts and the green compact. The sintered structures consist of a fine α phase within a δ phase matrix. The α phase is white and the δ phase grey [31]. This was verified by comparing the microstructure of the sintered compacts to that of the bulk CuSn quenched from 500 °C to produce an α phase plus δ phase microstructure. The average size of the α phase grains increases with increasing sintering temperature as shown in Table 4.8.

The structure of the compact sintered at 400 °C consists of discrete grains of α phase and δ phase. Sintering at the higher temperature of 600 °C has led to grain growth of the two phases, resulting in a microstructure consisting of interlinked α phase and δ phase.

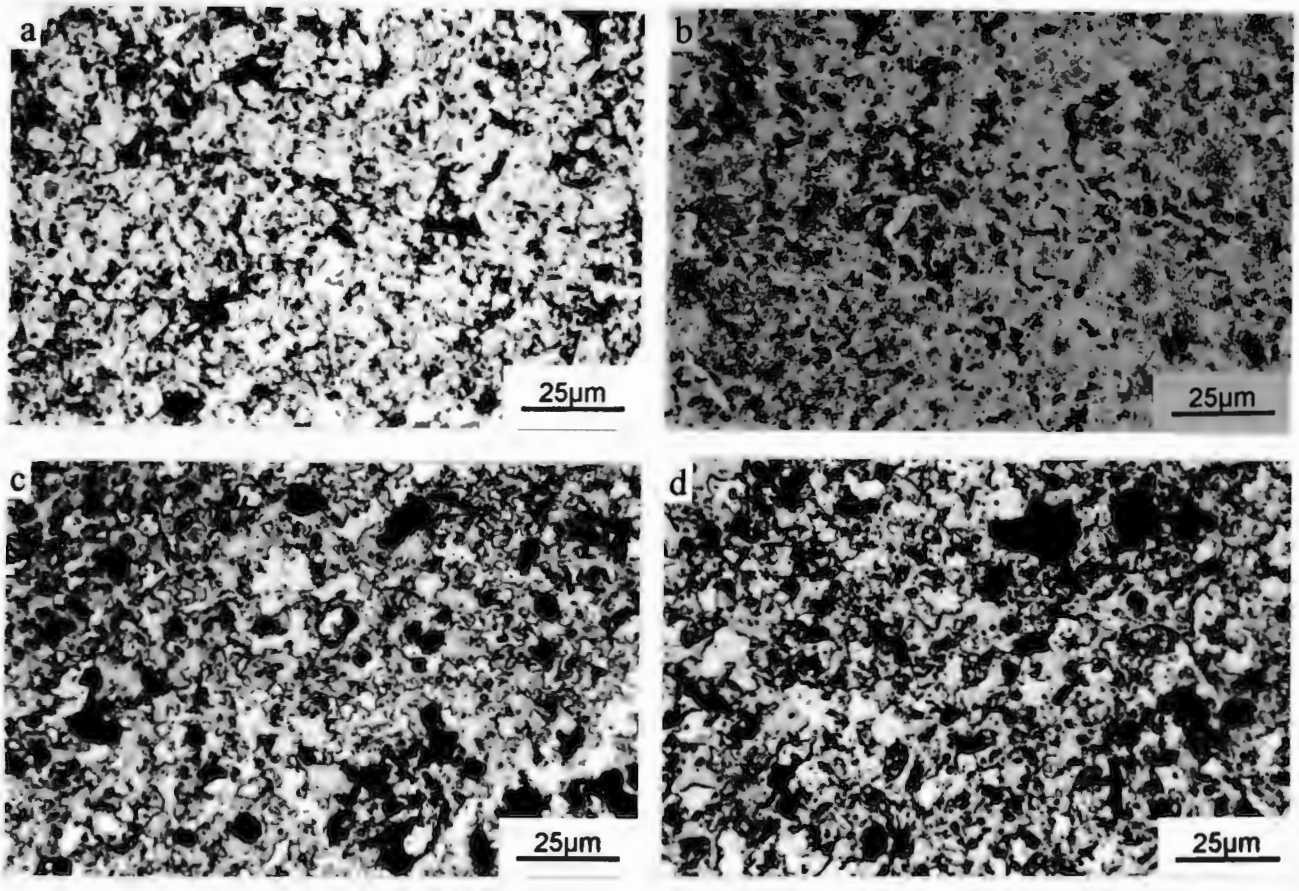

Figure 4.47: Optical micrographs showing (a) green compact, and microstructure of compacts sintered at (b) 400 °C (c) 500 °C and (d) 600 °C. (α phase - white, δ phase - grey)

Table 4.8: Table of α phase grain size, pore size and compact density as a function of condition.

Condition	α phase grain size (µm)	Pore size (µm)	Density (% of theoretical)
as compacted	-	1.7	87.7
sintered at 400 °C	2.2	2.3	87.5
sintered at 500 °C	3.9	2.4	86.8
sintered at 600 °C	4.7	2.4	86.5

The porosity of the green compact is high, and sintering has not reduced the porosity of the material, indicating that densification has not occurred (Table 4.8). The pores change from being irregular in the green compact to rounded in the sintered compacts. The average pore size remains constant at all the sintering temperatures, compared with the slightly lower pore size of the green compact, even though pore coarsening has taken place to a greater extent as the sintering temperature rises. This is due to the development of a small percentage of large pores which are far larger than the average pore size.

4.6.2 Hot Isostatic Pressing and Hot Uniaxial Pressing

Figure 4.48 (a) is an optical micrograph of the milled cast powder which was HIPed for 3 hours at 500 °C. Figure 4.48 (a) is an optical micrograph of the milled cast powder which had been HUPed using a thermo-mechanical processing pressure and temperature of 840 MPa and 400 °C.

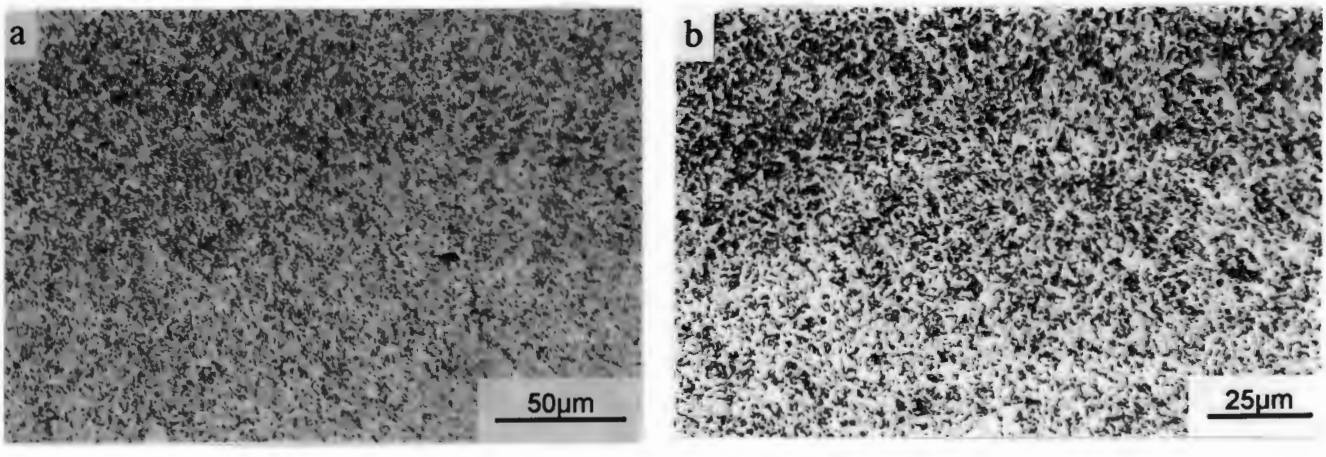

Figure 4.48: Optical micrographs showing the structure of (a) the HIPed sample and (b) the HUPed sample. (α phase - white, δ phase - grey)

Both the structures consist of a fine distribution of α phase in a δ phase matrix with a fine rounded pore structure. The porosity and the average size of the α phase grain and the pores are listed in Table 4.9.

Table 4.9: Table of compact microhardness, α phase grain size, pore size and compact density as a function of thermo-mechanical processing technique.

Condition	Microhardness (HV, 10 gf)	α phase grain size (μm)	Pore size (μm)	Density (% of theoretical)
HIPed	200	1.3	0.5	90.7
HUPed	170	1.8	0.4	87.8

- The increase in the hardness of the particles to a saturation value during milling reported in section 4.2.1 (Figure 4.11 on page 46) is an indication that the starting components have become alloyed due to cold welding, fracture and work hardening of the powder particles [38, 47]. After milling for 4 hours the experimental range is high due to the differing amounts of work hardening and differing morphologies in the milled powder. At the end of milling the experimental range has decreased, indicating that the powder is homogeneous.

5.1.2 Hardness Development

Milling of the elemental powder blend has lead to an increased hardness during milling compared with the quenched bulk material (132 HV compared with 106 HV from section 4.21 and section 4.1 respectively) as expected [38, 47], although the hardness attained during milling is lower than the hardness attained during ageing of the quenched material (195 HV from section 4.1). It was expected that the high deformation induced during milling would lead to a higher hardness development than the hardness attained using ageing, which is a conventional strengthening technique [38, 44, 47]. The lower hardness of the milled powder compared with the hardness attained by ageing may be due to the following reasons:

- The equipment used in this study may not be energetic enough to induce a highly deformed structure. The mill used was originally designed for milling of minerals to a fine powder, and not specifically for HEM of metallic samples.

- It was only possible to obtain microhardness values from large particles outside the average size range, and therefore the microhardness obtained may not reflect the average microhardness of the whole powder.

5.1.3 Formation of the η Phase

Formation of the η phase has occurred during milling (Figure 4.24 to Figure 4.26 on pages 56-57) outside the equilibrium concentration range as seen in the binary

equilibrium phase diagram shown on page 8 in Figure 2.4. The formation of the η phase can be understood if one compares the activation energy Q and diffusion coefficient D_o for the diffusion types shown in Table 5.1 [5]. Although the diffusion of copper in tin has a lower activation energy than that of tin in copper, the diffusion coefficient of tin in copper is two orders of magnitude greater than the diffusion coefficient of copper in tin. HEM has been reported to effect a high energy transfer rate between milling media and powder particles due to the repeated collisions which occur during the milling process [1, 6, 34, 38, 47]. The energy transfer during milling may be sufficient to overcome the activation energy necessary for diffusion of tin in copper, in which case a favourable condition would exist for the formation of the η phase.

Table 5.1: Table of activation energies and bulk diffusion coefficients for the diffusion types shown [5].

Diffusion type	Q (kJmol^{-1})	D_o (m^{2}s^{-1})
Cu in Cu	195.6	3.4×10^{-5}
Sn in Sn	43.9	1.2×10^{-9}
Cu in Sn	33.0	2.4×10^{-7}
Sn in Cu	117.0	2.95×10^{-5}

5.1.4 Sequence of Crystalline Phase Formation

The sequence of phase formation during milling of the elemental powder blend (shown in Table 4.3 on page 60) is discussed in this section. Diffusion of tin into copper occurs in the early stage of milling (4 hours) resulting in the formation of the tin-rich η phase in the powder as seen in Figure 4.24 on page 56. In the early to intermediate stages of milling (4 hours to 8 hours) as the powder is milled further, the δ phase forms as the η phase dissolves due to refinement of the powder via continual fracturing and cold welding and the formation of a homogeneous concentration of tin in the powder particles via the diffusion of tin (Figure 4.25 on page 57).

In the late to final stages of milling (24 hours to 48 hours) the formation of the copper-rich phases is caused by destabilisation of the tin-rich phases [60]. The η phase has dissolved completely after 24 hours as first the δ phase and then the α phase forms, and then the δ phase begins to dissolve as more α phase forms. Evidence of this is the disappearance of the η phase peaks and an increase in intensity of the δ phase peak after 24 hours of milling (Figure 4.26 on page 57), followed by a decrease in intensity of the δ phase peak, and finally an increase in intensity of the α phase peak at the end of milling (Figure 4.27 on page 58).

A similar result has been reported during MA of copper and zinc, where zinc-rich phases were first to form due to the diffusivity of zinc in copper being eight orders of magnitude higher than that of copper in zinc [50, 60]. It has been reported that the equilibrium structure of the material (the α phase and ε phase) is not formed during ageing of the bulk material due to the difficulty of formation of the ε phase [24, 26]. In contrast to this, the early formation of the tin-rich ε phase was detected during MA of Cu-20.0wt%Sn [5], a result which was not found in this work.

It is conceivable that the ε phase and also possibly the high temperature γ phase had formed during MA of CuSn, but these phases may not have formed in sufficient quantities to be detected by XRD, particularly when the phase peaks present have become broadened by the reduction of the crystalline grain size and an increase in the atomic-level strain during milling [1, 5]. The main diffraction peaks of the ε phase (43.5 ° from Table A3 on page 103) and γ phase (42.9 ° from Table 4.2 on page 55) are close to the diffraction peaks of copper (43.34 ° from Table A2 on page 103), tin (43.91 ° from Table A1 on page 102), δ phase and α phase (42.7 ° and 42.4 ° respectively from Table 4.2 on page 55) in that diffraction angle range.

5.2 Milling of Cast Powder

The sharp, angular morphology of the pulverised starting powder (Figure 4.15 (a) on page 48) indicates that the cast structure is extremely brittle due to the continuous δ phase intermetallic formed during cooling, as reported in [31]. The brittle nature of

the starting powder is the reason for the rapid decrease in particle size after 4 hours of milling (Figure 4.16 on page 49). Even though the brittle cast structure causes fracture to dominate during milling, welding of the particles has occurred to a certain extent, as can be seen in Figure 4.17 on page 50. HEM, or mechanical milling (MM) of a brittle pre-alloyed powder consisting of an intermetallic compound may be likened to MA of a brittle/brittle system. It may be expected that MA of a brittle/brittle system would not occur and that milling would only lead to a reduction of the size of the brittle components. However, it has been shown that MA of brittle/brittle systems has produced homogeneous alloys, demonstrating that MA has occurred on the atomic level for these systems [38]. It is not unreasonable to postulate that a similar process may have taken place during MM of the cast powder due to the presence of conglomerates consisting of powder fragments which have been welded together, as seen in Figure 4.17.

The change in the morphology of the particles shows that what little ductility the material has, is lost as the powder becomes more deformed during milling. After 4 hours of milling the powder consists of loosely-welded powder conglomerates (Figure 4.15 (b) on page 48 and Figure 4.17 on page 50). These conglomerates are broken up by the action of milling until the powder consists of discrete particles after 48 hours of milling (Figure 4.15 (e) on page 48).

A rise in the hardness of the cast particles during milling is expected due to work hardening, even in the brittle cast structure. This could not be confirmed as rapid particle refinement has occurred during milling to a size below which accurate microhardness determination was possible. It is possible that the hardness of the cast powder has risen during processing due to the high deformation induced during milling, as dislocations were observed during TEM examination of the milled powder (Figure 4.36 on page 65).

5.3 Milling of Melt Quenched Powder

HEM or MM of the melt quenched powder is influenced by two factors, namely the initial particle size and the microstructure of the starting material, of which the latter is presumed to be the dominant effect:

The rate of particle refinement of the melt quenched powder during milling (Figure 4.21 on page 53) is far slower than that of the cast powder (Figure 4.16 on page 49), even though the melt quenched powder is only slightly coarser (104 μm ± 28.1 μm from section 4.2.3) than the cast powder (71 μm ± 36 μm from section 4.2.2). It has been reported that the rate of particle refinement is roughly logarithmic with processing time, so the penalty (increased processing time) for starting with a coarser powder is not severe [48]. Therefore the slow rate of particle refinement during milling of the melt quenched powder compared to that of the cast powder is due to another factor.

The initial melt quenched powder is more ductile than the cast powder as it consists not only of the α phase, the brittle intermetallic δ phase and ε phase, but also of a ductile β phase matrix as shown in Figure 4.38 on page 68 [31]. The observation that fracture occurs predominantly by the less energetic intergranular fracture mode during pulverisation of the melt quenched splats (Figure 4.19 on page 51 and Figure 4.22 on page 54) and also in the early stages of milling (Figure 4.20 on page 52) indicates that the toughness of the β phase matrix of the material is the major factor in retarding particle size refinement. XRD of the material has revealed that the shape of the XRD trace has not changed substantially after 4 hours of milling, indicating that no major phase transformations have taken place (Figure 4.39 and Figure 4.40 on page 69). The only change is a decrease in the diffraction peak intensitities, which is due to strain accumulation during milling. In the late to final stages of milling (24 hours to 48 hours) the fracture mode has changed from brittle intergranular fracture to fracture of the particles due to plastic deformation, welding and work hardening of the particles (Figure 4.20). This change in fracture mode occurs when the particles have become too small to be plastically deformed.

During this stage of milling, two factors which have caused an increase in the intensity of the diffraction peak in the range 2θ = 41.5 ° to 42.5 ° relative to the intensity of the δ phase diffraction peak (Figure 4.42 and Figure 4.43 on page 71) can be identified. Firstly, the presence of the β phase would lead to the formation of the β′ phase due to deformation during milling, as it has been reported that this martensite can be formed by stressing of material containing the β phase [27, 28], and therefore cause an increase in the XRD intensity at 2θ = 42.42 °. The second factor is the destabilisation of the tin-rich δ phase during milling leading to the formation of the copper-rich α phase at 2θ = 42.4 °, a result which was similarly encountered in MA of copper and zinc [50, 60].

A rise in the particle hardness during milling of the melt quenched powder is expected due to work hardening. This could not be confirmed as particle refinement has occurred during milling to a size below which accurate microhardness determination was possible.

Milling of the melt quenched particles occurs via a two stage process, i.e. first traditional milling (particle refinement) [32], and then true MM (flattening of the particles, welding, work hardening and fracture) [1, 9] once the powder particles have reached a certain size, as seen in Figure 4.20 on page 52 and Figure 4.21 on page 53.

5.4 Extension of Solid Solution Solubility in the Milled Powder

5.4.1 Elemental Powder Blend

A shift in the diffraction peak positions during milling of the elemental powder blend as reported in section 4.3.1 indicates a change in the lattice spacing of the material due to solid solution formation, and is a common result for continuous HEM [66, 67]. The lattice parameter of the α phase at the solid solubility saturation limit is 3.7053 Å [26]. XRD has revealed that the lattice parameter of the α phase has increased from 3.62 Å for elemental copper powder (which is in close agreement with the published

value of 3.6147 Å at 20 °C [25]) to 3.72 Å after MA of the elemental powder blend (Table 4.4 on page 75).

The tin atoms have a metallic radius of 1.58 Å compared to copper atoms which have a metallic radius of 1.27 Å [68]. The increase in the lattice parameter during milling is caused by expansion of the lattice or unit cell in order to accommodate the larger tin atoms during formation of the solid solution α phase.

The result that the lattice parameter of the α phase has increased above the reported equilibrium saturation limit during milling of the elemental powder blend as reported in section 4.4 suggests that MA has caused an extension of the solid solution solubility of tin in copper. Extension of the solubility of tin in copper by MA has been reported previously [5]. The extension of the solubility limit by MA of other materials, e.g. iron in aluminium has also been reported [67].

Annealing of the milled powder causes the lattice parameter of the α phase to decrease from 3.72 Å to 3.69 Å (Table 4.4 on page 75), indicating that the solute content reverts to the equilibrium solubility limit for the composition Cu-24.6wt%Sn. The significance of this result would therefore indicate that the amount of α phase present in the milled elemental powder blend is greater than the equilibrium amount of the α phase in this material. During annealing, the following solid state reaction takes place: $\alpha_{saturated} \rightarrow \alpha_{equilibrium} + \delta$, i.e. additional δ phase and α phase with the equilibrium tin content forms due to transformation of the saturated α phase.

The results obtained compare favourably with those reported by HEM of Cu-20.0wt%Sn [5]. The formation of an extended solid solution with a lattice parameter of 3.771 Å was observed after HEM, and annealing of the milled powder led to a decrease of the lattice parameter to 3.673 Å.

Another factor which may induce a change in the lattice parameter *a* of the α phase is either interstitial carbon or hydrogen entering the copper lattice due to the

decomposition of hexane [42, 69]. Hexane was added to the powder as a surfactant to prevent excessive cold welding during milling (section 3.3).

5.4.2 Cast Powder and Melt Quenched Powder

It can be deduced that HEM of the cast powder and the melt quenched powder has also led to an extension of the solid solution solubility of the α phase. Although detailed analysis could not be performed on the lattice parameter of the α phase peaks of these powders, this deduction is supported by the observations that milling of the cast powder causes the combined α phase plus δ phase peak to shift to a lower peak position in the direction of the α phase (Figure 4.33 to Figure 4.35 on pages 63-64), and that milling of the melt quenched powder results in a powder that has a higher peak intensity in the region of the α phase than the δ phase peak (Figure 4.43 on page 71).

5.5 Nanocrystallinity during Milling

A nanocrystalline (NC) structure was produced in the milled elemental powder blend, the cast powder and the melt quenched powder. This is based on the following reasoning:

- XRD of the milled powders shows that the diffraction peaks broaden as milling progresses (sections 4.3.1 to 4.3.3). This is due to a reduction in the crystalline grain size and an increase in the atomic-level strain [2].

- TEM examination of the powders after milling has revealed the existence of contrast areas with a size ranging from approximately 5 nm to 50 nm in the powder (Figure 4.28, Figure 4.36 and Figure 4.44 on pages 59, 65 and 72 respectively). These areas have well defined boundaries and are polygonal in shape. Therefore these areas are thought to demarcate individual grains [6].

- Moiré patterns were observed during TEM examination of the milled powders (Figure 4.36 on page 65). This is an indication of crystallinity in the powders as it is a direct result of the crystallinity of a material that Moiré patterns are observed during TEM examination [25, 61, 64].

- The EDPs observed in the diffraction mode during TEM examination of the milled powders consist of concentric rings (Figure 4.28, Figure 4.36 and Figure 4.44 on pages 59, 65 and 72 respectively), indicating the presence of a large number of extremely small diffracting crystals in the area selected by the diffraction aperture [63].

The powders examined by TEM consisted of the δ phase and/or the α phase based on analysis of the EDPs obtained during TEM examination (section 4.5), a result confirmed by XRD analysis of the powders during milling (sections 4.3.1 to 4.3.3).

Due to the difficulty in preparing specimens for TEM, the most simple preparation method was employed. The powder was de-agglomerised and suspended in ethanol using an ultrasound bath, followed by transferral of droplets of the suspension onto a copper grid coated with an electron-transparent carbon support film. TEM images can be obtained from the edges of these powders or from particles which are small enough to be electron transparent. The microstructure of the edges may not be representative of the bulk particle [70], and for powders with a large size distribution, the largely electron transparent fine fraction may not be representative of the whole. Therefore it is possible that the observed nanocrystallinity may only exist in the fine electron transparent portion of the powder and not in the entire powder.

5.6 Amorphisation during Milling

An amorphous phase is formed during milling of the elemental powder blend, the cast powder and the melt quenched powder based on XRD and TEM results (section 4.3). Amorphisation of the powder has occurred at the final stage of milling due to the high energy transfer rate and deformation induced during milling of the powder [1, 34, 38].

Amorphisation has occurred presumably after the nanocrystalline grains have reached a saturation value as the stresses required for dislocation motion have become enormously high [51].

After milling for 48 hours, XRD reveals that the diffraction traces of all three of the starting powders consist of a crystalline component and an amorphous component. Confirmation of amorphisation of the powders are the presence of diffuse rings in the EDPs of the cast powder and melt quenched powder milled for 48 hrs (Figure 4.36 on page 65 and Figure 4.44 on page 72 respectively). Diffuse rings in the EDPs are an indication that a material is amorphous [25]. Amorphisation has been reported during HEM in Nb_3Sn using TEM and XRD [57].

Although diffuse rings were absent in the EDP of the milled elemental powder blend (Figure 4.28 on page 59), this does not preclude the presence of an amorphous phase. It is possible that the powder particle selected for TEM examination consisted only of nanocrystalline regions and that a large fraction of the powder consists of both amorphous and nanocrystalline components. The detection of the amorphous phase in the milled elemental powder blend using XRD confirms this, as does detection of the amorphous phase using XRD and TEM in the milled cast powder and milled melt quenched powder.

5.7 Thermo-Mechanical Processing of Milled Cast Powder

Of all the thermo-mechanical processing techniques employed, HIP produced slightly better properties in the processed sample compared with sintering and HUP (section 4.6). This is probably due to the fact that thermo-mechanical processing took place under a high positive pressure in an inert environment, compared with sintering which took place under a slightly negative pressure and hot uniaxial pressing in air. Therefore diffusional bonding was aided by a positive pressure and not hampered by oxide formation during thermo-mechanical processing.

The high porosity and microcrystalline structure observed during examination of the processed milled cast powder in section 4.6 indicates that thermo-mechanical processing of the milled powder at elevated temperatures has led to significant grain growth and a loss of nanocrystallinity of the material due to the high diffusivity of the milled powders [2, 3, 6, 7]. The observation that the porosity of the green compact does not decrease during sintering and that a high porosity is present in all of the compacted samples (section 4.6) indicates that the powder has poor compaction properties due to the highly deformed state of the milled powder. This result is not surprising as poor compaction is a common characteristic of highly deformed powders [2, 38].

5.8 Overview

In summary, it as been shown that HEM of elemental Cu-24.6wt%Sn has led to MA of the constituents, resulting in a final powder consisting of the α phase and the δ phase. Formation of the η phase (normally stable only at higher tin contents) during milling is due to the higher diffusivity of tin in copper than copper in tin. The solid solution solubility limit of the material has been extended due to the high energy imparted to the powder during milling of the elemental powder blend, indicated by an increase in the α phase lattice parameter.

HEM of the melt quenched powder proceeds via a mixed mode of firstly traditional milling (particle refinement) and then by MM (deformation, welding and fracture of the particles). This is primarily due to the limited energy transfer rate between the milling media and powder particles which the milling equipment in capable of.

Milling of the various powders has led to the development of a NC structure in the final powders due to refinement of the crystal size into the nano-range by the repeated deformation caused during milling, and the amorphous phase due to the high energy transfer rate and high deformation. The nanocrystalline plus amorphous structure of the milled cast powder has not been retained in the material during thermo-mechanical

processing at elevated temperatures due to anomalous grain growth, caused by the highly metastable state of the material after milling.

6. CONCLUSIONS

The characterisation of high energy milling on Cu-24.6wt%Sn in three initial states has been performed. The following conclusions can be drawn based on the discussion of the results obtained:

- High energy milling of an elemental powder blend, a cast powder and a melt quenched powder of the composition Cu-24.6wt%Sn has produced a structure consisting of nanocrystalline and amorphous phases in the milled powders.

- High energy milling of the elemental powder blend has caused an extension of the solid solution solubility of tin in copper.

- It has been shown for the first time that the tin-rich η phase, which is normally stable only at high tin contents, forms during high energy milling of the elemental powder blend.

7. REFERENCES

[1] C.C. Koch, *Nanostructured Mater.*, 1992, **2**, pp. 109-129.

[2] R.M. German, *"Powder Metallurgy Science"*, 2nd ed., Metal Powder Industries Federation, Princeton, New Jersey, 1994, pp. 49, 50, 73, 87, 90, 242-326.

[3] M. Gell, *Mater. Sci. Eng.*, 1995, **A204**, pp. 246-251.

[4] F.H. Froes, *Mater. Sci. Eng.*, 1994, **A184**, pp. 119-133.

[5] E. Ivanov, V. Patton, T.F. Grigorieva, *Mater. Sci. Eng.*, 1996, **A217/218**, pp. 227-280.

[6] C. Suryanarayana, F.H. Froes, *Metall. Trans. A*, 1992, **23A**, pp. 1071-1081.

[7] H. Gleiter, *Nanostructured Mater.*, 1992, **1**, pp. 1-19.

[8] R.W. Siegel, *Ann. Rev. Mater. Sci.*, 1991, **21**, pp. 559-578.

[9] H. Gleiter, *Prog. Mater. Sci.*, 1989, **33**, pp. 223-315.

[10] R. Birringer, *Mater. Sci. Eng.*, 1989, **A117**, pp. 33-43.

[11] R.E. Smallman, "*Modern Physical Metallurgy*", 4th ed., Butterworths, London, 1985, pp. 163-175.

[12] F.H. Froes, C. Suryanarayana, G. Chen, A. Frefer, G.R. Hyde, *J. Met.*, 1992, **44**, pp. 26-29.

[13] G.H. Fair, J.V. Wood, *J. Mater. Sci.*, 1994, **29**, pp. 1935-1939.

[14] D.R. Askeland, *"The Science and Engineering of Materials"*, 3rd ed., PWS Publishing Company, Boston, Massachusetts, 1994, pp. 266, 267, 305-309.

[15] R.L. Fleischer, D.M. Dimiduk, H.A. Lipsitt, *Ann. Rev. Mater. Sci.*, 1989, **19**, pp. 231-263.

[16] D.G. Morris, M.A. Morris, *Scripta Mater.*, 1996, **34**, no. 1, pp. 45-51.

[17] E.M. Schulson, D.R. Barker, *Scripta Metall.*, 1983, **17**, pp. 519-522.

[18] R. Bohn, T. Haubold, R. Birringer, H. Gleiter, *Scripta Metall. et Mater.*, 1991, **25**, pp. 811-816.

[19] D.G. Morris, S. Gunther, *Mater. Sci. Eng.*, 1996, **A208**, pp. 7-19.

[20] K. Lu, R. Lück, B. Predel, *Acta Metall. et Mater.*, 1994, **42**, no. 7, pp. 2303-2311.

[21] W. Vandermeulen, A. Deruyttere, *Metall. Trans.*, 1973, **4**, pp. 1659-1664.

[22] T.B. Massalski: in *"Physical Metallurgy"*, 3rd ed., R.W. Cahn, P. Haasen (eds.), Elsevier Science Publishers, Amsterdam, The Netherlands, 1983, pp. 188-191.

[23] T.B. Massalski, *"Binary Alloy Phase Diagrams"*, vol. 1, 2nd ed., W.W. Scott Jr. (ed.), Ohio, 1987, pp. 964-965.

[24] R. Hultgren, R.L. Orr, P.D. Anderson, K.K. Kelly, *"Selected Values of Thermodynamic Properties of Metals and Alloys"*, John Wiley & Sons, New York, New York, 1963, p. 708.

[25] J.W. Edington, *"Practical Electron Microscopy in Materials Science"*, TechBooks, Hendon, Virginia, 1976, pp. 89-91, 188-192, 291, 303-312.

[26] *"Constitution of Binary Alloys"*, 2nd ed., M. Hansen (ed.), McGraw Hill, New York, New York, 1958, pp. 633-638.

[27] M. de Bondt, A. Deruyttere, *Acta Metall.*, 1967, **15**, pp. 993-1005.

[28] G.K. Ramesh Prasad, K. Chattopadhyay, M. Mohan Rao, *J. Mater. Sci. Lett.*, 1986, **5**, pp. 991-994.

[29] K. Shimizu, H. Sakamoto, K. Otsuka, *Trans. Jpn. Inst. Met.*, 1975, **16**, pp. 581-590.

[30] I.A. Arbuzova, Y.N. Koval, V.V. Martynov, L.G. Khandros, *Phys. Met. Metallogr.*, 1973, **36**, no. 5, pp. 202-204.

[31] M.B. Cortie, C.E. Mavrocordatos, *Metall. Trans. A*, 1991, **22A**, pp. 11-18.

[32] C.C. Koch, *Ann. Rev. Mater. Sci.*, 1989, **19**, pp. 122-143.

[33] D.G. Morris, M.A. Morris, *Mater. Sci. Eng.*, 1988, **A104**, pp. 201-213.

[34] R.B. Schwarz, *Scripta Mater.*, 1996, **34**, no. 1, pp. 1-4.

[35] M. Oehring, R. Borman, *Mater. Sci. Eng.*, 1991, **A134**, pp. 1330-1333.

[36] G. Le Caer, P. Matteazzi, B. Fults, *J. Mater. Res.*, 1992, **7**, pp. 1387-1395.

[37] C.C. Koch, *Scripta Mater.*, 1996, **34**, no. 1, pp. 21-27.

[38] P.S. Gilman, J.S. Benjamin, *Ann. Rev. Mater. Sci.*, 1983, **13**, pp. 279-300.

[39] A. Corrias, G. Ennas, G. Marongiu, A. Musinu, G. Paschina, D. Zedda, *Mater. Sci. Eng.*, 1995, **A204**, pp. 211-216.

[40] "*Dry Grinding Attritors*", Union Processes, Inc. sales brochure, Akron, OH, 1993.

[41] R. Sundaresan, F.H. Froes, *J. Met.*, 1987, **39**, no. 8, pp. 22-27.

[42] R.B. Schwarz, P.B. Desch, S. Srinivasan, P. Nash, *Nanostructured Mater.*, 1992, **1**, pp. 37-42.

[43] R.Z. Valiev, R.S. Mishral, J. Grozal, A.K. Mukherjee, *Scripta Mater.*, 1996, **34**, no. 9, pp. 1443-1448.

[44] J.C. Rawers, R.C. Doan, *Metall. Mater. Trans. A*, 1994, **25A**, pp. 381-388.

[45] J.C. Rawers, G. Slavens, D. Govier, C. Dogan, R.C. Doan, *Metall. Mater. Trans. A*, 1996, **27A**, pp. 3126-3134.

[46] R.B. Schwarz, S.R. Srinivasan, J.J. Petrovic, C.J. Maggiore, *Mater. Sci. Eng.*, 1992, **A155**, pp. 75-83.

[47] T.S. Benjamin, T.E. Volin, *Metall. Trans.*, 1974, **5**, pp. 1929-1934.

[48] J.S. Benjamin, *Sci. Am.*, 1976, **234**, no. 5, pp. 40-48.

[49] J.S. Benjamin, *Metall. Trans.*, 1970, **1**, pp. 2943-2951.

[50] S.K. Pabi, B.S. Murty, *Mater. Sci. Eng.*, 1996, **A214**, pp. 146-152.

[51] H.J. Fecht, E. Hellstern, Z. Fu, W.L. Johnson, *Metall. Trans. A*, 1990, **21A**, pp. 2333-2337.

[52] J.S. Forrester, G.B. Schaffer, *Metall. Mater. Trans. A*, 1995, **26A**, pp. 725-730.

[53] D.L. Zhang, *J. Mater. Sci. Lett.*, 1995, **14**, pp. 1508-1511.

[54] P. Lee, J. Yang, *Mater. Sci. Eng.*, 1996, **A208**, pp. 76-79.

[55] W. Guo, A. Iasonna, M. Magini, S. Martelli, F. Padella, *J. Mater. Sci.*, 1994, **29**, pp. 2436-2444.

[56] R.B. Schwarz, C.C. Koch, *Appl. Phys. Lett.*, 1986, **49**, no. 3, pp. 146-148.

[57] Y.S. Cho, C.C. Koch, *Mater. Sci. Eng.*, 1991, **A141**, pp. 139-148.

[58] H. Hahn, J. Logas, R.S. Averback, *J. Mater. Res.*, 1990, **5**, pp. 609-614.

[59] G.F. van der Voort, *"Metallographic Principles and Practices"*, McGraw Hill, New York, New York, 1984, p. 571.

[60] S.K. Pabi, J. Joardar, B.S. Murty, *J. Mater. Sci.*, 1996, **31**, pp. 3207-3211.

[61] P. Hirsch, A. Howie, R.B. Nicholson, D.W. Pashley, M.J. Whelan, *"Electron Microscopy of Thin Crystals"*, 2nd ed., Robert E. Krieger Publishing Co. Huntington, New York, 1977, pp. 169, 170.

[62] D.W. Smith, *Trans. AIMM*, 1933, **104**, pp. 48-63.

[63] P.J. Goodhew, F.J. Humphreys, *"Electron Microscopy and Analysis"*, 2nd ed., Taylor & Francis, London, 1988, pp. 23, 44, 45.

[64] M. von Heimendahl, *"Electron Microscopy of Materials"*, A.S. Nowick (ed.), Academic Press, London, 1980, pp. 205-209.

[65] C. Hammond, *"Introduction to Crystallography"*, Oxford University Press, New York, New York, 1990, p. 62.

[66] T.D. Shen, C.C. Koch, *Acta Metall.*, 1996, **44**, no. 2, pp. 753-761.

[67] V.I. Fadeeva, A.V. Leonov, *Mater. Sci. Eng.*, 1996, **A206**, pp. 90-94.

[68] A.H. Cottrell, *"An Introduction to Metallurgy"*, Edward Arnold Publishers Ltd., London, 1967, pp. 35, 36.

[69] P.B. Desch, R.B. Schwarz, P. Nash, *Scripta Mater.*, 1996, **34**, no. 1, pp. 37-43.

[70] J.Y. Huang, Y.K. Wu, H.Q. Ye, *Mater. Sci. Eng.*, 1995, **A199**, pp. 165-172.

8. APPENDICES

Appendix A: Tables of Interplanar Spacing, Intensity and Diffraction Angle of Relevant Phases

Table A1: Table of *d*-spacing, intensity and diffraction angle for tin.
Source: *JCPDS* diffraction file 4-673. (* denotes strong lines)

d (Å)	*I* (%)	2*θ* (deg.)
2.915 *	100	30.67
2.793 *	90	32.05
2.062 *	34	43.91
2.017 *	74	44.95
1.659 *	17	55.39
1.484 *	23	62.60
1.458	13	63.85
1.442 *	20	64.64
1.304	15	72.49
1.292	15	73.27
1.205 *	20	79.56
1.095	13	89.52
1.0434	3	95.28
1.0401	5	95.68
1.0309	2	96.82
1.0252	5	97.54
0.9824	5	103.4
0.9718	2	105.0
0.9310	3	111.8
0.9286	13	112.3
0.9219	5	113.5
0.9178	5	114.3
0.8868	4	120.8
0.8755	2	123.4
0.8485	4	130.6
0.8466	10	131.2
0.8386	4	133.7
0.8086	6	144.9
0.8058	3	146.2

Table A2: Table of *d*-spacing, intensity, diffraction angle and plane indices for copper. Source: *JCPDS* powder diffraction file 4-836. (* denotes strong lines)

d (Å)	*I* (%)	2*θ* (deg.)	*h k l*
2.088 *	100	43.34	1 1 1
1.808 *	46	50.48	2 0 0
1.278 *	20	74.21	2 2 0
1.090 *	17	90.04	3 1 1
1.0436 *	5	95.26	2 2 2
0.9038 *	3	117.1	4 0 0
0.8293 *	9	136.8	3 3 1
0.8083 *	8	145.1	4 2 0

Table A3: Table of *d*-spacing, intensity and diffraction angle for ε phase (Cu_3Sn). Source: *JCPDS* powder diffraction file 1-1240. (* denotes strong lines)

d (Å)		*I* (%)	2*θ* (deg.)
2.38	*	20	37.8
2.16	*	40	41.8
2.08	*	100	43.5
1.60	*	27	57.6
1.38	*	30	67.9
1.24	*	40	76.9
1.19		5	80.8
1.16	*	30	83.3
1.15		17	84.2
1.08		7	91.1
1.04		7	95.7
0.98		8	104
0.92	*	20	114
0.90		7	118
0.88	*	20	122
0.85	*	24	130
0.83		12	137

Table A4: Table of *d*-spacing, intensity and diffraction angle for η phase (Cu_6Sn_5). Source: *JCPDS* powder diffraction file 2-713. (* denotes strong lines)

d (Å)		*I* (%)	*2θ* (deg.)
2.96	*	100	30.2
2.55		50	35.2
2.09	*	100	43.3
2.08	*	100	43.5
1.71		70	53.6
1.62		50	56.8
1.54	*	100	60.1
1.48	*	100	62.8
1.32	*	100	71.5
1.27		50	74.8
1.24		50	76.9
1.21	*	100	79.2
1.20		20	80.0
1.091		20	89.93
1.090	*	100	90.04
1.070		70	92.20
1.050		70	94.49
0.990		70	102
0.980		70	104

Table A5: Table of *d*-spacing, intensity and diffraction angle for β' phase ($Cu_{5.6}Sn$). Source: *JCPDS* powder diffraction file 31-487. (* denotes strong lines)

d (Å)		*I* (%)	*2θ* (deg.)
2.629	*	10	34.11
2.131	*	100	42.42
1.859	*	20	49.01
1.496	*	10	62.04
1.301	*	10	72.69
1.218	*	20	78.54
1.106	*	20	88.39
1.067	*	10	92.54
0.877		5	123
0.847		5	131

Table A6: Table of d-spacing, intensity and diffraction angle for β" phase. Source: JCPDS diffraction file 6-621. (* denotes strong lines)

d (Å)		Int. (%)	2θ (deg.)
2.3	*	70	39
2.16	*	100	41.8
2.03	*	100	44.6
2.02	*	70	44.9
1.57	*	70	58.8
1.34	*	70	70.3
1.32	*	100	71.5
1.22	*	70	78.4
1.14		40	85.1
1.13	*	100	86.0
1.12	*	70	87.0
1.10	*	70	89.0
1.08	*	70	91.1

Table A7: Table of *d*-spacing, intensity and diffraction angle for δ phase ($Cu_{41}Sn_{11}$). Source: *JCPDS* powder diffraction file 30-510. (* denotes strong lines)

d (Å)		*I* (%)	*2θ* (deg.)
3.67		3	24.3
3.46	*	9	25.8
2.997	*	5	29.81
2.595	*	5	34.57
2.518		2	35.66
2.403	*	4	37.43
2.119	*	100	42.67
2.076		2	43.60
1.9167	*	4	47.44
1.8351		3	49.69
1.7631		2	51.86
1.4983	*	6	61.94
1.3255		2	71.14
1.2976		3	72.91
1.2714		2	74.66
1.2234	*	10	78.13
1.1066		3	88.33
0.8009		2	148.59

Table A8: Table of *d*-spacing, intensity and diffraction angle for δ phase ($Cu_{327.9}Sn_{88.08}$). Source: *JCPDS* powder diffraction file 30-511. (* denotes strong lines)

d (Å)	*I* (%)	2θ (deg.)
3.666	3	24.28
3.456 *	8	25.78
3.036	1	29.42
2.9938 *	5	29.85
2.5932 *	5	34.59
2.5157	2	35.69
2.4001 *	4	37.48
2.1782	1	41.46
2.1168 *	100	42.72
2.0742	2	43.64
2.0087	1	45.14
1.9149 *	5	47.49
1.8337	3	49.73
1.8051	2	50.57
1.7616	2	51.91
1.7288	1	52.97
1.4969 *	6	62.00
1.4819	1	62.70
1.4573	1	63.88
1.3736	1	68.29
1.3390	1	70.31
1.3242	2	71.22
1.2965	3	72.98
1.2703	2	74.74
1.2224 *	10	78.21
1.1408	1	85.04
1.1057 *	4	88.42
1.0892	1	90.12
1.0586	2	93.49
0.9468	1	109.0
0.9073	2	116.4
0.8893	1	120.2
0.8412	2	132.9
0.8199	1	140.2
0.8002	2	148.9

Table A9: Table of *d*-spacing, intensity and diffraction angle for δ phase ($Cu_{40.5}Sn_{11}$). Source: *JCPDS* powder diffraction file 31-485. (* denotes strong lines)

d (Å)	*I* (%)	*2θ* (deg.)
9.0	1	9.8
3.675	3	24.22
3.466 *	10	25.71
2.9986 *	7	29.80
2.5976 *	4	34.53
2.5212	2	35.61
2.4063 *	4	37.38
2.1843	1	41.34
2.1225 *	100	42.60
2.0797	1	43.52
2.0137	1	45.02
1.9202	3	47.35
1.8378	2	49.61
1.8098	2	50.43
1.7660	1	51.77
1.7330	1	52.83
1.5672	1	58.94
1.5009 *	8	61.82
1.4857	1	62.52
1.4610	1	63.70
1.3772	1	68.09
1.3423	1	70.11
1.3278	1	70.99
1.2999	3	72.76
1.2735	1	74.52
1.2256 *	12	77.96
1.1085 *	5	88.14
1.0612	2	93.19
0.9493	2	108.6
0.9097	2	115.9
0.8916	1	119.7
0.8665	1	125.7
0.8434	2	132.2
0.8221	1	139.4
0.8022	3	147.9
0.7838	1	159.3

Table A10: Table of *d*-spacing, intensity and diffraction angle for δ phase ($Cu_{81}Sn_{22}$). Source: *JCPDS* powder diffraction file 31-486. (* denotes strong lines)

d (Å)	*I* (%)	2*θ* (deg.)
3.669	3	24.26
3.458 *	9	25.77
3.038	1	29.40
2.9957 *	5	29.83
2.5947 *	5	34.57
2.5171	2	35.67
2.4026 *	4	37.44
2.1802	1	41.42
2.1187 *	100	42.68
2.0760	2	43.60
2.0103	1	45.10
1.9164 *	4	47.45
1.8351	3	49.69
1.8071	2	50.51
1.7629	2	51.87
1.7379	1	52.67
1.7300	1	52.93
1.4982 *	7	61.94
1.4831	1	62.65
1.4585	1	63.83
1.3750	1	68.21
1.3403	2	70.23
1.3255	2	71.14
1.2975	3	72.91
1.2714	2	74.66
1.2235 *	12	78.12
1.1934	1	80.49
1.1417	1	84.96
1.1065 *	5	88.34
1.0901	1	90.03
1.0595	2	93.39
0.9987	1	101.1
0.9476	2	108.9
0.9081	2	116.2
0.8901	1	120.0
0.8651	1	126.1
0.8419	3	132.6
0.8207	1	139.9
0.8009 *	4	148.6
0.7946	1	152.0
0.7825	1	160.3

Table A11: Table of *d*-spacing, intensity and diffraction angle for copper oxide (Cu_4O_3). Source: *JCPDS* powder diffraction file 33-480. (* denotes strong lines)

d (Å)	*I* (%)	2*θ* (deg.)
5.032	2	17.63
3.174 *	100	28.12
2.918 *	38	30.64
2.483 *	7	36.18
2.064 *	7	43.87
2.050	5	44.18
1.8912 *	16	48.12
1.8805 *	10	48.41
1.7302 *	21	52.93
1.5871 *	10	58.13
1.5364 *	7	60.24
1.4592	3	63.79
1.3258	3	71.12
1.3052	3	72.42
1.2581	2	75.59
1.2324	5	77.45
1.1553	3	83.73
1.1424	2	84.89
1.1155	2	87.45

Table A12: Table of *d*-spacing, intensity and diffraction angle for copper oxide (Cu_2O). Source: *JCPDS* powder diffraction file 5-667. (* denotes strong lines)

d (Å)	*I* (%)	2*θ* (deg.)
3.02 *	9	29.6
2.465 *	100	36.45
2.135 *	37	42.34
1.743	1	52.51
1.510 *	27	61.41
1.287 *	17	73.61
1.233 *	4	77.41
1.0674	2	92.49
0.9795 *	4	103.8
0.9548 *	3	107.7
0.8715	3	124.4
0.8216	3	139.6

Table A13: Table of *d*-spacing, intensity and diffraction angle for copper oxide (Cu_4O_3). Source: *JCPDS* powder diffraction file 3-879. (* denotes strong lines)

d (Å)		*I* (%)	2*θ* (deg.)
3.13		20	28.5
2.90	*	40	30.8
2.50	*	100	35.9
2.47	*	40	36.4
2.05	*	60	44.2
1.88		20	48.4
1.58	*	80	58.4
1.45	*	60	64.2
1.43	*	60	65.3
1.25	*	80	76.2
1.24	*	40	76.9
1.06	*	40	93.3
1.03		20	96.9
1.02	*	40	98.2
0.951	*	40	108
0.941	*	40	110
0.937	*	40	111
0.918		20	114
0.861	*	40	127
0.834	*	40	135
0.823		20	139

Table A14: Table of *d*-spacing, intensity and diffraction angle for copper oxide (CuO). Source: *JCPDS* powder diffraction file 5-661. (* denotes strong lines)

d (Å)	*I* (%)	2*θ* (deg.)
2.751 *	12	32.55
2.530 *	49	35.49
2.523 *	100	35.59
2.323 *	96	38.77
2.312 *	30	38.96
1.959	3	46.35
1.866 *	25	48.81
1.778	2	51.40
1.714	8	53.46
1.581 *	14	58.37
1.505 *	20	61.63
1.418 *	12	65.87
1.410 *	15	66.30
1.375 *	19	68.21
1.304	7	72.49
1.265	6	75.10
1.262	7	75.31
1.1961	2	80.27
1.1697	5	82.47
1.1620	3	83.14
1.1585	2	83.44
1.1556	4	83.70
1.1233	2	86.69
1.0916	6	89.87
1.0737	2	91.79
1.0394	<1	95.77
1.0178	3	98.49
1.0074	4	99.87
0.9921	<1	102.0
0.9808	4	103.6
0.9576	3	107.2
0.9435	<1	109.6
0.9390	4	110.4
0.9332	2	111.4
0.9209	2	113.7
0.9100	2	115.8
0.9039	1	117.1

Table A15: Table of *d*-spacing, intensity and diffraction angle for tin oxide (SnO). Source: *JCPDS* powder diffraction file 6-395. (* denotes strong lines)

d (Å)	*I* (%)	2*θ* (deg.)
4.85	10	18.3
2.989 *	100	29.90
2.688 *	35	33.34
2.418 *	14	37.19
2.039	<1	44.44
1.901 *	14	47.85
1.797 *	25	50.81
1.604 *	25	57.46
1.494 *	12	62.14
1.484 *	12	62.60
1.382	4	67.82
1.344	6	70.01
1.225	4	78.01
1.209	4	79.24
1.202	4	79.80
1.1747	6	82.04
1.1697	8	82.47
1.1520	2	84.02
1.1026	4	88.73
1.0766	6	91.47
1.0303	4	96.89
1.0201	4	98.19
0.9965	2	101.4
0.9852	2	103.0
0.9674	<1	105.7
0.9507	4	108.4
0.9371	4	110.7
0.9056	4	116.7
0.8988	4	118.1
0.8824	6	121.8
0.8524	4	129.5
0.8503	4	130.1
0.8405	6	133.1
0.8062	2	146.0
0.8020	<1	148.0
0.8002	2	148.9

Table A16: Table of *d*-spacing, intensity and diffraction angle for tin oxide (SnO_2). Source: *JCPDS* powder diffraction file 21-1250. (* denotes strong lines)

d (Å)	*I* (%)	2*θ* (deg.)
3.351 *	100	26.60
2.644 *	81	33.91
2.369 *	24	37.99
2.309	5	39.01
2.120	2	42.65
1.765 *	63	51.80
1.675 *	17	54.81
1.593	8	57.89
1.498 *	13	61.95
1.439 *	17	64.79
1.415 *	15	66.03
1.322	7	71.35
1.215	11	78.78
1.184	3	81.26
1.155	8	83.75
1.117	3	87.30
1.092	8	89.83
1.081	8	91.00
1.059	3	93.45
1.036	4	96.18
0.9505	8	108.4
0.9291	3	112.2
0.9143	3	115.0
0.9081	8	116.2
0.8819	7	121.9
0.8814	6	122.0
0.8480	6	130.8
0.8375	1	134.0
0.8261	4	137.9
0.8125	2	143.2
0.8026	6	147.7

Appendix B: XRD of α phase, β phase and γ phase

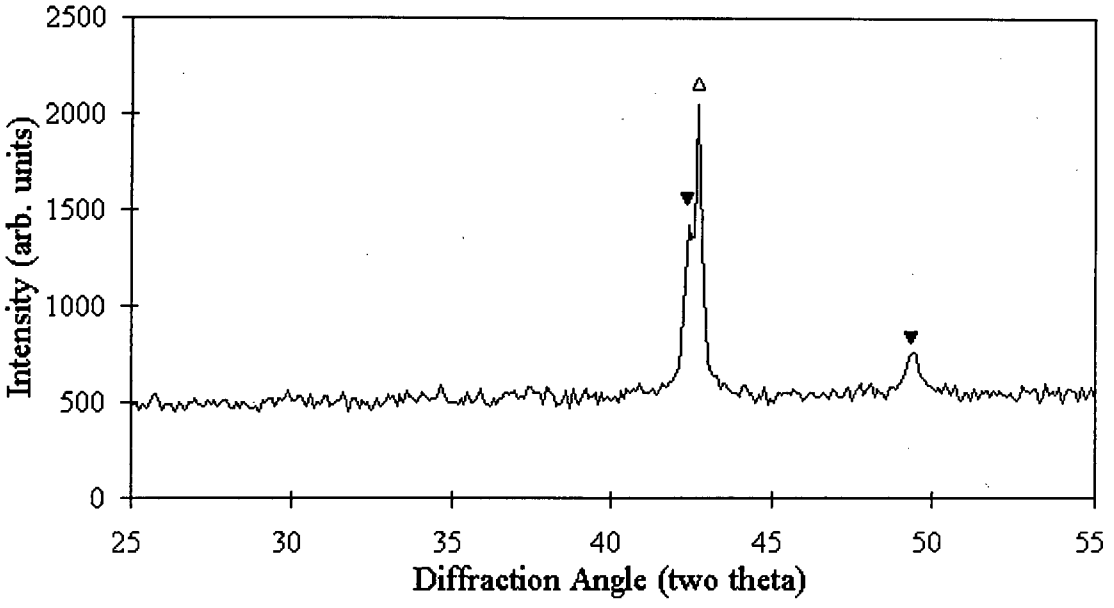

Figure B1: XRD trace of ▼ α phase and △ δ phase.

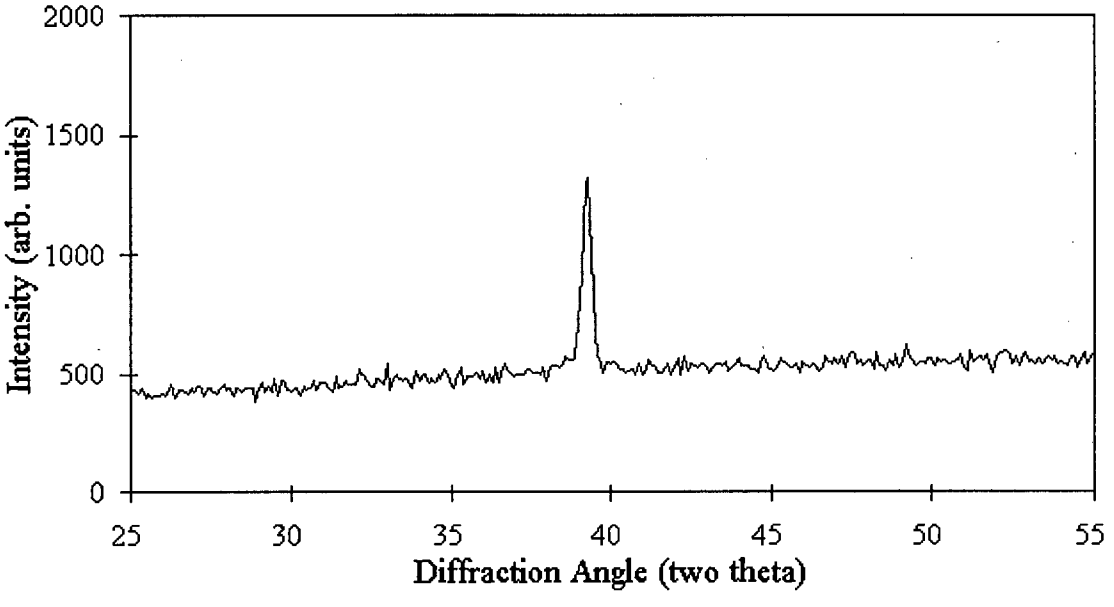

Figure B2: XRD trace of β phase.

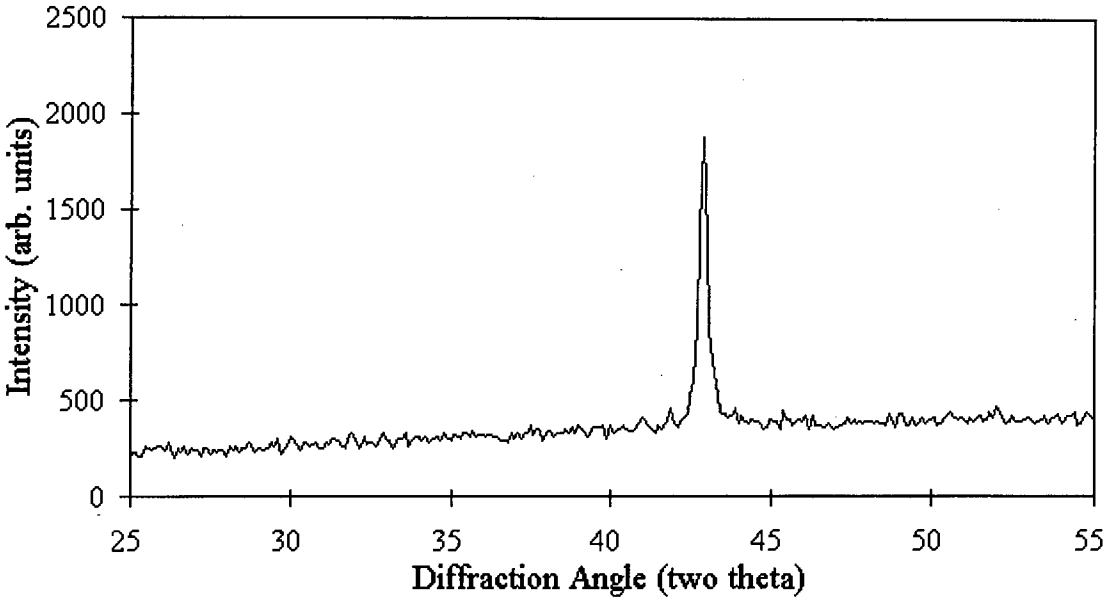

Figure B3: XRD trace of γ phase.

Appendix C: XRD of Milled and Annealed Cast Powder and Melt Quenched Powder

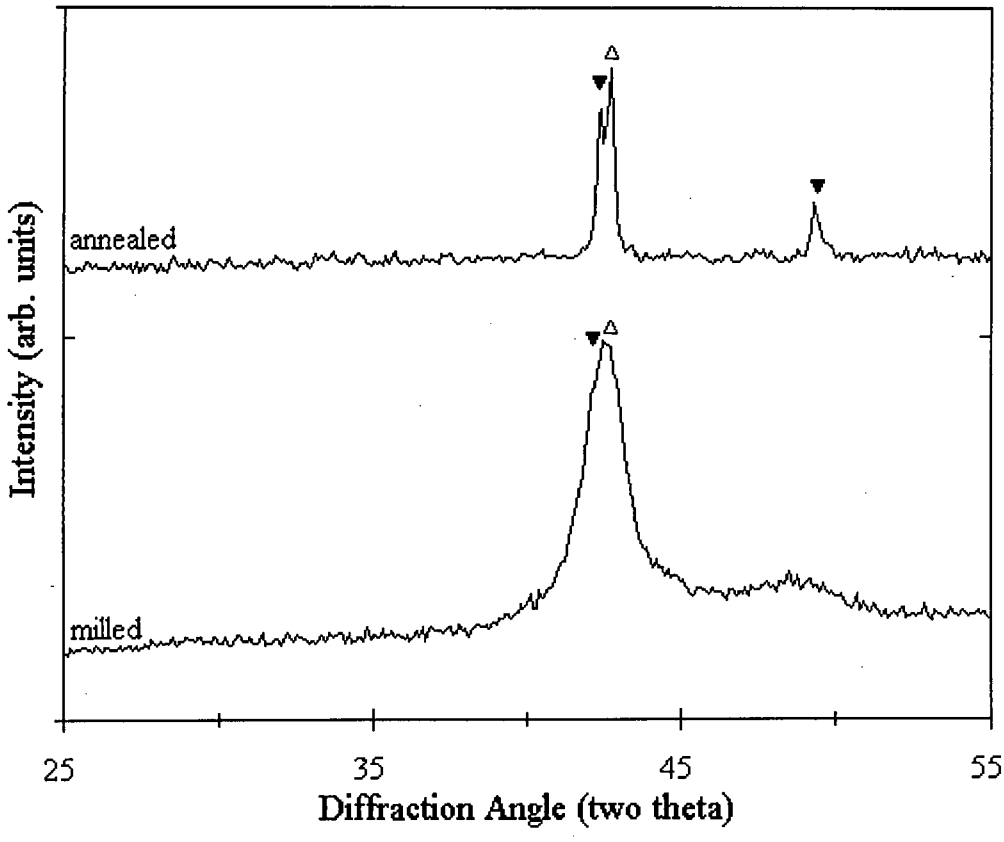

Figure C1: Plot showing XRD traces of the cast powder after milling for 48 hours and after the milled powder had been annealed at 450 °C for 1 hour.

Labels: ▵ δ phase, ▼ α phase.

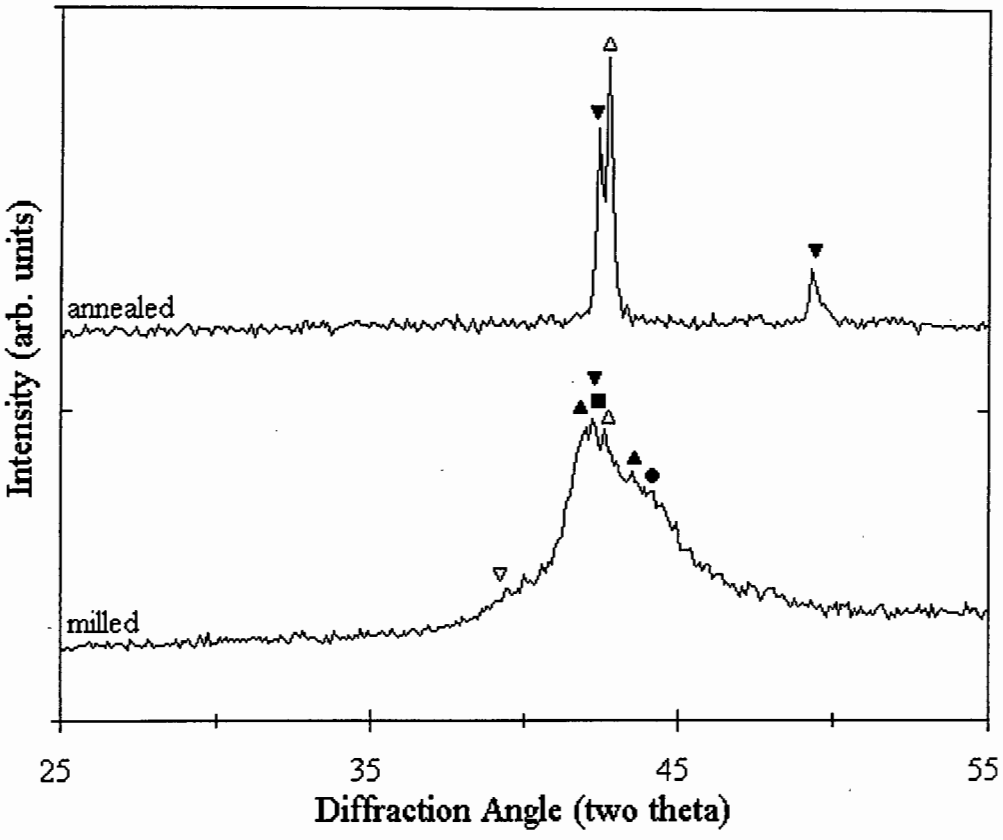

Figure C2: Plot showing XRD traces of the melt quenched powder after milling for 48 hours and after the milled powder had been annealed at 450 °C for 1 hour.

Labels: △ δ phase, ▼ α phase, ▽ β phase, ■ β′ phase, ▲ ε phase, ● Cu_4O_3.

Erosion of Glass Impacted With Spherical Particles

Z. Feng and A. Ball
Department of Materials Engineering .
University of Cape Town
R. South Africa

The erosion of soda-lime-glass by glass beads has been investigated over a range of particle diameters D(63-1000μm), velocities V(33 ms^{-1} to 113ms^{-1}) and impact angle α(30^0 to 90^0). Erosion test also was carried on steel ball for comparative purpose. Detailed studies of the influence of the impact variables on the erosion rate as well as scanning microscopy studies of the eroded surface and erodents before and after impact have been performed. The modes and mechanisms of erosion of glass impacted by spherical erodents are discussed.

With glass bead below or in the size range 180-250μm and at low velocity impact, the material removal is associated with the fatigue controlled processes. With increasing velocity, no Hertzian cracks occur in terms of the scarcity of nucleating crack and insufficient strain energy in the system due to small contact radius and less contact time even when the applied force is great enough to produce the critical tension at the rim of the area of contact. With further increasing velocity, the material removal is associated with the combination of mechanism of lateral crack and fatigue processes. With glass beads above or in the size range 400-500μm, material removal is associated with the interaction of Hertzian cone cracks and lateral cracks over velocities ranging from 33ms^{-1} to 57ms^{-1}.

There is a sharp increase in erosion rate above a certain threshold velocity and angle. The threshold velocity transition shifts from the low velocity regime to the high veloctiy regime with decreasing impingement angle. The threshold angle transition shifts from the low angle regime to the high regime with increasing velocity or decreasing particle size.

The erosion rate increases with increasing particle size. Particularly, there is a sharp increase in erosion rate at a certain particle size which is dependent upon impact angle and velocity. The slope of erosion rate decreased with further increasing particle size

ranges above 400-500μm. It can be rationalised in terms of the increased crushing particle size and fragmentation of the particles during impact.

There is slightly higher in erosion rate of glass caused by steel ball compared to glass beads. It may be ascribed to less kinetic energy dissipated by glass beads into the target due to its fragmentation, which offsets the benefit of higher hardness.